Western Graduate&PostdoctoralStudies

Western University
Scholarship@Western

Electronic Thesis and Dissertation Repository

12-17-2021 2:00 PM

The Effects of Solution pH, Temperature and Redox Environment on Corrosion and Oxide Formation on Inconel X-750

Mohsen Bahrami, *The University of Western Ontario*

Supervisor: Wren, Jungsook C., *The University of Western Ontario*

A thesis submitted in partial fulfillment of the requirements for the Doctor of Philosophy degree in Chemistry

© Mohsen Bahrami 2021

Follow this and additional works at: https://ir.lib.uwo.ca/etd

 Part of the Inorganic Chemistry Commons, and the Physical Chemistry Commons

Recommended Citation

Bahrami, Mohsen, "The Effects of Solution pH, Temperature and Redox Environment on Corrosion and Oxide Formation on Inconel X-750" (2021). *Electronic Thesis and Dissertation Repository*. 8349.
https://ir.lib.uwo.ca/etd/8349

This Dissertation/Thesis is brought to you for free and open access by Scholarship@Western. It has been accepted for inclusion in Electronic Thesis and Dissertation Repository by an authorized administrator of Scholarship@Western. For more information, please contact wlswadmin@uwo.ca.

ABSTRACT

Nickel-based superalloys have a wide range of applications in different industries due to their exceptional mechanical and corrosion-resistance properties. These alloys are widely employed in the nuclear industry. Inside a nuclear reactor, these alloys are exposed to a continuous flux of gamma-radiation. When exposed to gamma-radiation, water decomposes, resulting in the production of oxidizing and reducing species. These species have a considerable effect on the redox chemistry of the solution, which controls the overall corrosion behaviour of nickel-based superalloys.

Corrosion of metals and alloys involves several elementary steps. A comprehensive understanding of these steps and how they influence each other is key to predicting the overall corrosion behaviour of an alloy. This thesis investigates the effect of solution conditions on the corrosion of Inconel X-750, which is a nickel-based superalloy and consists of three main elements (i.e., Cr, Fe and Ni). The parameters studied in this thesis are solution pH, temperature, dissolved oxygen concentration and the presence and absence of gamma-radiation. Electrochemistry experiments were coupled with coupon-exposure tests in order to better understand the effects of these parameters on the corrosion kinetics of Inconel X-750. Solution analysis was carried out to measure the amounts of dissolved ions, while the surfaces of corroded coupons were analyzed to evaluate the morphology of the oxide films formed.

The results showed that the corrosion evolution of Inconel X-750 starts with a 1st (pseudo-) steady-state but does not remain in this steady-state. Rather, the corroding system evolves toward a 2nd (pseudo-) steady-state, which is close to the redox potential of a metal oxide/hydroxide solid species or between the redox potentials of two sets of metal oxide/hydroxide solid species. The evolution of the corroding system from the 1st to 2nd (pseudo-) steady-state was attributed to the precipitation and formation of corrosion products in the form of a hydrogel network which facilitated the formation of metal cations of higher oxidation states. Once a hydrogel network had developed, the metal

cations of higher oxidation states acted as the main oxidant and controlled the interfacial reactions. In later stages, the hydrogel network could dehydrate and convert into solid crystal oxides which could further inhibit metal oxidation.

KEYWORDS

Inconel X-750, Nickel-based Superalloy, Corrosion, Oxide Film, Gamma-radiation, Redox Conditions

SUMMARY FOR LAY AUDIENCE

Nickel-based superalloys are extensively used in the nuclear industry due to their exceptional mechanical and corrosion-resistance properties. Inside a nuclear reactor, these alloys are exposed to gamma-radiation. Gamma-radiation decomposes water, resulting in the generation of oxidizing and reducing species which can significantly affect the solution properties. Therefore, understanding the effect of solution properties on the corrosion behaviour of nickel-based superalloys is necessary to predict their long-term behaviours.

This thesis investigates the effect of solution properties on the corrosion of Inconel X-750, which is a nickel-based superalloy. The parameters studied in this thesis are solution pH, temperature, dissolved oxygen concentration, and gamma-radiation. Electrochemistry and corrosion experiments were carried out in order to understand the effects of these parameters on the corrosion behaviour of Inconel X-750. The oxide films and the solutions obtained from the corrosion experiments were analyzed by scanning electron microscopy and an advanced solution analysis technique, respectively.

The results showed that the corrosion evolution of Inconel X-750 started with an initial steady-state but did not remain in this steady-state. Rather, the corroding system evolved toward a final steady-state. The evolution of the corroding system from the initial to the final steady-state was attributed to the precipitation of corrosion products, which facilitated the formation of metal cations of higher oxidation states. This resulted in the development of the precipitated corrosion products. The metal cations of higher oxidation states controlled the overall corrosion process at longer times. In addition, the precipitated corrosion products could convert into solid crystal oxides and decrease the rate of metal oxidation.

DEDICATION

To my father, who sacrificed his dreams so that I could fulfil mine.

CO-AUTHOURSHIP STATEMENT

For this thesis, I am the author of all Chapters and Appendices.

Dr. J. Clara Wren provided invaluable scientific comments on this thesis.

Dr. Jiju Joseph helped with the post-test solution analysis.

ACKNOWLEDGEMENTS

There are many individuals who travelled this journey with me and to whom I am eternally grateful.

Dr. J. Clara Wren gave me the opportunity to study corrosion behaviour of my alloy of interest and invested tremendous effort and time to train me as a corrosion scientist.

Dr. Jiju Joseph helped with reviewing and editing of all Chapters and with coupon exposure tests.

G. Whitaker helped with the refinement and editing of all Chapters and Appendices.

I would like to sincerely thank Dr. James Noël who spent a lot of time helping me refine my understanding of corrosion fundamentals.

A special thanks must go to Dr. Guo for his unconditional help and support in the lab, help with SEM imaging, and scientific input.

I would like to thank Dr. Karimihaghighi for her help with coupon exposure tests, SEM imaging, formatting and scientific comments.

Thanks to Dr. Lindsay Grandy, Masoud Zakeri, and Dr. Momeni for holding many scientific discussions and help in the lab.

Thank you to the Western Nanofabrication Facility where I was able to complete the SEM imaging included in Chapter 6, especially Mr. Tim Goldhawk and Dr. Todd Simpson for their time training and assisting me with SEM imaging.

I would like to thank NSERC for financial support of this project, which was fully funded by Dr. Clara Wren's NSERC discovery grant.

Finally, thanks to all previous and current Wren and Shoesmith/Noël group members who helped me in the lab and enhanced my understanding of corrosion.

TABLE OF CONTENTS

LIST OF TABLES

LIST OF FIGURES

LIST OF ABBREVIATIONS, SYMBOLS, AND NOMENCLATURE

Symbol	Name	Unit & Value
$a_{M^{n+}_{(aq)\|int}}$	Chemical activity of dissolved metal cation in interfacial region	–
$a_{M^{0}_{(m)\|int}}$	Chemical activity of metal	–
α	Transfer or symmetry coefficient	–
$CV_{t=0}$	Cyclic voltammetry without a prior E_{corr} measurement	–
ΔE_{therm}	Thermodynamic driving force for corrosion	V
e^-	Electron	–
η (or η_{rxn})	Overpotential (for a redox half-reaction)	V
η_{ox}	Overpotential for a metal oxidation half-reaction	V
η_{red}	Overpotential for an oxidant (or solution) reduction half-reaction	V
$E^{i=0,f}_{CV_{t=0}}$	$E^{i=0}$ on the positive potential scan of $CV_{t=0}$	V
$E^{i=0,u}_{CV_{t=0}}$	The most positive (most noble) $E^{i=0}$ on the positive	

	potential scan of $CV_{t=0}$	V
$E_{CV_{t=0}}^{i=0,m}$	The middle $E^{i=0}$ on the positive potential scan of $CV_{t=0}$	V
$E_{PD_{t=24}}^{i=0,f}$	$E^{i=0}$ on the $PD_{t=24}$	V
$E_{M/M^{n+}}^{e}$	Equilibrium potential of the material in the environment of interest	V
$E_{Ox/Red}^{e}$	Redox potential of the environment	V
E_{corr} (or E_{CORR})	Corrosion potential	V
E_{elec}	Electrode potential	V
$E^{i=0}$	Applied potential at which measured current density is zero	V
E_{ox}^{eq}	Equilibrium potential of an oxidation half-reaction	V
E_{red}^{eq}	Equilibrium potential of an oxidant (or solution) reduction half- reaction	V
E_{rxn}^{eq}	Equilibrium potential (of a redox half-reaction)	V
E_r	Reversible potential	V
E°	Standard reversible potential	V
E (or E_{app})	(Experimentally) applied potential	V

F	Faraday constant	96.48 kC mol^{-1}
i or i_{corr} (or I_{CORR})	(Corrosion/Measured) current density	A cm^{-2}
I_0	Exchange current	A cm^{-2}
I	Net current at the potential of interest	A cm^{-2}
k_{M1f}	(Pseudo-) 1st order rate coefficient for the forward reaction of $M1$	1/s
k_{M1r}	(Pseudo-) 1st order rate coefficient for the reverse reaction of $M1$	1/s
$[M^{n+}]_{Ar-No-Rad}$	Average concentration of dissolved metal cations in argon-saturated conditions and in the absence of gamma-radiation	M
$[M^{n+}]_{Ar-Rad}$	Average concentration of dissolved metal cations in argon-saturated conditions and in the presence of gamma-radiation	M
$[M^{n+}]_{air-No-Rad}$	Average concentration of dissolved metal cations in air-saturated conditions and in the absence of gamma-radiation	M

$[M^{n+}]_{pH\ 10.6}$	Average concentration of dissolved metal cations at pH 10.6	M
$[M^{n+}]_{pH\ 6.0}$	Average concentration of dissolved metal cations at pH 6.0	M
n	Number of moles	mol
$PD_{t=24h}$	Potentiodynamic polarization after 24 hours of E_{corr} measurement	–
Ox	(Soluble) oxidant	M
R	Ideal gas constant	8.31447 J mol^{-1} K^{-1}
Red	Reductant (reduced form of the oxidant)	M
T	(Absolute) temperature	°C or K
υ_{M1}	Rate of net metal oxidation	mol cm^{-2} s^{-1}
υ_{M1f}	Rate of forward metal oxidation	mol cm^{-2} s^{-1}
υ_{M1r}	Rate of reverse metal oxidation	mol cm^{-2} s^{-1}

Abbreviations	**Term**
AES	Auger electron spectroscopy
$Ag/AgCl$	Silver-silver chloride
air	Stagnant air-saturated solution
Ar	Solution under continuous argon purging

BSEs	Backscattered electrons
BWR	Boiling water reactor
CANDU	Canada Deuterium Uranium
CE	Counter electrode
CRT	Cathode ray tube
CV	Cyclic voltammetry
Gel	Hydrogel
Hg/HgO	Mercury/mercury oxide
Hyd	Hydrolysis
ICP-OES	Inductively coupled plasma optical emission spectrometry
$M^{n+}_{(hyd)}$	Hydrated metal cation
$M(OH)_{(n+1)\ (s)}$	Metal oxide/hydroxide of a higher oxidation state
$M(OH)_{n\ (aq)}$	Dissolved metal hydroxide
$M(OH)_{n\ (gel)}$	Hydrogel network
$M(OH)_{n\ (s)}$	(Solid) (precipitated) metal (oxide/) hydroxide

$M(OH)_{x\ (aq)}^{(n-x)+}$	Hydrolyzed metal cation
$M_{(aq)}^{(n+1)+}$	Dissolved metal cation of a higher oxidation state
$M_{(aq)\|bulk}^{n+}$	Dissolved metal cation in bulk solution
$M_{(aq)\|int\ (sat)}^{n+}$ or $M_{(aq)\|int\ (sat)}^{(n+1)+}$	Dissolved metal cation in interfacial region at saturation limit
$M_{(aq)\|int}^{n+}$	Dissolved metal cation in interfacial region
$M_{(aq)}^{n+}$	Dissolved metal cation
$M_{(m)\|int}^{0}$	Metal atom in metallic site
$M_{(m)\|int}^{n+}$	Oxidized metal cation in metallic site
M^{n+}	Dissolved metal cation
M	Metal
PD	Potentiodynamic
PHWR	Pressurized heavy water reactor
PLWR or PWR	Pressurized light water reactor
ppb	Parts per billion
ppm	Parts per million

RDS	Rate-determining step
RE	Reference electrode
RHE	Reversible hydrogen electrode
Rxn	Redox reaction
SCE	Saturated calomel electrode
SEM	Scanning electron microscopy
SEs	Secondary electrons
Trans	Transport
WE	Working electrode
XPS	X-ray photoelectron spectroscopy

CHAPTER 1

Introduction

1.1 Thesis Motivation

There are several types of nuclear reactor in operation around the world and the most common designs are pressurized light water reactors (PLWR or PWR) and pressurized heavy water reactors (PHWR). CANDU stands for CANada Deuterium Uranium because it was invented in Canada. CANDU reactors are PHWR type and use deuterium oxide (also known as heavy water) as moderator and coolant, and natural uranium as fuel [1], [2]. Canada is home to 19 power reactors providing 14.9% of the country's electricity and approximately 58% of Ontario's electricity [1].

Nickel-based superalloys are used in CANDU, PWR and boiling water reactors (BWR) [3]–[5]. Superalloys are heat-resistant alloys that are able to maintain their high strength at high temperatures. Nickel-based superalloys are one of three main categories of superalloys which can be used in severe environments instead of stainless steels, as nickel can accommodate larger amounts of alloying elements (mainly Cr, Mo and W) in solid solution than iron [6], [7]. The most commonly used nickel-based superalloys in the cores of power reactors are Inconel alloys 600, 625, 718 and X-750 [8]. In nuclear reactors, Inconel X-750 is used as spacers, bolts, guide pins, and other structural components [5].

Inside the reactor core, nickel-based superalloys are exposed to both neutron- and gamma-radiation. The effect of neutron-radiation on the microstructural evolution of Inconel X-750 has been studied via heavy ion irradiation experiments [9]–[11]. The corrosion behaviour of Inconel X-750 in simulated reactor conditions has also been studied [12], [13]. However, there has been no study on the direct effect of gamma-

radiation on the corrosion dynamics of Inconel X-750, to the best of my knowledge. Therefore, a more systematic study is necessary in order to understand the mechanism by which gamma-radiation influences the corrosion rate of Inconel X-750 in aqueous environments.

When exposed to gamma-radiation, water decomposes, resulting in the production of a number of different redox active species, ranging from oxidizing ($\bullet OH$, H_2O_2, O_2) to reducing ($\bullet e_{aq}^-$, $\bullet H$, $\bullet O_2^-$) [14]–[17], as shown in reaction (1, [15]). In the presence of continuous gamma-radiation, these species reach low, steady-state concentrations which control the redox potential of aqueous environments and consequently the corrosion process [14].

$$H_2O \rightsquigarrow OH^1, \bullet e_{aq}^-, \bullet H, H_2, H_2O_2, H^+ \quad (1)$$

In the literature, the direct effect of gamma-radiation on the corrosion behaviours of pure nickel [18], Stellite-6 [19]–[21], and carbon and stainless steels has been studied [22]–[25]. The direct effect of gamma-radiation on the corrosion behaviour of nickel-based superalloys has also been studied [4], [26]. This work aims to improve the understanding of the processes involved in the corrosion of nickel-based superalloys in general and that of Inconel X-750 in particular. In this study, the corrosion behaviour of Inconel X-750 at constant pH values (10.6, 8.4 and 6.0) was studied. Environments with a constant pH is not uncommon is industrial and environmental situation [27]. The results from the study of Stellite-6, which is a cobalt-based superalloy, indicated that gamma-radiation did not change the oxide composition significantly in the range of 25 °C to 150 °C [21]. This study shows that at 25 °C, the corrosion of Inconel X-750 is mainly driven by metal oxidation products accumulated in later stages not by the water radiolysis products. In nuclear reactors, nickel-based superalloys can be exposed to temperatures higher than 150 °C (the maximum temperature investigated in this study) [4]. Therefore,

[1] The reference indicated OH but I believe this to be a typo and that the correct form of this symbol should have been $\bullet OH$.

more electrochemistry and coupon exposure tests, and surface analysis investigations can be performed on Inconel X-750 to better understand the effect of gamma-radiation on metal dissolution and compositional changes of the oxide films at higher temperatures.

1.2 Research Objective and Approaches

The objective of this thesis is to develop a mechanistic understanding of the effects of solution properties on the corrosion dynamics of Inconel X-750. This research aims to evaluate and build upon existing models for the corrosion of nickel-based superalloys in highly oxidizing aqueous solutions in the presence and absence of gamma-radiation. The parameters investigated in this research are solution pH, temperature, oxygen concentration, and the effect of gamma-radiation. The corrosion dynamics are investigated using a combination of electrochemical techniques and coupon exposure tests. The electrochemical techniques include corrosion potential ((E_{corr}) measurement) and cyclic voltammetry (CV). The coupon exposure tests are performed using Inconel X-750 coupons immersed in solutions in sealed quartz vials. The post-test analyses carried out are dissolved metal analysis by inductively coupled plasma optical emission spectrometry (ICP-OES) and surface analysis using scanning electron microscopy (SEM). The results from these studies are discussed in Chapters 4, 5 and 6.

1.3 Thesis Outline

- Chapter 1: This Chapter describes the thesis motivation, objectives, and thesis outline.
- Chapter 2: This Chapter contains the materials background, theoretical background and a literature review in $Fe - Cr - Ni$ systems.
- Chapter 3: This Chapter discusses the techniques used in this study.
- Chapter 4: *The Effects of Solution pH, Temperature, and Redox and Transport Conditions on the Corrosion Evolution of Inconel X-750*

In this Chapter, the elementary steps that occur during corrosion of a pure metal (e.g., Ni, Cu) are briefly summarized [18], [28]. This theoretical understanding is applied to Inconel X-750, which contains more than one type of metal atom and is likely covered with an air-formed oxide. In this Chapter, E_{corr} measurement experiments and the corrosion evolution of Inconel X-750 are studied. The parameters studied are: solution pH (10.6, 8.4 and 6.0), temperature (25 °C and 80 °C), and redox and transport conditions (solution under continuous argon purging, stagnant air-saturated solution, and solution under gamma-radiation).

– Chapter 5: *Time-Dependent Metal Oxidation Rate: The Effects of Solution pH, Temperature, and Redox and Transport Conditions*

In this Chapter, the time-dependent kinetics of Inconel X-750 corrosion are studied. For this purpose, potentiodynamic (PD) polarization after 24 hours of E_{corr} measurement ($PD_{t=24}$) and cyclic voltammetry without a prior E_{corr} measurement ($CV_{t=0}$) were performed. The parameters studied were: solution pH (10.6, 8.4 and 6.0), and solution redox and transport conditions (i.e., solution under continuous argon purging and stagnant air-saturated solution). The $CV_{t=0}$ and $PD_{t=24}$ results are compared with the 1st and 2nd (pseudo-) steady-states from the E_{corr} measurement experiments and the key findings are discussed.

– Chapter 6: *Time-Dependent Corrosion Behaviour of Inconel X-750 at 25 °C – 150 °C: The Effects of pH, Temperature, Oxygen Concentration and Gamma-Radiation*

In this Chapter coupon exposure tests were performed to investigate the effects of gamma-radiation and pH on the kinetics of oxide formation and metal dissolution of Inconel X-750 in borate buffer solutions at 25 °C and 150 °C for different exposure times. In addition, the effect of temperature (i.e., 25 °C versus 80 °C) in argon-saturated conditions and the effect of oxygen concentration (i.e., argon-saturated versus air-saturated) at 80 °C were studied. After the test duration, the solution was analyzed by

ICP-OES to determine the concentrations of dissolved metal ions while the morphologies of the oxides formed on the corroded coupons were characterized by SEM.

– Chapter 7: *Thesis Summary and Future Work*

This Chapter summarizes the key findings on the corrosion dynamics of Inconel X-750 and discusses future work.

1.4 References

[1] Canadian Nuclear Association, "The Canadian Nuclear Factbook 2020" Accessed: Feb. 26, 2021. [Online]. Available: https://cna.ca/wp-content/uploads/2019/08/2020-Factbook-EN-digital.pdf

[2] The Essential CANDU, A Textbook on the CANDU Nuclear Power Plant Technology, Editor-in-Chief Wm. J. Garland, Chapter 1, "Introduction to Nuclear Reactors", by R. Chaplin, University Network of Excellence in Nuclear Engineering (UNENE), ISBN 0-9730040. Retrieved from https://www.unene.ca/education/candu-textbook on 19 Dec. 2021.

[3] H. K. Zhang, Z. Yao, G. Morin, and M. Griffiths, "TEM characterization of in-reactor neutron irradiated CANDU spacer material Inconel X-750," *Journal of Nuclear Materials*, vol. 451, no. 1, pp. 88–96, Aug. 2014, doi: 10.1016/j.jnucmat.2014.03.043.

[4] M. Momeni, "Gamma-Radiation Induced Corrosion of Alloy 800," The University of Western Ontario, 2017. Electronic Thesis and Dissertation Repository, Available: https://ir.lib.uwo.ca/etd/5011

[5] T. Kekkonen and H. Hänninen, "The effect of heat treatment on the microstructure and corrosion resistance of inconel X-750 alloy," *Corrosion Science*, vol. 25, no. 8, pp. 789–803, Jan. 1985, doi: 10.1016/0010-938X(85)90011-3.

[6] W. F. Smith, *Structure and Properties of Engineering Alloys*, 2nd Edition. McGraw-Hill, 1993.

[7] J. R. Davis, Ed., “Nickel and Nickel Alloys,” in *Metals Handbook Desk Edition*, 2nd Edition., ASM International, 1998, pp. 609–615. doi: 10.31399/asm.hb.mhde2.a0003147.

[8] M. Griffiths, “The Effect of Irradiation on Ni-Containing Components in CANDU® Reactor Cores: A Review,” *Nuclear Review*, pp. 1–16, May 2014, doi: 10.12943/ANR.2013.00001.

[9] H. K. Zhang, Z. Yao, C. Judge, and M. Griffiths, “Microstructural evolution of CANDU spacer material Inconel X-750 under in situ ion irradiation,” *Journal of Nuclear Materials*, vol. 443, no. 1, pp. 49–58, Nov. 2013, doi: 10.1016/j.jnucmat.2013.06.034.

[10] H. K. Zhang, Z. Yao, M. R. Daymond, and M. A. Kirk, “Elevated temperature irradiation damage in CANDU spacer material Inconel X-750,” *Journal of Nuclear Materials*, vol. 445, no. 1, pp. 227–234, Feb. 2014, doi: 10.1016/j.jnucmat.2013.11.008.

[11] H. K. Zhang, Z. Yao, M. A. Kirk, and M. R. Daymond, “Stability of Ni_3(Al, Ti) Gamma Prime Precipitates in a Nickel-Based Superalloy Inconel X-750 Under Heavy Ion Irradiation,” *Metallurgical and Materials Transactions A*, vol. 45, no. 8, pp. 3422–3428, Jul. 2014, doi: 10.1007/s11661-014-2309-y.

[12] S. Tuzi, K. Göransson, S. M. H. Rahman, S. G. Eriksson, F. Liu, M. Thuvander, and K. Stiller, “Oxide evolution on Alloy X-750 in simulated BWR environment,” *Journal of Nuclear Materials*, vol. 482, pp. 19–27, Dec. 2016, doi: 10.1016/j.jnucmat.2016.09.026.

[13] S. Tuzi, H. Lai, K. Göransson, M. Thuvander, and K. Stiller, “Corrosion of pre-oxidized nickel alloy X-750 in simulated BWR environment,” *Journal of Nuclear Materials*, vol. 486, pp. 350–360, Apr. 2017, doi: 10.1016/j.jnucmat.2017.01.051.

[14] J. C. Wren, “Steady-State Radiolysis: Effects of Dissolved Additives,” in *Nuclear Energy and the Environment*, vol. 1046, American Chemical Society, 2010, pp. 271–295.

[15] J. M. Joseph, B. Seon Choi, P. Yakabuskie, and J. Clara Wren, “A combined experimental and model analysis on the effect of pH and O_2(aq) on γ-radiolytically

produced H_2 and H_2O_2," *Radiation Physics and Chemistry*, vol. 77, no. 9, pp. 1009–1020, Sep. 2008, doi: 10.1016/j.radphyschem.2008.06.001.

[16] J. W. T. Spinks, *An Introduction to Radiation Chemistry*, 2nd Edition. John Wiley & Sons, Inc., 1976.

[17] G. S. Was, "Environmentally Assisted Cracking of Irradiated Metals and Alloys," in *Fundamentals of Radiation Materials Science*, Berlin, Heidelberg: Springer Berlin Heidelberg, 2007, pp. 765–814. doi: 10.1007/978-3-540-49472-0_15.

[18] R. Karimihaghighi, "Non-Linear Effects of Solution Parameters and Gamma Radiation on Nickel Oxidation Dynamics," The University of Western Ontario, 2021. Electronic Thesis and Dissertation Repository, Available: https://ir.lib.uwo.ca/etd/7789

[19] M. Behazin, J. J. Noël, and J. C. Wren, "Combined Effects of pH and γ-Irradiation on the Corrosion of Co-Cr Alloy Stellite-6," *Electrochimica Acta*, vol. 134, pp. 399–410, Jul. 2014, doi: 10.1016/j.electacta.2014.04.079.

[20] M. Behazin, M. C. Biesinger, J. J. Noël, and J. C. Wren, "Comparative study of film formation on high-purity Co and Stellite-6: Probing the roles of a chromium oxide layer and gamma-radiation," *Corrosion Science*, vol. 63, pp. 40–50, Oct. 2012, doi: 10.1016/j.corsci.2012.05.007.

[21] M. Behazin, "Radiation Induced Corrosion of Stellite-6," The University of Western Ontario, 2014. Electronic Thesis and Dissertation Repository, Available: https://ir.lib.uwo.ca/etd/2434

[22] D. Guo, "Corrosion Dynamics of Carbon Steel in Used Fuel Container Environments," The University of Western Ontario, 2018. Electronic Thesis and Dissertation Repository, Available: https://ir.lib.uwo.ca/etd/5897

[23] K. Ishigure, N. Fujita, T. Tamura, and K. Oshima, "Effect of Gamma Radiation on the Release of Corrosion Products from Carbon Steel and Stainless Steel in High Temperature Water," *Nuclear Technology*, vol. 50, no. 2, pp. 169–177, Sep. 1980, doi: 10.13182/NT80-A32543.

[24] Q. W. Knapp and J. C. Wren, “Film formation on type-316L stainless steel as a function of potential: Probing the role of gamma-radiation,” *Electrochimica Acta*, vol. 80, pp. 90–99, Oct. 2012, doi: 10.1016/j.electacta.2012.06.090.

[25] K. Daub, X. Zhang, J. J. Noël, and J. C. Wren, “Gamma-radiation-induced corrosion of carbon steel in neutral and mildly basic water at 150 °C,” *Corrosion Science*, vol. 53, no. 1, pp. 11–16, Jan. 2011, doi: 10.1016/j.corsci.2010.09.048.

[26] A. Y. Musa and J. C. Wren, “Combined effect of gamma-radiation and pH on corrosion of Ni–Cr–Fe alloy inconel 600,” *Corrosion Science*, vol. 109, pp. 1–12, Aug. 2016, doi: 10.1016/j.corsci.2016.03.015.

[27] R. G. Kelly, J. R. Scully, D. Shoesmith, and R. G. Buchheit, *Electrochemical Techniques in Corrosion Science and Engineering*. Marcel Dekker, Inc., 2003.

[28] M. Naghizadeh, “Copper Corrosion Dynamics under Deep Geologic Repository Conditions,” The University of Western Ontario. Accessed: Aug. 12, 2021. Electronic Thesis and Dissertation Repository, Available: https://ir.lib.uwo.ca/etd/7894/

CHAPTER 2

Technical Background and Literature Review

2.1 Nickel-Based Superalloys in Nuclear Reactors

Nickel and nickel-based superalloys are able to maintain their integrity in high-temperature applications and corrosive environments. These alloys have a wide range of applications in rocket engines, nuclear reactors, and aircraft structures [1]–[3].

A "nuclear reactor" is the name given to the device or structure in which a controlled nuclear reaction takes place [4]. The core of the reactor is the place where the nuclear fuel is placed and where the nuclear reaction takes place [4]. In nuclear power plants, the heat energy from the fission of uranium (^{235}U) is converted into high-quality steam [5].

There are several types of nuclear reactor in operation around the world and the most common designs are pressurized light water reactors (PLWR or PWR) and pressurized heavy water reactors (PHWR). CANDU stands for CANada Deuterium Uranium because it was invented in Canada. CANDU reactors are PHWR type. As of 2018, there have been about 449 nuclear reactors around the world, about half of which corresponded to boiling water reactors (BWR) and the other half to PWR [6]–[8].

The reactor core also contains a moderator to slow the neutrons released by the fission of uranium atoms. In some cases, the moderator is also the coolant [4]. The primary coolant is circulated through the core, where it absorbs heat, through the reactor coolant piping, and to the steam generators where it transfers its heat to a second, high-purity water loop. The water in the secondary loop is heated to steam, which is used to

drive the turbine. The steam generators in PWRs create a barrier between the primary (i.e., radioactive) and secondary (nonradioactive) systems [5].

In both BWR and PWR, ordinary water (light water) is used as both the coolant and the moderator. Likewise, both BWR and PWR use enriched uranium as fuel—with a slightly higher enrichment in a PWR [4]. However, there are some dissimilarities between PWR and BWR [4]. PWR vessels (including the reactor vessel, steam generator shells, and pressurizer) operate at pressures of the order of 13.8 MPa and temperatures of up to 330 °C [5]. BWR reactor pressure vessels operate at much lower internal pressures than those of a PWR, of the order of the saturation pressure of steam at reactor operating temperatures (6.89 MPa at 288 °C). As a result, BWR reactor vessels can be much larger than those of PWRs [5].

CANDU reactors use unenriched uranium [4]. CANDU reactors use heavy water as its moderator and coolant. Heavy water has the advantage of absorbing fewer neutrons than normal water. Therefore, it is possible to sustain a nuclear reaction without the need to enrich the uranium fuel. CANDU reactors have the additional advantage that they can be refueled without the need to shut down. The heavy water coolant in CANDU reactors is pressurized to prevent it from boiling [4].

In CANDU reactors, the hot pressure tube and relatively cold calandria tube are separated by four spacers which are spread over the 6-meter span of the fuel channel. The spacers remain in the reactor core for the duration of the reactor life. The spacers are responsible for maintaining carbon-dioxide-filled gap between the pressure tube and calandria tube [9].

Inconel alloys 600, 625, 718 and X-750 are the most commonly used nickel-based superalloys in the cores of power reactors [9]. Inconel alloys 600, 690 and 800 have been used since the end of 80s in steam generator tubes due to their good heat transfer properties and excellent resistance to all forms of corrosion [5], [8]. Inconel X-750 is used as spacers in CANDU reactors to separate hot pressure tube (~250 °C – 310 °C) and cold calandria tube (~60 °C – 80 °C), **Figure 2.1** [10].

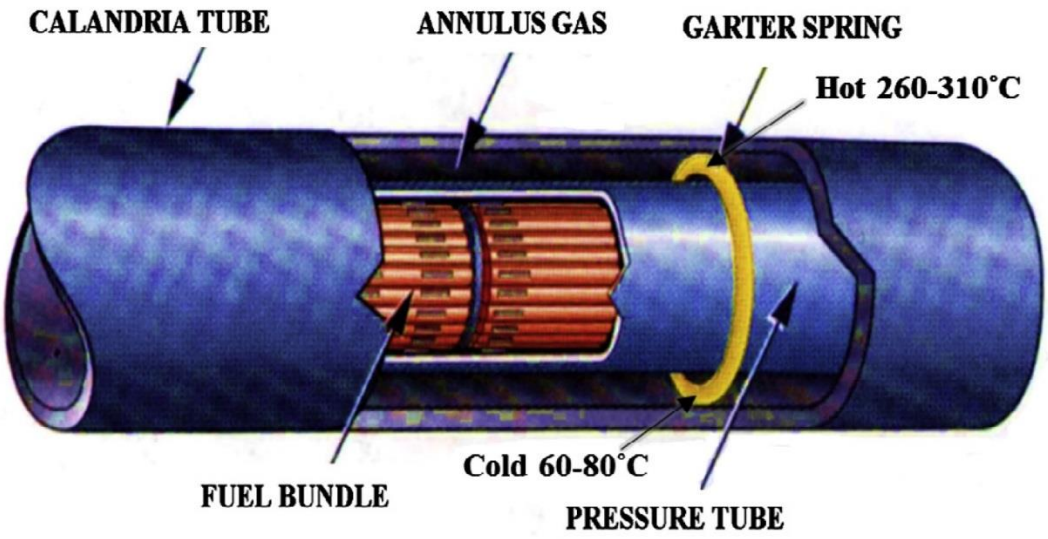

Figure 2.1 Schematic showing the spacer temperature range in a CANDU fuel channel[1] [10].

The effect of neutron-radiation on the microstructural evolution of Inconel X-750 has been studied via heavy ion irradiation experiments [11]–[13]. However, the existing literature on the effect of ionizing radiation such as gamma-radiation on the corrosion behaviour of nickel-based superalloys is limited [14], [15].

Inconel alloys 600 and 690 are used in steam generators of PWRs due to their ability to form an oxide film that can limit the cation release in the primary loop. The diffusion of nickel, cobalt and other cations through the oxide film can lead to their release in the primary water. The circulation of these cations from the steam generator to the core can result in their activation under a neutron flux (reactions 1 and 2, [8]):

$$^{58}Ni + \mathrm{n} \rightleftharpoons {}^{58}Co + \mathrm{p} \quad (1)$$

[1] This figure was published in Journal of Nuclear Materials, Vol. 451, Issues 1–3, H. K. Zhang, Z. Yao, G. Morin, and M. Griffiths, TEM characterization of in-reactor neutron irradiated CANDU spacer material Inconel X-750, 88–96, Copyright Elsevier (2014).

$$^{59}Co + \text{n} \rightleftharpoons {}^{60}Co + \gamma \quad (2)$$

where n and p represent a neutron and a proton, respectively [8], [16].

Neutron activation results in the production of radioactive elements. These radioactive corrosion products carried through the coolant could later deposits on the wall of the heat transport tubing outside the reactor core. This can create radioactive hot spots outside the core which can pose a safety concern for reactor maintenance workers and make any maintenance activities very expensive [8], [14], [17].

2.2 Principles of Corrosion

Aqueous corrosion is an electrochemical process occurring at the interface between a metal and an aqueous solution. For corrosion to occur, an oxidation reaction and a reduction reaction must occur simultaneously [18]. Anodic (or oxidation) and cathodic (or reduction) reactions are represented by reactions 3 and 4, respectively.

$$M \rightarrow M^{n+} + ne^{-} \quad (3)$$

$$Ox + ne^{-} \rightarrow Red \quad (4)$$

where M denotes a metal and M^{n+} a dissolved metal cation while Ox denotes a soluble oxidant and Red the reduced form of the oxidant that may or may not be a soluble species [18].

The difference in equilibrium potentials for the half-reactions determines whether or not a particular corrosion reaction can proceed, as shown in **Figure 2.2**[1] [18], [19]. Therefore, the thermodynamic driving force (ΔE_{therm}) for corrosion, [Eq 1, [18]], is:

[1] The vertical displacement in this figure indicates the electrochemical potential.

$$\Delta E_{therm} = E^{e}_{Ox/Red} - E^{e}_{M/M^{n+}} \quad \text{[Eq 1]}$$

where $E^{e}_{M/M^{n+}}$ is the equilibrium potential of the material in the environment of interest and $E^{e}_{Ox/Red}$ is the redox potential of the environment [19]. For each half-reaction, the Butler-Volmer equation, [Eq 2, [18]], predicts the current at the potential of interest.

$$I = I_0 \{\exp\left(\frac{\alpha F}{RT}\eta\right) - \exp\left(1-\alpha\right)\frac{F}{RT}\,\eta\} \quad \text{[Eq 2]}$$

where I is the net current at the potential of interest, I_0 is the exchange current, F is the Faraday constant, R is the ideal gas constant, T is the absolute temperature and α is the transfer or symmetry coefficient, generally assumed to be 0.5. The term η is the overpotential, defined by $\eta = \left(E - E^{e}_{M/M^{n+}}\right)$, where E is the experimentally applied potential[1] [18].

This coupling between the anodic and cathodic reactions occurs at a single potential, known as the corrosion potential (E_{corr}). There are situations where the anodic reaction is accompanied by more than one cathodic reaction, such as in aerated solutions where both proton reduction ($2H^+ + 2e^- \rightarrow H_2$) and oxygen reduction ($O_2 + 2H_2O + 4e^- \rightarrow 4OH^-$) reactions can occur [18]. Corrosion reactions involve the coupling of an anodic half-reaction to a cathodic half-reaction. This coupling of half-reactions produces an equation of the same form as the Butler-Volmer equation. This expression, which is known as the Wagner-Traud equation, [Eq 3, [18]], relates the measured current to the corrosion current (i_{corr}) [18], [20]. The net current that would be measured by a potentiostat during a polarization experiment is given by:

[1] I believe that the term 'overpotential' is also applicable to naturally corroding conditions and in the absence of an applied potential. Therefore, the 'experimentally applied potential' should be replaced with 'electrode potential'.

$$i = i_{corr}\ \{\exp\left(\frac{\alpha_a F\eta}{RT}\right) - \exp\left(\frac{-\alpha_c F\eta}{RT}\right)\} \qquad \text{[Eq 3]}^{1}$$

where i and i_{corr} represent the current densities. The Wagner-Traud equation considers the difference from E_{corr} rather than equilibrium potential of a redox half-reaction (E_{rxn}^{eq}) and the current density at zero 'overpotential' is i_{corr} instead of i_0 [18], [20].

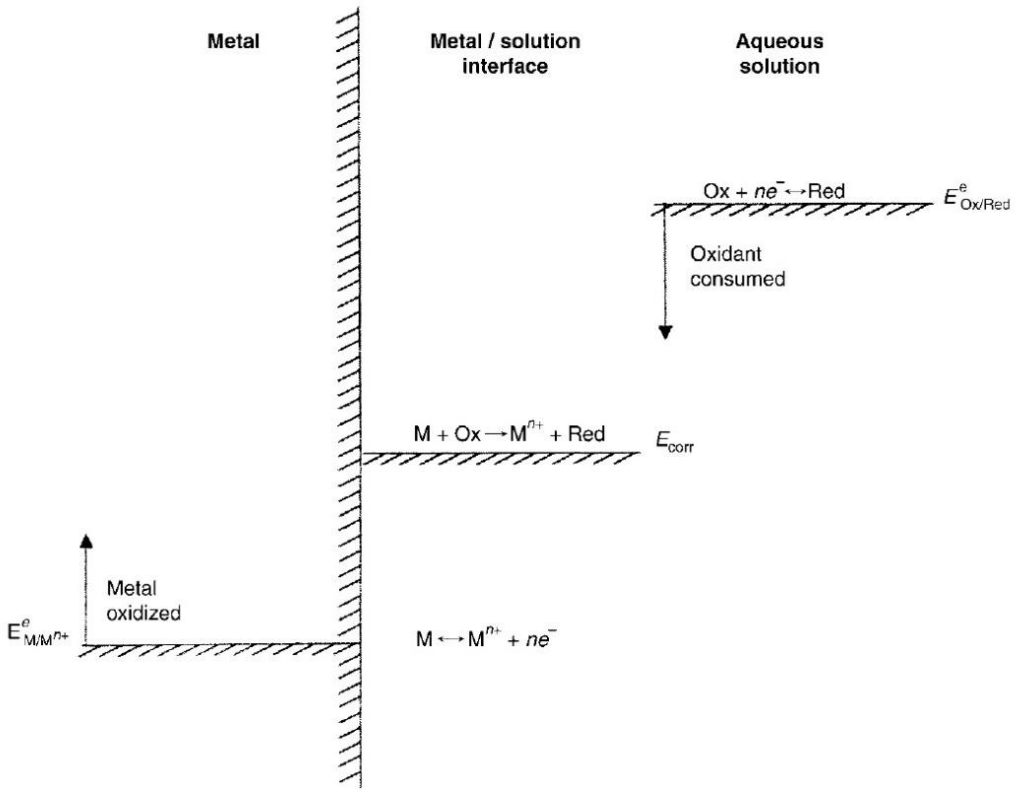

Figure 2.2 The thermodynamic driving force for corrosion across a metal/aqueous solution interface in the presence of a soluble oxidant, Ox. The values of the equilibrium potentials are shown schematically (reprinted with permission of ASM International. All rights reserved. www.asminternational.org) [18].

[1] I believe that the term 'η' in [Eq 3] should be replaced with '$E_{app} - E_{corr}$' where E_{app} is the applied potential. This is because the potential quantity is not the overpotential, but the difference between the applied potential and E_{corr}.

Electrode reactions can only take place at the interface between the electrode and the solution. Electrode reactions tend to make the solution composition adjacent to the electrode different from that further away [21]. The solution volume very close to the electrode must differ in structure from the characteristics of more remote zones. This is because the solution volume within a few molecular layers from the electrode is forced to interact with the electrode. Likewise, the distribution of mobile electrons at electrode/solution interface must differ from the distribution found in the interior of the electrode [21].

Evolution of the corrosion process with time could change the equilibrium potentials for the half-reactions; i.e., the driving force for corrosion would not necessarily remain constant [19]. This will be explained further in the next section (E_{corr} Evolution).

Corrosion process involves several elementary reactions. Any one or combination of these reactions can control the overall corrosion process [17], [18], [22]. The interfacial kinetics of either anodic or cathodic reactions could be rate controlling. For example, when the concentration of oxidant is low and the cathodic and anodic reactions are fast, the transport of oxidant to the cathodic site can be rate determining. On the other hand, if the anodic reaction is fast and the rate of dissolved metal cations from the interfacial region to the bulk solution is slow, the interfacial region becomes supersaturated with dissolved metal cations which results in the precipitation of oxides, hydroxides or metal salts. The precipitated corrosion products are likely to be porous and could control the transport of dissolved metal cation [18]. The properties of oxides/hydroxides that form on pure Fe, Cr, and Ni as well as the complex oxide/hydroxide system of $Fe - Cr - Ni$ alloys are discussed in detail later in this Chapter.

2.3 E_{corr} Evolution

Determining the evolution of a corrosion process with time may require a significant amount of research. However, a preliminary understanding can be gained

from a knowledge of the system corrosion potential, E_{corr}, and how it changes with time [19]. The E_{corr} adopted by the system is dictated by the relative rates of anodic and cathodic reduction reactions. While E_{corr} yields no quantitative information on the rate of the overall corrosion process, it is a good qualitative indicator of the evolution of corrosion kinetics with time [19].

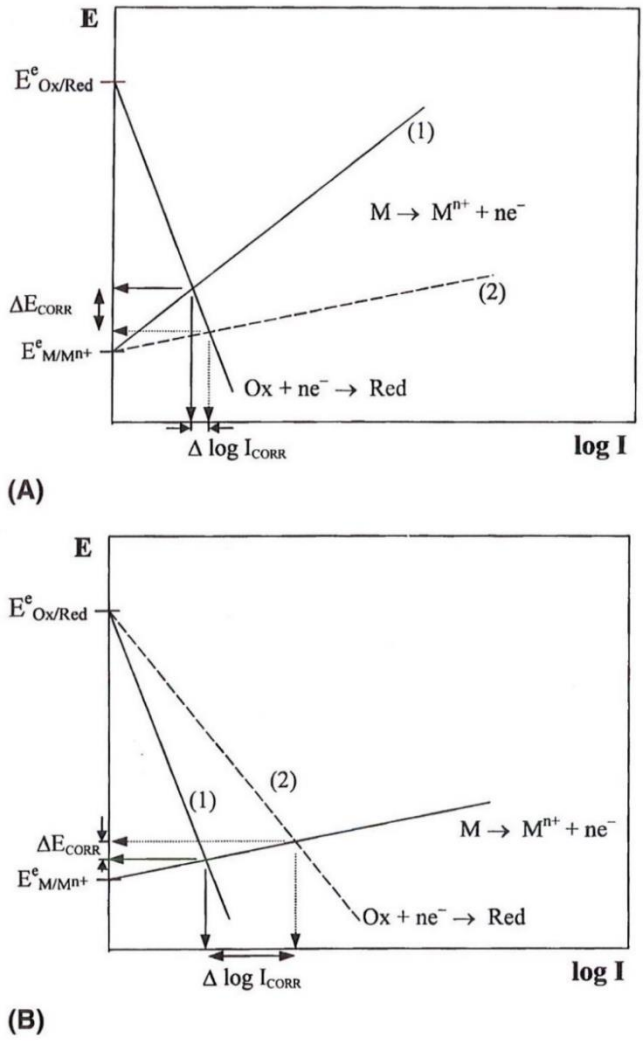

Figure 2.3 (A) Evans diagram illustrating the change in I_{CORR} and E_{CORR} for the increase in rate (from 1 to 2) of a fast anodic reaction coupled to a slow cathodic reaction. (B) Evans diagram for the same combination, illustrating the influence of a change in rate of the slow cathodic reaction (from 1 to 2)[1] [19].

[1] Republished with permission of Taylor & Francis, from Electrochemical Techniques in Corrosion Science and Engineering, R. G. Kelly, J. R. Scully, D. Shoesmith, and R. G. Buchheit, 2002; permission conveyed through Copyright Clearance Center, Inc.

The proximity of E_{corr} to either $E^e_{M/M^{n+}}$ or $E^e_{Ox/Red}$ can indicate which one of the two half-reactions may be rate-determining. This is illustrated in **Figure 2.3A**, which shows the combination of a fast anodic half-reaction and a slow cathodic half-reaction. The corrosion of iron in aerated neutral solution is a good example of such a combination. The influence of a change in rate of the slow cathodic reaction is shown in **Figure 2.3B** [19].

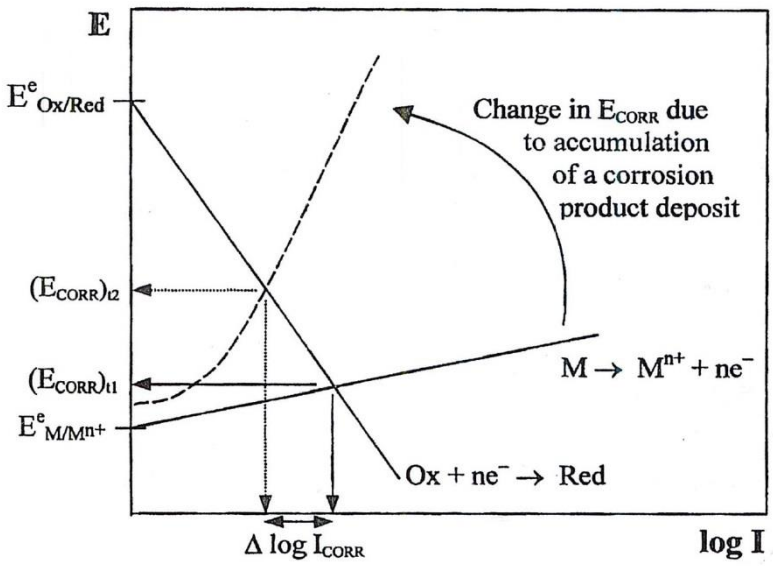

Figure 2.4 Evans diagram for the coupling of a fast anodic reaction to a slow cathodic reaction, illustrating the influence of the formation of a corrosion product deposit[1] [19].

For a fast anodic reaction coupled to a slow cathodic reaction, a change in the rate of the anodic reaction (line 1 to 2 in **Figure 2.3A**) has little effect on the corrosion rate but a measurable effect on E_{corr}, whereas the opposite is true for a change in the cathodic reaction rate (line 1 to 2 in **Figure 2.3B**) [19].

[1] Republished with permission of Taylor & Francis, from Electrochemical Techniques in Corrosion Science and Engineering, R. G. Kelly, J. R. Scully, D. Shoesmith, and R. G. Buchheit, 2002; permission conveyed through Copyright Clearance Center, Inc.

In an environment with a constant redox conditions (e.g., permanently aerated and/or constant pH), E_{corr} could shift in the positive direction. As corrosion progresses, the precipitation of a corrosion product could polarize (i.e., increase the overpotential, η, for) the anodic half-reaction, as illustrated in **Figure 2.4**[1]. This polarization may result from an anodic concentration polarization, as the rate of transport of dissolved metal species away from the corroding surface becomes steadily inhibited by the thickening of the surface deposit; i.e., the anodic half-reaction becomes transport-controlled [19].

The introduction of transport effects due to the precipitation of corrosion products would not necessarily be confined to one half-reaction. The transport of the oxidant to the corrosion site could also be polarized, as shown in **Figure 2.5**. In this situation, the shift in E_{corr} due to anodic concentration polarization would be offset by a similar effect of the surface deposit on the cathodic half-reaction [19].

In neutral solutions, the reduction of oxygen is important for many metals. This is because the amount of dissolved oxygen will determine the corrosion rate. The bulk oxygen concentration in room temperature aqueous solutions is low—between 6 to 8 ppm depending on the presence or absence of other dissolved species [19], [23], [24]. In deaerated water, this amount decreases to a reported value of 75 ppb [25]. There is net diffusion of new electrolyte molecules into the depleted zone from more remote regions due to the Brownian motion of molecules which tends to homogenize the solution [21]. In catholically polarized electrodes, the rate of oxygen reduction reaction can be limited due to the low concentration of dissolved oxygen. Usually, mass-transport-controlled processes are strongly influenced by the solution velocity and agitation—unlike charge-transfer-controlled processes which are not affected by solution agitation. Therefore, fluid flow can increase the supply of oxygen in the reacting interface from the bulk solution and as a result, the rate of oxygen reduction reaction can increase [19].

[1] The arrow in this diagram should point to the intersection of the lower and upper lines and to the intersection of the curved dashed line and the upper line.

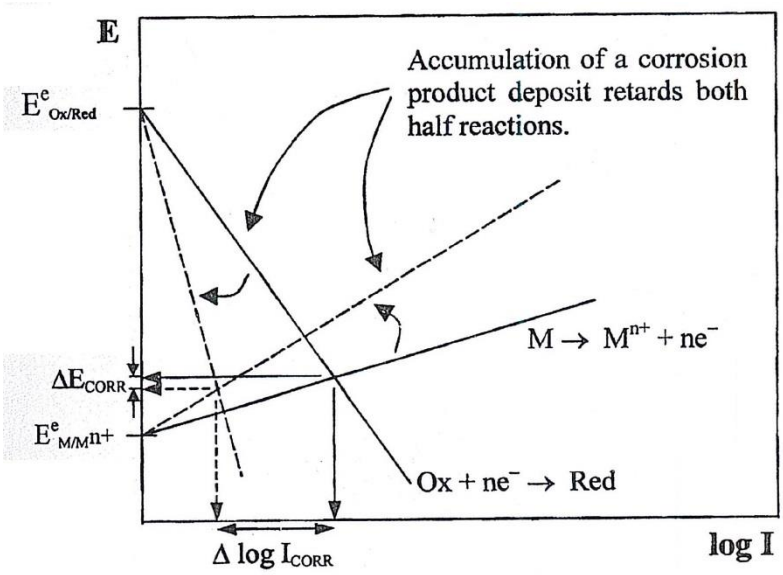

Figure 2.5 Evans diagram illustrating the influence on I_{CORR} and E_{CORR} of a corrosion product deposit that affects both the anodic and cathodic half-reactions. The solid lines are for no deposit; the dashed lines illustrate the changes in the presence of the deposit[1] [19].

Oxygen reduction reaction on platinum is nearly ten times slower than hydrogen reduction reaction. The exchange current density of oxygen reduction reaction is very low—even on an electrode like platinum. This is because the charge transfer is slowed down considerably due to the oxide film formation on the electrode and the electrode acts as a less efficient catalyst for oxygen reduction reaction [26].

2.4 Oxide/Hydroxide Films in $Fe - Cr - Ni$ Systems

Oxides can generally be categorized into two groups: (1) compact, anhydrous oxides in which oxygen is present only as bridging atoms between metal cations; and, (2)

[1] Republished with permission of Taylor & Francis, from Electrochemical Techniques in Corrosion Science and Engineering, R. G. Kelly, J. R. Scully, D. Shoesmith, and R. G. Buchheit, 2002; permission conveyed through Copyright Clearance Center, Inc.

dispersed, hydrous oxides where oxygen is present not just as bridging atoms between metal cations, but also as O^-, OH, and OH_2 species, i.e., in coordinated terminal group form. When the latter group is in contact with aqueous media, it usually contains considerable quantities of loosely bound and trapped water, plus, occasionally, electrolyte species [27].

Generally, oxides can form via a number of pathways. *Direct* film formation occurs via the reaction of the metal, M, with water to form an adsorbed oxygen layer or compact oxide, MO_x, reaction 5, [28].

$$M_{(s)} + xH_2O_{(l)} \rightarrow MO_{x\,(s)} + 2xH^+_{(aq)} + 2xe^- \quad (5)$$

On the other hand, an insoluble oxide can form *indirectly* through a dissolution-precipitation process. This process has several steps and starts with metal oxidation to form metal cations in the solution [28].

2.4.1 Iron and chromium

Tamura investigated the atmospheric corrosion of iron and steel and calculated the solubilities of corrosion products as a function of pH, as seen in **Figure 2.6** [29]. The driving force for dissolution is defined by the extent of solution undersaturation with respect to the oxide. Undersaturation is a necessity for dissolution just as supersaturation is for precipitation [30].

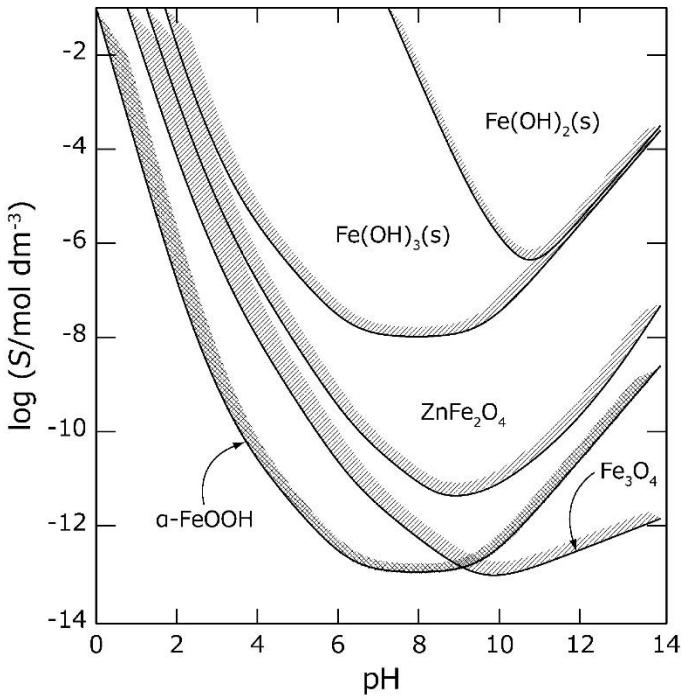

Figure 2.6 Solubilities of corrosion products as functions of pH[1] [29].

The dissolution of highly crystalline Fe^{III} oxides at atmospheric pressure requires a pH < 1 even at 70 °C [30]. The order of solubility is Lepidocrocite ($\gamma - FeOOH$) > maghemite ($\gamma - Fe_2O_3$) > hematite ($\alpha - Fe_2O_3$) [30]. Lepidocrocite dissolves more rapidly than hematite due to its lower thermodynamic stability. Usually, magnetite ($Fe^{II}Fe_2^{III}O_4$) dissolves faster than pure Fe^{III} oxides. This is due to its Fe^{II} content and the fact that Fe^{III} occurs in octahedral and tetrahedral positions [30]. The first step in dissolution of Fe^{III} oxide is the adsorption of proton by surface OH which results in the $Fe - O$ bond weakening and eventually the detachment of Fe from the bulk oxide [30].

David and Welch prepared and compared the magnetite samples formed in the presence and absence of water. The former readily yielded γ-ferric oxide on oxidation whereas the latter oxidized with difficulty and yielded α-oxide directly. They suggested

[1] This figure was published in Corrosion Science, Vol. 50, Issue 7, H. Tamura, The role of rusts in corrosion and corrosion protection of iron and steel, 1872–1883, Copyright Elsevier (2008).

that a small proportion of combined water is essential to the stability of the spinel-type structure γ-ferric oxide without which the γ-ferric structure is destroyed [31].

Sunseri et al. studied pure chromium and concluded that the first step in the growth of a stable passive film is the formation of an oxy-hydroxide phase with a composition near that of $Cr(OH)_3$ [32]. Pure Cr_2O_3 is never formed in aqueous solutions at any pH value and electrode potential within the passivity range [32]. The compositions of passive films on chromium depend on the potential and the electrolyte pH [33].

Sass and Rai showed that $Cr_xFe_{1-x}(OH)_3$ forms readily at room temperature and the dissolved Cr in equilibrium with it is several orders of magnitude lower in concentration than when in equilibrium with $Cr(OH)_3$ [34].

Lister et al. examined the oxide film that developed on the surface of type 304 stainless steel in lithiated high temperature water (pH 10.3) and observed two layers. It was found that the precipitated outer layer of iron-rich oxide crystals afforded no protection against corrosion. In addition, once a protective layer of chromium-rich oxide is established, the nucleation of the outer layer is suppressed [16].

2.4.2 Nickel and nickel-based superalloys

Commercially pure nickel has excellent resistance to many corrosive environments [1]. From the standpoint of corrosion, nickel is less readily oxidized than iron and chromium. This results in the enrichment of metallic nickel in the metal closest to the metal/oxide interface. In nickel-based superalloys, chromium and molybdenum are used to improve the existing passive film on nickel surface [35].

Mellsop et al. [36] attempted to further develop the nickel phase transformations model that was first introduced by Bode is in 1966 [37]. According to Mellsop et al., it is neither $\alpha - Ni(OH)_2$ nor $\beta - Ni(OH)_2$ which is formed from metallic nickel at low potentials, but a third phase which is referred to as $\alpha(II)_{compact}$. **Figure 2.7** shows the updated nickel oxidation diagram in which the $\alpha(II)_{compact}$ phase is included. The

compact $Ni(II)$ phase could have a structure part way between NiO and $\alpha - Ni(OH)_2$ [36].

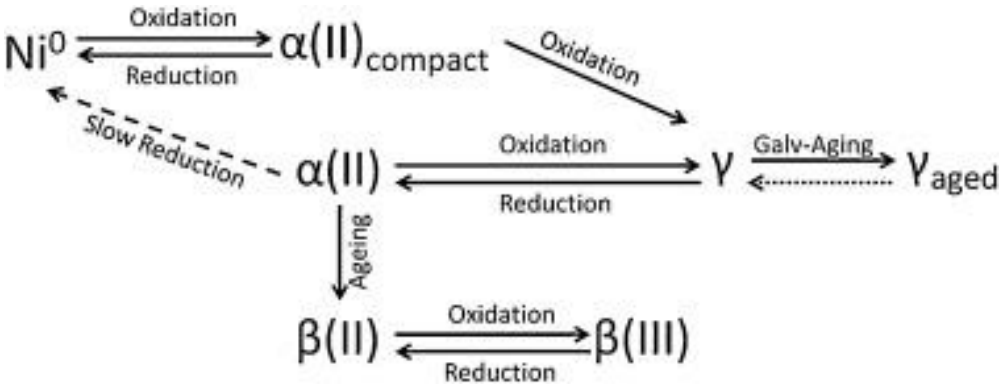

Figure 2.7 Updated model of nickel phases[1] [36].

The oxide formed on the surface of nickel-based superalloys exposed to simulated reactor conditions has been extensively studied [38]–[40]. The oxide film grown in pressurized water on nickel-based superalloys has a duplex structure: an internal film enriched in chromium (a film of iron and nickel mixed chromite) and an external noncontinuous film enriched in iron and nickel (composed of two different phases: nickel ferrite crystals and nickel hydroxide nodules). The external film is assumed to be formed by precipitation process [8].

Tuzi et al. studied the oxide evolution on Alloy X-750 with and without pre-oxidization treatment. In Alloy X-750 without a pre-oxidization treatment, they proposed a mechanism for oxide formation and observed a multi-layer film composed of two outer

[1] This figure was published in Electrochimica Acta, Vol. 168, S. R. Mellsop, A. Gardiner, B. Johannessen, and A. T. Marshall, Structure and transformation of oxy-hydroxide films on Ni anodes below and above the oxygen evolution potential in alkaline electrolytes, 356-364, Copyright Elsevier (2015).

layers of spinel crystals, an intermediate layer of mixed nickel and titanium-rich oxides, and an inner layer of oxidized based metal [38], [39].

Qiu et al. studied the electrochemical behaviour of Alloy 600 at 290 °C and concluded that the oxide film had a duplex structure, consisting of an inner layer and an outer layer. It was also found that increasing dissolved hydrogen content resulted in a thinner inner layer and shifted the E_{corr} to more negative potentials [40].

Ru et al. investigated the influence of iron content ($0-9$ at.%) on oxide film formation in $Ni-Cr-xFe$ alloys in simulated PWR solution [41]. They observed polyhedral particles on the 500 h samples which they characterized as spinel oxides: $NiFe_2O_4$, $NiCr_2O_4$ and $FeCr_2O_4$. The results indicated that increasing the Fe content of the alloy increased the Fe content of the spinel particles. In addition, increasing the Fe content in the alloy matrix can increase the iron cation concentration gradient between the matrix/film interface and the film/solution interface, accelerate the transport rate of iron cations, and increase the transport rate of oxygen into the inner oxide layer, this accelerating the growth of the inner oxide layer [41].

Huang et al. constructed the potential-pH diagram for the $Fe-Cr-Ni-H_2O$ system at 80 °C, **Figure 2.8**. The vertical dash dot lines in **Figure 2.8** indicate the passive potential regions in different solution pHs. The calculations were based on the assumption of a stoichiometric spinel ($FeCr_2O_4$) as the corrosion product on Alloy 690 [42].

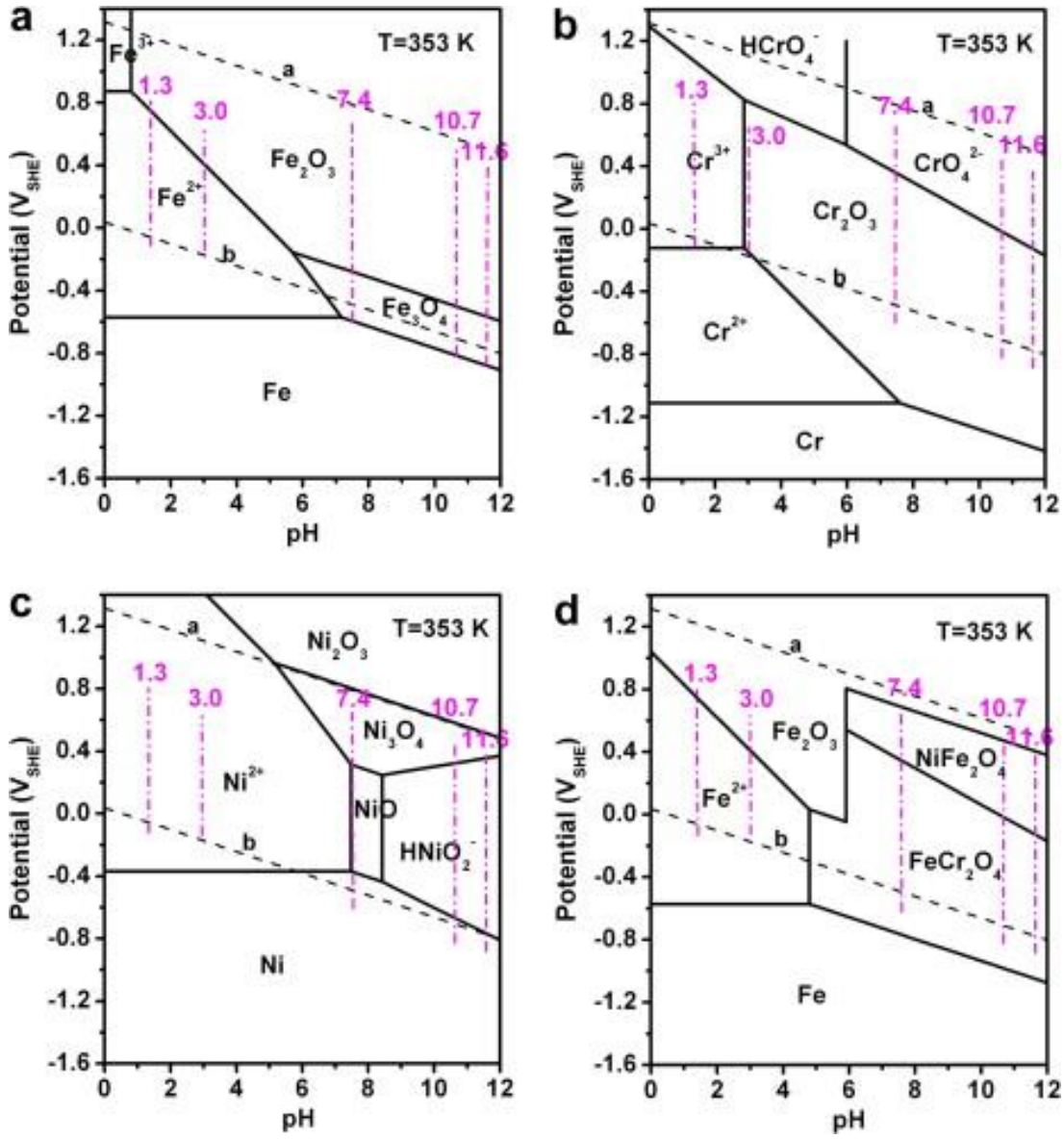

Figure 2.8 Potential–pH diagrams at 353 K. (a) $Fe-H_2O$ system, (b) $Cr-H_2O$ system, (c) $Ni-H_2O$ system, and (d) $Fe-Cr-Ni-H_2O$ system. The oxygen and hydrogen equilibria at 1 atm are represented by dash lines a and b, respectively. The vertical dash dot lines reveal the passive regions in different pH solutions[1] [42].

[1] This figure was published in Corrosion Science, Vol. 51, Issue 12, J. Huang, X. Wu, and E. Han, Influence of pH on electrochemical properties of passive films formed on Alloy 690 in high temperature aqueous environments, 2976–2982, Copyright Elsevier (2009).

2.5 Corrosion under Gamma-Radiation

The radiation energy that is absorbed by atoms and molecules will result in the formation of unstable, highly reactive ions and radicals [43]. When exposed to gamma-radiation, water decomposes, resulting in the production of a number of different redox active species, ranging from oxidizing ($\bullet OH$, H_2O_2, O_2) to reducing ($\bullet e_{aq}^-$, $\bullet H$, $\bullet O_2^-$) [43]–[46], as shown in reaction (6, [44]). In the presence of continuous gamma-radiation, these species reach low, steady-state concentrations which control the redox potential of aqueous environments and consequently the corrosion process [43].

$$H_2O \rightsquigarrow OH^1, \bullet e_{aq}^-, \bullet H, H_2, H_2O_2, H^+ \quad (6)$$

The solution environment under gamma-radiation becomes more oxidizing due to the production of H_2O_2 which acts as the main oxidant and consequently initially increases the metal oxidation rate [15], [17].

In the literature, the direct effect of gamma-radiation on the corrosion behaviours of nickel and nickel-based superalloys [17], [14], [15], Stellite-6 [47]–[49], and carbon and stainless steels has been studied [50]–[53].

The surface of nickel-based superalloys with at least 15 wt.% Cr (e.g., Inconel 600 and Alloy 800) is reported to be covered with a thin layer of Cr_2O_3 oxide due to its thermodynamic stability [14], [15].

Musa and Wren studied the effect of pH (within the range of pH 6.0 to pH 10.6) on the corrosion behaviour of Inconel 600 in deaerated solutions in the presence and absence of gamma-radiation. They concluded that a) Cr oxidation was minimal and the main oxidation reactions involved Fe and Ni and b) at a higher pH where the solubilities

[1]The reference indicated OH but I believe this to be a typo and that the correct form of this symbol should have been $\bullet OH$.

of Fe^{II} and Ni^{II} are near their minima, metal oxidation resulted in further oxide/hydroxide growth whereas a lower pH increased the dissolution of metal cations [15].

Momeni studied the effect of gamma-radiation and solution conditions and developed a predictive model for the corrosion behaviour of Alloy 800. It was concluded that a) the corrosion process involved a series of elementary reactions including metal oxidation reactions coupled with solution reduction reactions and b) the rates of metal oxidation, metal cation dissolution and oxide formation reactions evolved as corrosion progressed [14].

Karimihaghighi studied the effect of gamma-radiation and solution conditions (temperature, pH, ionic strength) on the corrosion behaviour of pure nickel and identified three phases for the overall nickel oxidation dynamics: Phase 1 involved nickel dissolution and precipitation, Phase 2 involved additional processes including the oxidation of Ni^{II} to a higher oxidation state and precipitation of a mixed Ni^{II}/Ni^{III} hydroxide and, Phase 3 involved the nucleation and growth of solid crystal particles after precipitation of sufficient mixed Ni^{II}/Ni^{III} hydroxide [17].

Ishigure et al. studied the effect of gamma-radiation (using a ^{60}Co source with a dose rate of 5×10^2 Gy h^{-1}) at temperatures up to 250 °C on the corrosion products produced from carbon steel and stainless steel (type 304). It was found that gamma-radiation increased the release rate of insoluble corrosion product (crud), but did not have much influence on the release of soluble species (ions). Moreover, they studied the effect of temperature and observed that at 65 °C, gamma-radiation had no effect on the level of crud iron. On the contrary, at 150 °C, gamma-radiation increased the level of crud iron. On the other hand, the gamma-radiation did not seem to have a large effect on the release of iron at both temperatures except for the fact that the release levels at 65 °C were lower by a factor of 10 than at 150 °C [51].

2.6 References

[1] W. F. Smith, *Structure and Properties of Engineering Alloys*, 2nd Edition. McGraw-Hill, 1993.

[2] J. R. Davis, Ed., "Nickel and Nickel Alloys," in *Metals Handbook Desk Edition*, 2nd Edition., ASM International, 1998, pp. 609–615. doi: 10.31399/asm.hb.mhde2.a0003147.

[3] W. L. Mankins and S. Lamb, "Nickel and Nickel Alloys," in ASM HANDBOOK Properties and Selection: Nonferrous Alloys and Special-Purpose Materials, vol. 2, ASM Handbook Committee, Ed. ASM International, 1990, pp. 428–445. doi: 10.31399/asm.hb.v02.a0001072.

[4] P. Breeze, *Power Generation Technologies*, 2nd Edition. Newnes, 2014.

[5] G. J. Licina, "Nuclear Power," in *Corrosion Tests and Standards: Application and Interpretation*, 2nd Edition., R. Baboian, Ed. ASTM Publication, 2005.

[6] Canadian Nuclear Association, "The Canadian Nuclear Factbook 2020" Accessed: Feb. 26, 2021. [Online]. Available: https://cna.ca/wp-content/uploads/2019/08/2020-Factbook-EN-digital.pdf

[7] The Essential CANDU, A Textbook on the CANDU Nuclear Power Plant Technology, Editor-in-Chief Wm. J. Garland, Chapter 1, "Introduction to Nuclear Reactors", by R. Chaplin, University Network of Excellence in Nuclear Engineering (UNENE), ISBN 0-9730040. Retrieved from https://www.unene.ca/education/candu-textbook on 19 Dec. 2021.

[8] Y. Wouters and L. Latu-Romain, "Corrosion in Pressurized Water," in *Encyclopedia of Interfacial Chemistry*, Elsevier, 2018, pp. 155–163. doi: 10.1016/B978-0-12-409547-2.13875-2.

[9] M. Griffiths, "The Effect of Irradiation on Ni-Containing Components in CANDU® Reactor Cores: A Review," *Nuclear Review*, pp. 1–16, May 2014, doi: 10.12943/ANR.2013.00001.

[10] H. K. Zhang, Z. Yao, G. Morin, and M. Griffiths, “TEM characterization of in-reactor neutron irradiated CANDU spacer material Inconel X-750,” *Journal of Nuclear Materials*, vol. 451, no. 1, pp. 88–96, Aug. 2014, doi: 10.1016/j.jnucmat.2014.03.043.

[11] H. K. Zhang, Z. Yao, C. Judge, and M. Griffiths, “Microstructural evolution of CANDU spacer material Inconel X-750 under in situ ion irradiation,” *Journal of Nuclear Materials*, vol. 443, no. 1, pp. 49–58, Nov. 2013, doi: 10.1016/j.jnucmat.2013.06.034.

[12] H. K. Zhang, Z. Yao, M. R. Daymond, and M. A. Kirk, “Elevated temperature irradiation damage in CANDU spacer material Inconel X-750,” *Journal of Nuclear Materials*, vol. 445, no. 1, pp. 227–234, Feb. 2014, doi: 10.1016/j.jnucmat.2013.11.008.

[13] H. K. Zhang, Z. Yao, M. A. Kirk, and M. R. Daymond, “Stability of Ni_3(Al, Ti) Gamma Prime Precipitates in a Nickel-Based Superalloy Inconel X-750 Under Heavy Ion Irradiation,” *Metallurgical and Materials Transactions A*, vol. 45, no. 8, pp. 3422–3428, Jul. 2014, doi: 10.1007/s11661-014-2309-y.

[14] M. Momeni, “Gamma-Radiation Induced Corrosion of Alloy 800,” The University of Western Ontario, 2017. Electronic Thesis and Dissertation Repository, Available: https://ir.lib.uwo.ca/etd/5011

[15] A. Y. Musa and J. C. Wren, “Combined effect of gamma-radiation and pH on corrosion of Ni–Cr–Fe alloy inconel 600,” *Corrosion Science*, vol. 109, pp. 1–12, Aug. 2016, doi: 10.1016/j.corsci.2016.03.015.

[16] D. H. Lister, R. D. Davidson, and E. McAlpine, “The mechanism and kinetics of corrosion product release from stainless steel in lithiated high temperature water,” *Corrosion Science*, vol. 27, no. 2, pp. 113–140, Jan. 1987, doi: 10.1016/0010-938X(87)90068-0.

[17] R. Karimihaghighi, “Non-Linear Effects of Solution Parameters and Gamma Radiation on Nickel Oxidation Dynamics,” The University of Western Ontario, 2021. Electronic Thesis and Dissertation Repository, Available: https://ir.lib.uwo.ca/etd/7789

[18] D. W. Shoesmith, “Kinetics of Aqueous Corrosion,” in *Corrosion: Fundamentals, Testing, and Protection*, vol. 13A, S. D. Cramer and B. S. Covino, Eds. ASM International, 2003, pp. 42–51.

[19] R. G. Kelly, J. R. Scully, D. Shoesmith, and R. G. Buchheit, *Electrochemical Techniques in Corrosion Science and Engineering*. Marcel Dekker, Inc., 2003.

[20] G. S. Frankel, “Wagner-Traud to Stern-Geary; Development of Corrosion Kinetics,” in Corrosion Science: A Retrospective and Current Status in Honor of Robert P. Frankenthal, G. S. Frankel, H. S. Isaacs, J. R. Scully, and J. D. Sinclair, Eds. The Electrochemical Society Inc., Proceedings Volume 2002-13, 2002, pp. 33–41.

[21] L. R. Faulkner, “Understanding electrochemistry: Some distinctive concepts,” *Journal of Chemical Education*, vol. 60, no. 4, pp. 262–264, Apr. 1983, doi: 10.1021/ed060p262.

[22] M. Naghizadeh, “Copper Corrosion Dynamics under Deep Geologic Repository Conditions,” The University of Western Ontario. Accessed: Aug. 12, 2021. Electronic Thesis and Dissertation Repository, Available: https://ir.lib.uwo.ca/etd/7894/

[23] J. C. Scully, *The fundamentals of corrosion*, 3rd Edition. Pergamon press, 1990.

[24] K. S. Schmitz, *Physical Chemistry*. Elsevier, 2017. doi: 10.1016/C2013-0-18556-X.

[25] I. S. Hwang, R. G. Ballinger, J. W. Prybylowski, and K. Hosoya, “Electrochemistry of Multiphase Nickel-Base Alloys in Aqueous Systems,” *Journal of The Electrochemical Society*, vol. 136, no. 7, pp. 1874–1883, Jul. 1989, doi: 10.1149/1.2097067.

[26] Z. Ahmad, *Principles of Corrosion Engineering and Corrosion Control*, 1st Edition. Elsevier Ltd., 2006.

[27] L. D. Burke and M. E. G. Lyons, “Electrochemistry of Hydrous Oxide Films,” in *Modern Aspects of Electrochemistry*, vol. 18, R. E. White, J. O’M. Bockris, and B. E. Conway, Eds. Springer US, 1986, pp. 169–248.

[28] J. R. Scully and K. Lutton, “Polarization Behavior of Active Passive Metals and Alloys,” in *Encyclopedia of Interfacial Chemistry*, K. Wandelt, Ed. Elsevier, 2018, pp. 439–447.

[29] H. Tamura, “The role of rusts in corrosion and corrosion protection of iron and steel,” *Corrosion Science*, vol. 50, no. 7, pp. 1872–1883, Jul. 2008, doi: 10.1016/j.corsci.2008.03.008.

[30] R. M. Cornell and U. Schwertmann, *The Iron Oxides: Structure, Properties, Reactions, Occurrences and Uses*, 2nd Edition. Wiley-VCH, 2003.

[31] I. David and A. J. E. Welch, “The oxidation of magnetite and related spinels. Constitution of gamma ferric oxide,” *Transactions of the Faraday Society*, vol. 52, pp. 1642–1650, 1956.

[32] C. Sunseri, S. Piazza, and F. D. Quarto, “Photocurrent Spectroscopic Investigations of Passive Films on Chromium,” *Journal of The Electrochemical Society*, vol. 137, no. 8, p. 2411, Aug. 1990, doi: 10.1149/1.2086952.

[33] M. Metikoš-Huković and M. Ceraj-Cerić, “p-Type and n-Type Behavior of Chromium Oxide as a Function of the Applied Potential,” *Journal of The Electrochemical Society*, vol. 134, no. 9, p. 2193, Sep. 1987, doi: 10.1149/1.2100850.

[34] B. M. Sass and D. Rai, “Solubility of amorphous chromium(III)-iron(III) hydroxide solid solutions,” *Inorganic Chemistry*, vol. 26, no. 14, pp. 2228–2232, Jul. 1987, doi: 10.1021/ic00261a013.

[35] C. O. A. Olsson, “Passivation of Stainless Steels and Other Chromium Bearing Alloys,” in *Encyclopedia of Interfacial Chemistry*, Elsevier, 2018, pp. 357–364. doi: 10.1016/B978-0-12-409547-2.13585-1.

[36] S. R. Mellsop, A. Gardiner, B. Johannessen, and A. T. Marshall, “Structure and transformation of oxy-hydroxide films on Ni anodes below and above the oxygen evolution potential in alkaline electrolytes,” *Electrochimica Acta*, vol. 168, pp. 356–364, Jun. 2015, doi: 10.1016/j.electacta.2015.04.020.

[37] H. Bode, K. Dehmelt, and J. Witte, “Zur kenntnis der nickelhydroxidelektrode—I.Über das nickel (II)-hydroxidhydrat,” *Electrochimica Acta*, vol. 11, no. 8, pp. 1079–1087, Aug. 1966, doi: 10.1016/0013-4686(66)80045-2.

[38] S. Tuzi, K. Göransson, S. M. H. Rahman, S. G. Eriksson, F. Liu, M. Thuvander, and K. Stiller, “Oxide evolution on Alloy X-750 in simulated BWR environment,” *Journal of Nuclear Materials*, vol. 482, pp. 19–27, Dec. 2016, doi: 10.1016/j.jnucmat.2016.09.026.

[39] S. Tuzi, H. Lai, K. Göransson, M. Thuvander, and K. Stiller, “Corrosion of pre-oxidized nickel alloy X-750 in simulated BWR environment,” *Journal of Nuclear Materials*, vol. 486, pp. 350–360, Apr. 2017, doi: 10.1016/j.jnucmat.2017.01.051.

[40] Y. Qiu, T. Shoji, and Z. Lu, “Effect of dissolved hydrogen on the electrochemical behaviour of Alloy 600 in simulated PWR primary water at 290 °C,” *Corrosion Science*, vol. 53, no. 5, pp. 1983–1989, May 2011, doi: 10.1016/j.corsci.2011.02.020.

[41] X. Ru, Z. Lu, J. Chen, G. Han, J. Zhang, P. Hu, and X. Liang, “Effects of iron content in Ni-Cr-xFe alloys and immersion time on the oxide films formed in a simulated PWR water environment,” *Journal of Nuclear Materials*, vol. 497, pp. 37–53, Dec. 2017, doi: 10.1016/j.jnucmat.2017.10.048.

[42] J. Huang, X. Wu, and E. Han, “Influence of pH on electrochemical properties of passive films formed on Alloy 690 in high temperature aqueous environments,” *Corrosion Science*, vol. 51, no. 12, pp. 2976–2982, 2009.

[43] J. C. Wren, “Steady-State Radiolysis: Effects of Dissolved Additives,” in *Nuclear Energy and the Environment*, vol. 1046, American Chemical Society, 2010, pp. 271–295.

[44] J. M. Joseph, B. Seon Choi, P. Yakabuskie, and J. Clara Wren, “A combined experimental and model analysis on the effect of pH and O_2(aq) on γ-radiolytically produced H_2 and H_2O_2,” *Radiation Physics and Chemistry*, vol. 77, no. 9, pp. 1009–1020, Sep. 2008, doi: 10.1016/j.radphyschem.2008.06.001.

[45] J. W. T. Spinks, *An Introduction to Radiation Chemistry*, 2nd Edition. John Wiley & Sons, Inc., 1976.

[46] G. S. Was, “Environmentally Assisted Cracking of Irradiated Metals and Alloys,” in *Fundamentals of Radiation Materials Science*, Berlin, Heidelberg: Springer Berlin Heidelberg, 2007, pp. 765–814. doi: 10.1007/978-3-540-49472-0_15.

[47] M. Behazin, J. J. Noël, and J. C. Wren, “Combined Effects of pH and γ-Irradiation on the Corrosion of Co-Cr Alloy Stellite-6,” *Electrochimica Acta*, vol. 134, pp. 399–410, Jul. 2014, doi: 10.1016/j.electacta.2014.04.079.

[48] M. Behazin, M. C. Biesinger, J. J. Noël, and J. C. Wren, “Comparative study of film formation on high-purity Co and Stellite-6: Probing the roles of a chromium oxide layer and gamma-radiation,” *Corrosion Science*, vol. 63, pp. 40–50, Oct. 2012, doi: 10.1016/j.corsci.2012.05.007.

[49] M. Behazin, “Radiation Induced Corrosion of Stellite-6,” The University of Western Ontario, 2014. Electronic Thesis and Dissertation Repository, Available: https://ir.lib.uwo.ca/etd/2434

[50] D. Guo, “Corrosion Dynamics of Carbon Steel in Used Fuel Container Environments,” The University of Western Ontario, 2018. Electronic Thesis and Dissertation Repository, Available: https://ir.lib.uwo.ca/etd/5897

[51] K. Ishigure, N. Fujita, T. Tamura, and K. Oshima, “Effect of Gamma Radiation on the Release of Corrosion Products from Carbon Steel and Stainless Steel in High Temperature Water,” *Nuclear Technology*, vol. 50, no. 2, pp. 169–177, Sep. 1980, doi: 10.13182/NT80-A32543.

[52] Q. W. Knapp and J. C. Wren, “Film formation on type-316L stainless steel as a function of potential: Probing the role of gamma-radiation,” *Electrochimica Acta*, vol. 80, pp. 90–99, Oct. 2012, doi: 10.1016/j.electacta.2012.06.090.

[53] K. Daub, X. Zhang, J. J. Noël, and J. C. Wren, “Gamma-radiation-induced corrosion of carbon steel in neutral and mildly basic water at 150 °C,” *Corrosion Science*, vol. 53, no. 1, pp. 11–16, Jan. 2011, doi: 10.1016/j.corsci.2010.09.048.

CHAPTER 3

Experimental Techniques and Procedures

3.1 Introduction

In this Chapter, the experimental procedures used for conducting electrochemical and coupon exposure tests are explained. The fundamental principles of the techniques used in this thesis are also explained. The procedures used for sample (Inconel X-750) and solution preparation are also discussed, to eliminate the need for further explanations in each data Chapter (Chapters 4, 5 and 6).

3.2 Specimen and Solution Preparation

The chemical composition of Inconel X-750 (UNS NO7750, ThyssenKrupp VDM USA, INC.) used in this work is shown in **Table 3.1**. The solution used in this study was 0.01 M sodium borate solution, prepared using 18.2 MΩ cm high-purity water and $Na_2B_4O_7.10H_2O$. The high-purity water used was prepared using a NANOpure Diamond UV ultra-pure water system (Barnstead International). The solution pH was adjusted to 10.6 by adding 2 M $NaOH$ solution (made from $NaOH$ pellets) to the 0.01 M borate solution, while pH 6.0 and pH 8.4 were achieved by addition of an appropriate amount of H_3BO_3. The accuracy of pH measurements was within ± 0.3 of the desired pH. The pH of the prepared solutions was measured by a Fisher Scientific accumet® BASIC AB15 pH meter.

Table 3.1 Chemical composition of Inconel X-750 (UNS NO7550).

Element	Ni	Cr	Fe	Ti	Nb	Al
Percent (wt%)	71.64	15.55	8.20	2.52	0.89	0.70

3.3 Electrochemical Experiments

For electrochemistry experiments, the working electrode (WE) was prepared in the form of a cylindrical disc with a diameter of 1 cm and a thickness of 0.5 cm. A threaded hole was created on one flat face to allow it to be attached to the electrode holder. The other side of the electrode was manually grounded using silicon carbide papers followed by a mirror polishing on a polishing cloth. The polished WE was cleaned in a sonication bath using a 50/50 acetone/methanol mixture to remove the polishing residues. Next, the WE was dried in a flow of argon gas and attached to the electrode holder. Then, the whole assembly was wrapped with Parafilm (for experiments conducted at 25 °C) or Teflon (for experiments conducted at 80 °C) on all sides except the circular flat, mirror-polished side, allowing it to be in contact with the electrolyte.

A large solution volume (nearly 500 mL) was used in the electrochemistry experiments. Either a saturated calomel electrode (SCE, Fisher Scientific) at 25 °C or a silver-silver chloride ($Ag/AgCl$, Fisher Scientific) at 80 °C was used as the reference electrode (RE) in the absence of gamma-radiation. A mercury/mercury oxide Hg/HgO reference electrode (Radiometer Analytical) was used in the presence of gamma-radiation due to its superior stability under radiation relative to SCE and $Ag/AgCl$ reference electrodes [1], [2]. Silver-silver chloride electrodes have the advantage that they can be used at temperatures greater than 60 °C, whereas calomel electrodes cannot [3]. A platinum mesh (Alfa Aesar, 99.9% purity) was used as the counter electrode (CE). The exposed surface area of the coupon was 0.785 cm^2 in all electrochemistry experiments. For electrochemistry experiments run under continuous argon purging and under gamma-radiation, the solution was purged with a flow of argon gas (Praxair, 99.9%) for about 1 hour prior to start of the experiment. For electrochemistry experiments under gamma-

radiation, the solution was no longer being purged after the cell was transferred to the gamma cell chamber.

Electrochemistry experiments were performed in non-polarized (corrosion potential or E_{corr} measurement) and polarized (cyclic voltammetry (CV) and potentiodynamic (PD) polarization) modes. The electrochemistry experiments were carried out in a three-electrode cell using a Solartron MultiStat (1480), a Biologic multichannel potentiostat (VMP-300) or a Biologic potentiostat (MCS-200). All electrochemistry experiments were preceded by five minutes' cathodic cleaning (e.g., at –1.1 V_{SCE} in pH 10.6, at –0.97 V_{SCE} in pH 8.4 and at –0.83 V_{SCE} in pH 6.0 solutions at 25 °C). Cathodic cleaning is carried out to remove any remaining organic residue to ensure a reproducible starting surface [4].

In voltammetry, a variable potential is applied to a WE in an electrochemical cell. This excitation signal produces a current response. In classical voltammetry, the applied voltage changes linearly with time and the current response is recorded as a function of time, and as a function of the applied voltage. In CV, the potential is cycled between two values, first increasing linearly to a maximum and then decreasing linearly with the same slope to the original value. This process may be repeated numerous times while the current is recorded as a function of time [3]. In this study, only the first cycles of the CV experiments are presented. In CV, the potential range was extended from the cleaning potential to a more positive (more noble) potential, referred to as positive potential scan. Then, the potential was scanned to the initial cleaning potential in the more negative (less noble) direction, referred to as negative potential scan. Each PD polarization experiment was carried out after 24 hours of E_{corr} measurement. In PD polarization, the potential was scanned from 300 mV below (less positive) to 300 mV above (more positive) the value of E_{corr} at 24 hours. The scan rate was set to 5 mV s^{-1} for both CV and PD polarization experiments.

3.4 Coupon Exposure Experiment

For coupon exposure tests performed in argon-saturated and under gamma-radiation conditions, the stock solution of interest was purged with argon gas prior to being transferred to the glove box. The coupons used were of two different thicknesses: 3 mm and 5 mm. The coupon exposure tests were performed at 25 °C, 80 °C and 150 °C, and the coupons were completely submerged in the solution of interest. The amount of solution used in each coupon exposure test was 6.0 mL. The quartz vials containing the immersed coupons were sealed by crimp caps to prevent solution evaporation and any ingress/egress of gas during the test [5]. For coupon exposure experiments at 150 °C, the prepared quartz vials were inserted into an autoclave. The autoclave was partially filled with water to balance the pressure between the inner and outer sides of the vial at 150 °C [6]. A leak test was carried out with argon gas for about 20 minutes before inserting the autoclave into the gamma cell chamber.

Upon termination of the experiment, the amounts of dissolved Cr, Fe, and Ni ions were measured using an inductively coupled plasma optical emission spectrometry (ICP-OES) instrument (Perkin Elmer Avio 200). The solutions from the coupon exposure tests were diluted using nitric acid to ensure that the dissolved metals remained dissolved (not forming colloidal particles) in the test solution prior to analysis using ICP-OES [7]. The dissolution of Cr, Fe, and Ni was then determined as a function of time. The dilution factor was taken into consideration and the results were normalized to the exposed surface area since coupons of different thicknesses were used. The morphology of the corroded coupons was analyzed using a field emission scanning electron microscopy (SEM, LEO 1540XB). The corroded coupons were stored in a vacuum desiccator prior to the SEM analysis.

3.5 Radiation Source

An MDS Nordion Gammacell 220 Excel Cobalt-60 irradiator was used as the source of radiation. The radiation dose rate during the experiments was ~ 2.1 – 1.7 kGy

h^{-1}, where 1 Gy is equivalent to 1 J of energy absorbed per kilogram [4]. All experiments in the presence of radiation were performed by placing the electrochemical cell or autoclave containing the coupon vials inside the gamma cell sample chamber, which was then lowered into the irradiation zone, a cylindrical cavity surrounded by 11 tubular pencils containing ^{60}Co [4]. The ^{60}Co radiation source has a half-life of 5.27 years and emits two photons per disintegration with energies of 1.17 MeV and 1.33 MeV [8], [9].

3.6 Potentiostat

The corrosion kinetics of the WE can be studied by changing the potential of the WE (with respect to the RE) and measuring the reaction rate in terms of current density. In an electrochemical cell, the RE allows the separation of applied potential into a controlled (between the RE and the WE) and a controlling (between the RE and CE) portion. The potentiostat changes the potential of the controlling portion to keep the potential of the controlled portion at the desired value [10]. When the current is supplied (by the potentiostat) to the CE, electrical current must be concurrently withdrawn from WE (and vice versa) in order to maintain the electronic equipment and the electrode electrically neutral [11].

3.7 Scanning Electron Microscopy (SEM)

A scanning electron microscope has four major sections: 1) electron source (or electron gun), 2) electromagnetic lenses, which are used to focus the electron beam and demagnify it into a small electron probe, 3) deflection system and 4) the detectors, which are used to collect signals emitted from the sample [12].

In SEM a focused beam of electrons is directed on to the specimen, and the signals emitted from the specimen are collected as a function of the position of the incident focused electron beam [12]. The electrons are accelerated to an energy between 1 and 30 keV. The magnetic condenser and objective lens systems reduce the spot size to a diameter of 2 – 10 nm when it reaches the sample [3].

An incident electron beam that impinges on a sample surface can undergo both elastic and inelastic scattering events as it penetrates the solid sample. Inelastic scattering refers to any process in which the primary electron loses a detectable amount of energy, whereas in elastic scattering the electron energy remains unchanged [12].

Several types of signals are produced from a surface, including backscattered electrons (BSEs) and secondary electrons (SEs) [3]. The region electrons penetrate is known as the interaction volume [3]. Electrons that leave the surface with energies >50 eV are termed BSEs while all the electrons with energies between 1 eV and ~50 eV are termed SEs [12].

Two pairs of scanning coils deflect the electron beam to scan over a raster. Scanning the entire rastered area is accomplished by moving the beam to the next line and repeating this process [12]. SEs are often detected by Everheart-Thornley detector. Photons are emitted when the SEs strike a scintillator—a phosphor that emits light when struck by energetic particles such as electrons. The emitted photons are carried by a light guide to a photomultiplier tube where they are converted into pulses of electrons [3]. These pulses of electrons are then used to control the brightness of the electron beam in a cathode ray tube (CRT) on which, SEM images are displayed [3], [13]. On the other hand, semiconductor detectors are widely used for BSEs, but they suffer from a relatively slower response time compared to scintillators [3].

3.8 Inductively Coupled Plasma Optical Emission Spectrometry (ICP-OES)

An ICP-OES instrument consists of an electrolyte-introduction system (nebulizer and spray chamber), a plasma chamber containing a torch and argon gas supplies, a radio-frequency generator and the associated electronics, and a spectrometer with detectors for emitted photons [14].

Routine determination of 70 elements can be made using ICP-OES at concentration levels below one milligram per liter [15]. In ICP-OES, a liquid sample is injected into the instrument, which is then nebulized into an aerosol, a very fine mist of droplets. The aerosol is transported to the plasma where it is desolvated, vaporized, atomized, and excited and/or ionized. The excited atoms and ions emit photons with wavelengths characteristic of the specific elements. These photons are collected and sorted by wavelength. The photons are detected and turned into electronic signals that are converted into concentration information for the analyst [15].

3.9 References

[1] M. Behazin, "Radiation Induced Corrosion of Stellite-6," The University of Western Ontario, 2014. Electronic Thesis and Dissertation Repository, Available: https://ir.lib.uwo.ca/etd/2434

[2] M. Behazin, M. C. Biesinger, J. J. Noël, and J. C. Wren, "Comparative study of film formation on high-purity Co and Stellite-6: Probing the roles of a chromium oxide layer and gamma-radiation," *Corrosion Science*, vol. 63, pp. 40–50, Oct. 2012, doi: 10.1016/j.corsci.2012.05.007.

[3] D. A. Skoog, F. J. Holler, and S. R. Crouch, Principles of Instrumental Analysis, 6th Edition. Thomson Brooks/Cole, 2007.

[4] Q. W. Knapp and J. C. Wren, "Film formation on type-316L stainless steel as a function of potential: Probing the role of gamma-radiation," *Electrochimica Acta*, vol. 80, pp. 90–99, Oct. 2012, doi: 10.1016/j.electacta.2012.06.090.

[5] R. Karimihaghighi, "Non-Linear Effects of Solution Parameters and Gamma Radiation on Nickel Oxidation Dynamics," The University of Western Ontario, 2021. Electronic Thesis and Dissertation Repository, Available: https://ir.lib.uwo.ca/etd/7789

[6] A. Y. Musa and J. C. Wren, "Combined effect of gamma-radiation and pH on corrosion of Ni–Cr–Fe alloy inconel 600," *Corrosion Science*, vol. 109, pp. 1–12, Aug. 2016, doi: 10.1016/j.corsci.2016.03.015.

[7] K. I. Choudhry, D. A. Guzonas, D. T. Kallikragas, and I. M. Svishchev, “On-line monitoring of oxide formation and dissolution on alloy 800H in supercritical water,” *Corrosion Science*, vol. 111, pp. 574–582, Oct. 2016, doi: 10.1016/j.corsci.2016.05.042.

[8] J. W. T. Spinks, *An Introduction to Radiation Chemistry*, 2nd Edition. John Wiley & Sons, Inc., 1976.

[9] K. Jan, K. Bashir, S. Jan, and Ab. L. Khan, “Principles and Sources of Gamma Irradiation,” in *Innovative Food Processing Technologies*, Elsevier, 2021, pp. 61–70. doi: 10.1016/B978-0-08-100596-5.23010-2.

[10] R. G. Kelly, J. R. Scully, D. Shoesmith, and R. G. Buchheit, *Electrochemical Techniques in Corrosion Science and Engineering*. Marcel Dekker, Inc., 2003.

[11] W. S. Tait, “Chapter 5 - Electrochemical Corrosion Basics,” in *Handbook of Environmental Degradation of Materials*, 3rd Edition., M. Kutz, Ed. William Andrew Publishing, 2018, pp. 97–115. doi: 10.1016/B978-0-323-52472-8.00005-8.

[12] C. Scheu and W. D. Kaplan, “Introduction to Scanning Electron Microscopy,” in *In-Situ Electron Microscopy: Applications in Physics, Chemistry and Materials Science*, Wiley-VCH Verlag GmbH & Co. KGaA, 2012, pp. 1–37.

[13] B.L. Gabriel, “Scanning Electron Microscopy,” in *Fractography*, ASM International, 1987, pp. 166–178. doi: 10.31399/asm.hb.v12.a0001835.

[14] O. Gharbi, O. Hirsch, P. Chapon, and A. Stankova, “Inductively Coupled Plasma Optical Emission Spectroscopy,” in *ASM HANDBOOK Materials Characterization*, vol. 10, ASM International, 2019, pp. 71–83.

[15] C. B. Boss and K. J. Fredeen, *Concepts, instrumentation, and techniques in inductively coupled plasma optical emission spectrometry*, 3rd Edition. Perkin Elmer, 2004.

CHAPTER 4

The Effects of Solution pH, Temperature, and Redox and Transport Conditions on the Corrosion Evolution of Inconel X-750

4.1 Introduction

Corrosion involves the transfer of metal valence electrons to electrochemically active ions and molecules (i.e., oxidant) in the oxidizing medium to which the corroding metal is exposed. The corrosion process requires the reduction of oxidant to maintain the electrical charge neutrality of the metal and the electrolyte. The oxidation and reduction reactions happen simultaneously at the interface of the metal and the electrolyte. The oxidized metal atoms leave the metal lattice and become solvated (or hydrated in aqueous solutions) in the electrolyte. Once in the electrolyte, the solvated/hydrated metal cation can undergo chemical reactions. The overall rate of metal corrosion depends on one or a combination of the electrochemical and chemical reactions that are involved in the corrosion process [1]–[6].

The elementary reactions involved in corrosion of some pure metals (i.e., Ni and Cu) are discussed in the literature [4], [5]. In this thesis, these elementary reactions are adapted (from [4], [5]) for metal M (e.g., pure Fe) and are summarized in **Table 4.1**. These elementary reactions which are interfacial charge transfer and solution transport reactions will be discussed for metallic atoms $M^0_{(m)|int}$, dissolved metal cations ($M^{n+}_{(aq)}$), and precipitated metal oxides/hydroxides ($M(OH)_{n\,(s)}$). These elementary reactions and the corrosion fundamentals (discussed above and) in Chapter 2 will be used to discuss the corrosion processes in this thesis.

Table 4.1 Schematic of elementary reactions involved in the overall oxidation of pure Fe (adapted from [4], [5]).

Rxn	Reaction	(Electro)chemical Equation	Rate
M1	Electron transfer	$Fe^{0}_{(m)\|int} \rightleftharpoons Fe^{2+}_{(aq)\|int} + 2e^{-}$ Metal oxidation consists of two reaction steps: $\upsilon_{M1} = \upsilon_{M1f} - \upsilon_{M1r}$	$\upsilon_{M1} = \upsilon_{M1f} - \upsilon_{M1r}$
Trans	Ion diffusion	$Fe^{2+}_{(aq)\|int} \rightsquigarrow Fe^{2+}_{(aq)\|bulk}$	υ_{Trans}
Ox – Red	Electron transfer	$2H^{+} + 2e^{-} \rightleftharpoons H_2$ (see **Appendix B** and **Appendix C**)	$\upsilon_{Ox} = \upsilon_{Ox,f} - \upsilon_{Ox,r}$
M2	Electron transfer	$\left\{Fe^{2+}_{(aq)\|int} \rightleftharpoons Fe(OH)_2\right\} \rightleftharpoons \left\{Fe^{3+}_{(aq)\|int} \rightleftharpoons Fe(OH)_3\right\} + e^{-}$	υ_{M2}
Hyd	Hydrolysis	$Fe^{2+} + 2OH^{-} \rightleftharpoons Fe(OH)_2$ $Fe^{3+} + 3OH^{-} \rightleftharpoons Fe(OH)_3$	υ_{Hyd}
Gel	Hydrogel formation	$Fe(OH)_2/Fe(OH)_3 \rightsquigarrow Fe^{II}_x Fe^{III}_y (OH)_{2z\,(gel)}$	υ_{Gel}
Oxide	Crystal formation	$Fe^{II}_x Fe^{III}_y (OH)_{2z\,(gel)} \rightsquigarrow Fe^{II}_x Fe^{III}_y (O)_{z\,(crystal)} + zH_2O$	υ_{Oxide}

Metal oxidation (M1):

Corrosion involves metal oxidation half-reaction (reaction 1) coupled to oxidant (or solution) reduction half-reaction on the metal surface [6]. This is an electrochemical process in which electron transfer occurs at the metal/solution interface. The rate of this interfacial electron transfer largely depends on the redox potential of the solution [6]. In naturally corroding conditions, the redox potential of the solution is determined by the type(s) and concentration(s) of the oxidant(s). For example, in the presence of continuous gamma-radiation exposure, the redox potential of the solution is determined by the concentrations of the water radiolysis products which reach steady-state values [6]–[8].

$$M^{0}_{(m)|int} \rightleftharpoons M^{n+}_{(m)|int} + ne^{-} \quad (1)$$

where $M^{0}_{(m)|int}$, $M^{n+}_{(m)|int}$ are the metal atom and the oxidized metal cation in metallic site, respectively. Metal cation transfer from metal to solution requires lattice-bond breaking followed by solvation (or hydration) of the cation (reaction 2) [7], [6].

$$M^{n+}_{(m)|int} + nH_2O \rightarrow M^{n+}_{(hyd)} \rightarrow M^{n+}_{(aq)|int} \quad (2)$$

where $M^{n+}_{(hyd)}$ and $M^{n+}_{(aq)|int}$ are the hydrated metal cation and the dissolved metal cation in the interfacial region, respectively.

The redox potential of the solution is highest under continuous gamma-radiation exposure and lowest in solutions under continuous argon purging in which the solubility of dissolved oxygen is lower than that in a stagnant air-saturated solution (among the three solution conditions studied in this Chapter). In a more oxidizing solution such as a solution under continuous gamma-radiation exposure where highly oxidizing (e.g., H_2O_2) species are generated, the rate of interfacial electron transfer can increase [6], [4], [9].

Metal cation transport (Trans):

Unlike for electrochemical reactions on inert electrodes, the corrosion of metals and alloys involves the transfer of oxidized metal atoms ($M^{n+}_{(m)|int}$) from the metal to the solution [6]. The transport of a dissolved metal cation from the interfacial region ($M^{n+}_{(aq)|int}$) to the bulk solution ($M^{n+}_{(aq)|bulk}$), reaction 3, is driven by the concentration gradient (between the interfacial region and bulk solution) for that metal cation [4]. In large solution volumes and where the solution moves convectively, as in a three-electrode setup with solution under continuous argon purging, the interfacial region/bulk solution interface remains dilute (with regard to dissolved metal cations). This results in fast diffusion of metal cations from the interfacial region to the bulk solution compared to in stagnant solutions (such as solutions in stagnant air-saturated conditions) [4]. However, the rate of metal cation transport is significantly slower than the rate of electron transfer which occurs on a timescale of ~10^{-15} s [10].

$$M^{n+}_{(aq)|int} \rightsquigarrow M^{n+}_{(aq)|bulk} \quad (3)$$

The solution volume affects the rate of reaction 3 [4], [6]; further discussion is provided in Chapter 6, which discusses coupon exposure tests in small solution volumes. The net dissolution of dissolved metal cations (e.g., Ni^{II}) is initially higher at pH 6.0 than at pH 10.6 [11]. The rate of reaction 3 depends on the solution pH and the redox conditions. In a lower solution pH where the solubility limit of a metal cation is higher, a larger concentration gradient (between the interfacial region and bulk solution) establishes, which increases the rate of reaction 3 (see 'Hydrogel (Gel) formation' section below for further discussion on solubility limit). In more oxidizing conditions, the concentration of dissolved metal cations ($M^{n+}_{(aq)|int}$) increases faster and therefore the rate of reaction 3 increases.

Oxidant reduction ($Ox - Red$):

In naturally corroding conditions, oxidant (or solution, e.g., H^+) reduction reaction (reaction 4), must occur on the same electrode where metal oxidation occurs, to fulfill electrical charge neutrality requirements [6], [3]:

$$2H^+ + 2e^- \rightleftharpoons H_2 \quad (4)$$

Hydrolysis (Hyd):

The hydrated metal cation $M^{n+}_{(aq)}$ undergoes hydrolysis (reaction 5, [7]):

$$M^{n+}_{(aq)} + xOH^- \rightleftharpoons M(OH)^{(n-x)+}_{x\,(aq)} \quad (5)$$

where x is 1, 2, ... n+1 [7] and $M(OH)^{(n-x)+}_{x\,(aq)}$ is a hydrolyzed metal cation. The redox potential of the solution (which is defined by the type and concentration of oxidant present in solution) does not directly affect the solvation of a metal cation [6]. However, increasing the temperature from room temperature to 80 °C increases the rate of metal cation (e.g., $Fe^{2+}_{(aq)}$) hydrolysis [11]. Solution pH affects the hydrolysis equilibria of transition metal cations (reaction 5) [7]. For the range of pH studied in this thesis, the rate of hydrolysis increases with pH and therefore a higher rate of hydrolysis is expected at pH 10.6 than at pH 6.0.

Hydrogel (Gel) formation:

The hydrolysis of metal cations takes place in both the interfacial ($M^{n+}_{(aq)|int}$) and bulk ($M^{n+}_{(aq)|bulk}$) solutions. Metal oxide/hydroxide precipitation becomes significant when the concentration of a dissolved metal cation reaches its solubility limit defined by the solubility-pH diagram [12]. In the interfacial region, the solubility limit of a dissolved metal cation is referred to as $M^{n+}_{(aq)|int\,(sat)}$. In other words, the formation of *dissolved* metal hydroxide ($M(OH)_{n\,(aq)}$) happens even below the solubility limit, but the

formation of *solid* metal hydroxide ($M(OH)_{n\,(s)}$) becomes significant only when all the hydrolysis reactions reach equilibrium (reaction 6):

$$M^{n+}_{(aq)} \rightleftharpoons M(OH)_{n\,(s)} \tag{6}$$

Under these conditions, further hydrolysis of a dissolved metal cation results in the precipitation of $M(OH)_{n\,(s)}$.

The precipitated metal hydroxide ($M(OH)_{n\,(s)}$) is in dynamic equilibrium with the dissolved metal cation $M^{n+}_{(aq)}$, meaning that oxide/hydroxide dissolution and precipitation occur at the same rate. In the case of a multi-element precipitated metal hydroxide, a dynamic equilibrium exists between the hydroxide and dissolved metal cations of its constituents. In addition, the solubility limit of a given metal cation in the pure state is not necessarily the same as that in the presence of a multi-element hydrogel network that forms on the surface of an alloy such as Inconel X-750.

Solid metal hydroxides of transition metals precipitate as colloidal particles which results in the formation of a hydrogel network [4], [5], [13], (reaction 7). Under these conditions, the transport of dissolved metal cations from the corroding substrate to the bulk solution is slower than for a corroding surface without precipitated solid metal hydroxides [1], [5].

$$M^{n+}_{(aq)}/M(OH)_{n\,(s)} \rightsquigarrow M(OH)_{n\,(gel)} \tag{7}$$

The precipitated metal hydroxide undergoes chemical and electrochemical reactions. The metal hydroxide, $M(OH)_{n\,(s)}$, and the hydrogel network, $M(OH)_{n\,(gel)}$, are in chemical equilibrium with the dissolved metal cation, $M^{n+}_{(aq)}$. In a highly oxidizing environment, dissolved metal ions can further oxidize to a higher oxidation state. The possibility of $M^{n+}_{(aq)}$ oxidation to a dissolved metal cation of a higher oxidation state, $M^{(n+1)+}_{(aq)}$ increases in the presence of a hydrogel network, as the activation energy for a solution reaction is typically higher than that of surface reactions [4], [6]. Therefore, in

the presence of a hydrogel network, the oxidation of $M_{(aq)}^{n+}$ to $M_{(aq)}^{(n+1)+}$occurs faster (reaction 8). Similar to the first oxidation step, the oxidized metal cation undergoes hydrolysis and produces metal oxide/hydroxide of a higher oxidation state, $M(OH)_{(n+1)\,(s)}$, via the following electrochemical reaction:

$$\left\{M_{(aq)|int}^{n+} \rightleftharpoons M(OH)_n\right\} \rightleftharpoons \left\{M_{(aq)|int}^{(n+1)+} \rightleftharpoons M(OH)_{n+1}\right\} + e^- \quad (8)$$

Further oxidation of the dissolved metal cation (reaction 8) results in the development (evolution) of the hydrogel network. That is to say, the hydrogel network contains more than one oxidation state of a given metal ion (e.g., Fe^{II}/Fe^{III}).

Crystal formation (Oxide):

The growth of a metal oxide into a distinct crystal phase from dissolved ions, such as the growth of magnetite particles during corrosion, is very sensitive to temperature because lattice bond formation is a high activation energy process [6].

Some alloys such as Inconel X-750 contain more than one metallic element—in this case, three main elements: Ni, Cr, and Fe. Each element can have its own oxidation pathways. In addition, the formation of mixed metal oxides such as iron chromite or nickel chromite can occur early, adding extra pathways that the system can take. However, the fundamentals explained above regarding the steps involved in the corrosion of a pure metal (e.g., Fe) can still be applied to alloys which may contain more than one type of metal atom.

As explained above, the corrosion process consists of multiple steps. These steps are not independent of each other. That is to say, one step can affect or be affected by other steps. This is because the solution in contact with the corroding metal is an open chemical system in which the dissolved species (including the hydrated metal cations and reduced oxidant products) can move from the interfacial region to the bulk solution. In other words, there exists a systemic feedback in the corrosion process in which one

elementary reaction can affect or be affected by one or more other elementary reaction(s) [4], [5]. Under such conditions, the overall rate of the reaction is defined by the slowest step. This step is referred to as the rate-determining step (RDS). The combined effects of redox condition, pH, and temperature determine the RDS and therefore the process(es) that control the overall rate of metal oxidation.

4.2 Experimental Procedures

This Chapter studies the effect of solution pH (10.6, 8.4 and 6.0), temperature (25 °C and 80 °C), and solution redox and transport conditions (i.e., solution under continuous argon purging, stagnant air-saturated solution, and solution under gamma-radiation) on E_{corr} evolution. The E_{corr} measurements were conducted for 24 hours. The details of the experimental procedures and materials used can be found in Chapter 3.

4.3 Results and Discussions

Metal oxidation (which is coupled with oxidant reduction reaction) occurs when it is thermodynamically possible meaning that the metal is thermodynamically unstable in the oxidizing solution. The electrochemical driving force for corrosion is the difference between the equilibrium potentials of the metal oxidation half-reaction ($E^e_{M/M^{n+}}$) and the redox potential of the oxidizing medium ($E^e_{Ox/Red}$) [1], [3].

Corrosion of a pure metal involves not only the oxidation of a metal from a metallic site, $M^0_{(m)|int}$, but also the movement of dissolved metal cations. That is to say, the metal oxidation half-reaction is entropy-driven [4], [5]. Therefore, the true $E^e_{M/M^{n+}}$ for the metal oxidation half-reaction cannot be determined. Oxidant reduction, on the other hand, is accompanied by movement of oxidant to the metal surface and the movement of oxidant reduction products (e.g., H_2) from the interfacial region to the bulk solution [5]. Therefore, the reaction between the oxidant and the solution reduction products is likewise entropy driven. The diffusion of H_2 from the electrode surface to the bulk solution disturbs the equilibrium potential of the oxidant reduction reaction. Since

the equilibrium state is defined for reversible reactions only, there is no true equilibrium between the oxidant (e.g., H^+) and the reduced oxidant (e.g., H_2). Therefore, no true $E^e_{Ox/Red}$ can be defined for the redox potential of the oxidizing medium.

The corrosion potential, E_{corr}, that is adopted by the system is dictated by the relative kinetics of the oxidation and reduction reactions. No quantitative information (i.e., the rate of oxidation or reduction reactions) can be extracted from the E_{corr}. This is because at every moment, the rate of the oxidation reactions is equal to the rate of the reduction reactions. However, the value and the rate of change of E_{corr} can provide qualitative information on the evolution of the corrosion kinetics with time [1].

In **Figure 4.1**, the E_{corr} measurement results are presented for each pH (10.6, 8.4 and 6.0) in solution under continuous argon purging, stagnant air-saturated solution and solution under gamma-radiation. The designations 'Ar', 'air' and 'rad' refer to solution under continuous argon purging, stagnant air-saturated solution and solution under gamma-radiation. The potential in **Figure 4.1** is presented versus the reversible hydrogen electrode (RHE) for each pH. To this end, the electrode potentials measured relative to the saturated calomel electrode (SCE) or the $Ag/AgCl$ reference electrode were shifted by pH × 0.059 + 0.241 mV in the more positive (more noble) direction when SCE was used—and by pH × 0.059 + 0.197 mV in the more positive (more noble) direction when $Ag/AgCl$ was used (see **Appendix B** for more details).

In **Figure 4.1**, the equilibrium potentials (E^{eq}_{rxn}) values of redox half-reactions involving solid species only are presented next to the E_{corr} diagram; the full list of calculated E^{eq}_{rxn} values for redox half-reactions is provided in **Appendix B**. The E^{eq}_{rxn} values for redox half-reactions at 80 °C are shown by dotted lines. In addition, the E^{eq}_{rxn} values for redox half-reactions containing dissolved metal cations are not presented because such an equilibrium potential depends on the concentration of dissolved metal cations. This is because the concentrations of dissolved metal cations in the interfacial region change as corrosion progresses [11]. Therefore, the E^{eq}_{rxn} values for dissolved

metal cations cannot be determined if the concentration of dissolved metal cations in the interfacial region is unknown.

The overpotential for a redox half-reaction is defined as ($\left|\eta_{rxn}\right| = \left|E_{elec} - E_{rxn}^{eq}\right|$) [4], where E_{elec} is the electrode potential. Under naturally corroding conditions, the electrode potential is E_{corr} and therefore, the overpotential for a redox half-rection is: $\left|\eta_{rxn}\right| = \left|E_{corr} - E_{rxn}^{eq}\right|$. Comparing the E_{corr} and E_{rxn}^{eq} values of various possible redox half-reactions can determine whether or not a redox half-reaction can occur [11].

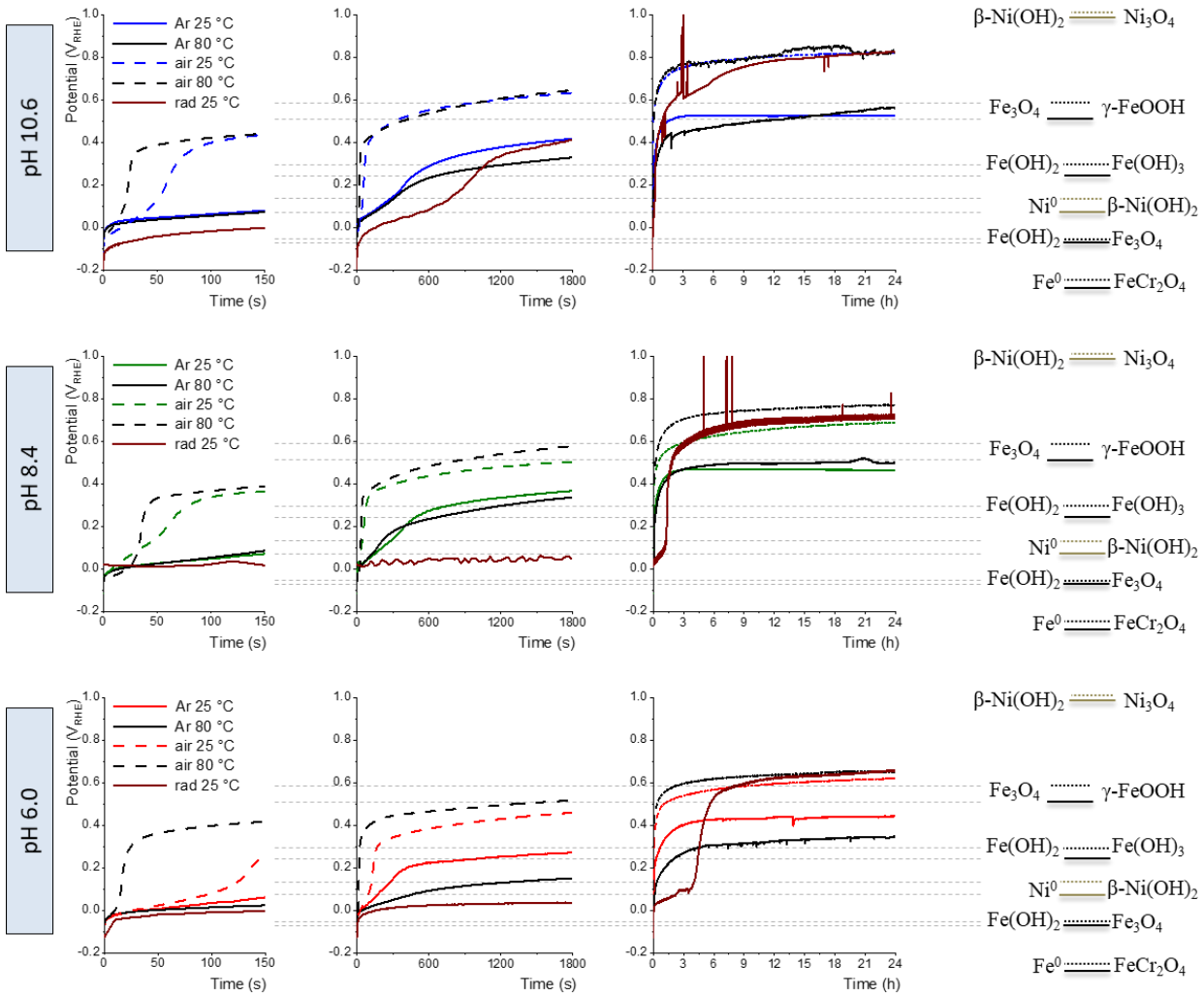

Figure 4.1 E_{corr} measurements in solution under continuous argon purging, stagnant air-saturated solution, and solution under gamma-radiation, at pH 10.6 (top), pH 8.4 (middle) and pH 6.0 (bottom).

Figure 4.1 shows that under all conditions, the E_{corr} changed in a quasi-stepwise manner. In all conditions, the E_{corr} contained an initial and a final period over which it changed slowly. The term 'steady-state' indicates the slow changes in E_{corr} over time. In other words, the redox reactions occurring on the corroding metal are in quasi-equilibrium (i.e., steady-state) [4]. In this Chapter, the initial and final stages are referred to as 1st and 2nd (pseudo-) steady-states, respectively. The 1st (pseudo-) steady-state is more evident in 0 – 150 s timeframe and in solutions under continuous argon purging. The E_{corr} reached the 1st (pseudo-) steady-state value typically within less than a second. Interestingly, the E_{corr} did not remain in the1st (pseudo-) steady-state. Rather, it evolved to the 2nd (pseudo-) steady-state. Irrespective of the solution pH, temperature and redox and transport conditions:

- Under given redox conditions (solution under continuous argon purging or stagnant air-saturated solution), the average values of the 1st and the 2nd (pseudo-) steady-states were independent of solution temperature—except at pH 6.0 in solution under continuous argon purging or at pH 8.4 in stagnant air-saturated solution where the difference between the average values of the 2nd (pseudo-) steady-states was slightly larger, about 100 mV.
- The average value of the 1st (pseudo-) steady-state was nearly independent of dissolved oxygen concentration whereas the average value of the 2nd (pseudo-) steady-state was a function of dissolved oxygen concentration.
- The average value of E_{corr} in the 1st (pseudo-) steady-state was close to the E_{rxn}^{eq} of a Fe species and below the E_{rxn}^{eq} of a Ni species.
- The 2nd (pseudo-) steady-state was farther from the E_{rxn}^{eq} of metal and metal hydroxide species and closer to the E_{rxn}^{eq} of metal oxide/hydroxide redox reactions or between the E_{rxn}^{eq} of two such redox reactions.
- At 25 °C: a) at all studied pHs, the 1st (pseudo-) steady-state was longest under gamma-radiation and shortest in the stagnant air-saturated solution, b) the 2nd (pseudo-) steady-states in stagnant air-saturated solution and solution under gamma-radiation approached the same final E_{corr} value (which is more obvious at pH 10.6) whereas the 2nd (pseudo-) steady-state

in solution under continuous argon purging approached a different final E_{corr} value and c) the 2nd (pseudo-) steady-state in stagnant air-saturated and under gamma-radiation conditions showed a slow increase in electrode potential over time, unlike the 2nd (pseudo-) steady-state in solution under continuous argon purging which showed no change over time.

- At both temperatures, the 2nd (pseudo-) steady-state value was in the vicinity of $E^{eq}_{Fe_3O_4 \rightleftharpoons \gamma-FeOOH}$ but less noble than $E^{eq}_{\beta-Ni(OH)_2 \rightleftharpoons Ni_3O_4}$ in solution under continuous argon purging. On the other hand, in stagnant air-saturated solution, the 2nd (pseudo-) steady-state value was always more noble than $E^{eq}_{Fe_3O_4 \rightleftharpoons \gamma-FeOOH}$ but less noble than $E^{eq}_{\beta-Ni(OH)_2 \rightleftharpoons Ni_3O_4}$.

The same E_{corr} results in **Figure 4.1** for solutions under continuous argon purging and stagnant air-saturated solutions are represented in **Figure 4.2** to better observe the effects of solution pH and dissolved oxygen concentration (at two temperatures) on E_{corr} evolution. **Figure 4.2** showed that:

- The duration of the 1st (pseudo-) steady-state was nearly the same for all three pHs in the stagnant air-saturated solution—more evident at 80 °C for all pHs and slightly different for pH 6.0 at 25 °C compared to the other two pHs.
- The duration of the 1st (pseudo-) steady-state was nearly the same for all three pHs in the solution under continuous argon purging—more evident at 25 °C for all pHs and slightly different for pH 6.0 at 80 °C compared to the other two pHs.
- The solution pH had almost no effect on the average value of the 1st (pseudo-) steady-state. However, the average value of the 2nd (pseudo-) steady-state was a function of solution pH.
- Irrespective of solution temperature or dissolved oxygen concentration, a decrease in solution pH decreased the average value of the 2nd (pseudo-) steady-state to a less positive (less noble) potential.

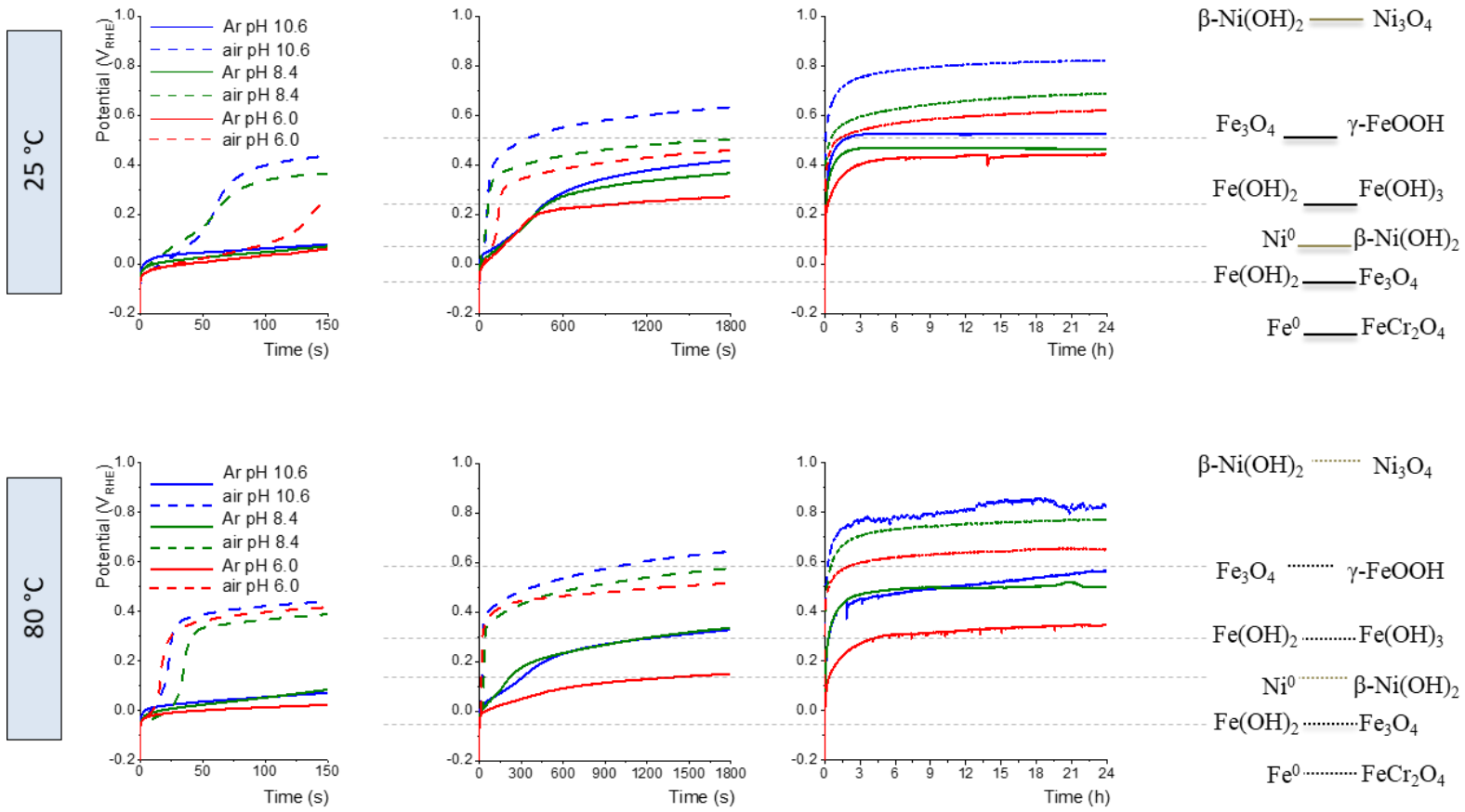

Figure 4.2 The effects of pH and dissolved oxygen concentration on E_{corr} evolution at 25 °C (top) and 80 °C (bottom).

The rate of a chemical reaction depends on the chemical activities (~ concentrations) of reactants. When a chemical process is reversible (i.e., the products of the forward reaction can react in the reverse direction), the net rate of the process is the difference between the forward and reverse rates. The electrochemical oxidation half-reaction of a metal to a metal cation at the metal-solution interface is a reversible process. That is, the net rate of metal oxidation depends not only the chemical activity of metal ($a_{M^0_{(m)|int}} = 1.0$) but also that of the metal cation ($a_{M^{n+}_{(aq)|int}} \approx \left[M^{n+}_{(aq)|int}\right]$):

$$\upsilon_{M1} = \upsilon_{M1f} - \upsilon_{M1r} = k_{M1f} \cdot (a_{M^0_{(m)|int}}) - k_{M1r} \cdot (a_{M^{n+}_{(aq)|int}}) \quad \text{[Eq 1]}$$

$$\upsilon_{M1} = k_{M1f} - k_{M1r} \cdot (a_{M^{n+}_{(aq)|int}}) \quad \text{[Eq 2]}$$

where k_{M1f} and k_{M1r} are the (pseudo-) 1st order rate coefficient for the forward and reverse reactions of $M1$, respectively [4]. [Eq 1] and [Eq 2] are adapted for metal M from [4]. As corrosion occurs, $a_{M^0_{(m)|int}}$ does not change (remains at 1.0) but $a_{M^{n+}_{(aq)|int}}$ does [4], [11]. Therefore, the net rate of metal oxidation ($\upsilon_{M1} = k_{M1f} - k_{M1r} \cdot (a_{M^{n+}_{(aq)|int}})$) changes with time, as υ_{M1} depends on $a_{M^{n+}_{(aq)|int}}$. The rate of $M1f$ is independent of $a_{M^{n+}_{(aq)|int}}$, while the rate $M1r$ depends on $a_{M^{n+}_{(aq)|int}}$. Therefore, as corrosion progresses, the build-up of metal cations in the interfacial region increases $a_{M^{n+}_{(aq)|int}}$. As a result, the rate of $M1r$ increases while the rate of $M1f$ remains unchanged.

The proximity of E_{corr} to either $E^e_{M/M^{n+}}$ or $E^e_{Ox/Red}$ can indicate which one of the two half-reactions may be rate-determining [1]. The overpotential for a redox half-rection is defined as ($\left|\eta_{rxn}\right| = \left|E_{corr} - E^{eq}_{rxn}\right|$). For a metal oxidation half-reaction, ($\left|\eta_{ox}\right| = \left|E_{corr} - E^{eq}_{ox}\right|$) where E^{eq}_{ox} is the equilibrium potential of metal oxidation half-reaction. The proximity of E_{corr} in the 1st (pseudo-) steady-state to the E^{eq}_{rxn} of metal and metal hydroxide species is indicative of the low overpotential required for metal oxidation (i.e., η_{ox}). At t = 0, the interfacial region (and bulk solution) is free of dissolved metal cations (e.g., $Fe^{2+}_{(aq)|int}$) and the metal oxidation half-reaction (υ_{M1}) can occur very easily. This

explains the proximity of E_{corr} in the 1st (pseudo-) steady-state to the E_{rxn}^{eq} of metal and metal hydroxide species for all solution pHs, temperatures and redox conditions.

It is evident from **Figure 4.2** that at all pHs and temperatures, changing the solution conditions from continuous argon purging to stagnant air-saturated decreased the duration of the 1st (pseudo-) steady-state. The solution convection resulting from continuous argon purging affects the saturation of the interfacial region with dissolved metal cations. As mentioned above, in solution under continuous argon purging the concentration of dissolved metal cations in the interfacial region/bulk solution interface remains low. This increases the rate of metal cation transport from the interfacial region to the bulk solution and the time required to saturate the interfacial region with dissolved metal cations.

In more oxidizing conditions, the overpotential for the metal oxidation half-reaction, ($|\eta_{ox}| = |E_{corr} - E_{ox}^{eq}|$), is larger. This results in faster oxidation of $M_{(m)|int}^{0}$ to $M_{(aq)|int}^{n+}$ which can saturate the interfacial region faster. The redox potential of the solution under gamma-radiation is more positive (more noble) than that of the stagnant air-saturated solution. This is due to the production of H_2O_2 which acts as the main oxidant and therefore initially increases the metal oxidation rate [4], [7]. Interestingly, however, the duration of the 1st (pseudo-) steady-state at 25 °C was longer under gamma-radiation than in stagnant air-saturated solution. In addition, the increase in the duration of the 1st (pseudo-) steady-state under gamma-radiation was pH-dependent. That is, the duration of the1st (pseudo-) steady-state was most affected at a lower pH. This behaviour can be attributed to the change in solution pH under gamma-radiation, which affects the solubility limit of dissolved metal cations and therefore how fast the interfacial region becomes saturated with dissolved metal cations. Under gamma-radiation, the solution pH decreases and the interfacial solution becomes more acidic. This is due to the continuous generation of H^+, which is a water radiolysis product [9], [4]. The solubility limit of metal cations (e.g., Fe^{II} and Ni^{II}) depends on solution pH [12]. At a lower pH (within the range of pH studied in this study), the solubility limits of Fe^{II} and Ni^{II} are higher [12]. However, these solubility limits are calculated for pure $Fe(OH)_2$ and $Ni(OH)_2$

hydroxides, which do not necessarily represent the solubility limit of Fe^{II} or Ni^{II} for the multi-element hydrogel network that forms on the surface of Inconel X-750. Nonetheless, the decrease in solution pH increases the dissolutions of both Fe^{II} or Ni^{II} (with a higher impact on Ni^{II} than Fe^{II}), see further discussions in Chapter 6. This is consistent with the extended 1st (pseudo-) steady-state at each pH under gamma-radiation. It should also be noted that although the average value of E_{corr} in the 1st (pseudo-) steady-state was below (less positive than) the E^{eq}_{rxn} of Ni species (i.e., $E^{eq}_{Ni^0 \rightleftharpoons \beta-Ni(OH)_2}$), the oxidation of Ni to dissolved $Ni^{2+}_{(aq)}$ has its own (quasi-) equilibrium potential at each moment (with a less positive value). More specifically, the oxidation of Ni occurs at a potential below (less positive than) the E^{eq}_{rxn} of Ni species (i.e., $E^{eq}_{Ni^0 \rightleftharpoons \beta-Ni(OH)_2}$).

It was observed that the E_{corr} did not remain in the 1st (pseudo-) steady-state. Rather, the E_{corr} moved from the 1st to the 2nd (pseudo-) steady-state. Once the interfacial region reaches the solubility limit of a metal cation ($M^{n+}_{(aq)|int\ (sat)}$), the yield of the hydrolysis reaction becomes significant and metal oxide/hydroxide precipitation ($M(OH)_{n\ (s)}$) becomes pronounced. Solid metal hydroxides of transition metals ($M(OH)_{n\ (s)}$) form colloidal particles and then a hydrogel network [4], [5], [13]. The deposition of corrosion products on the surface which results in the formation and growth of the hydrogel network inhibits the transport of dissolved metal cations from the corroding substrate [1], [5]. The effect of the hydrogel network on inhibiting the transport of dissolved metal cation away from the corroding surface becomes considerable as the hydrogel network grows.

Figure 4.1 showed that E_{corr} quickly becomes more noble than the $E^{eq}_{H^+ \rightleftharpoons H_2}$(which is 0.000 V_{RHE} under the standard conditions). The fact that in early times, the presented E_{corr} in this Chapter quickly becomes more positive (more noble) than the actual $E^{eq}_{H^+ \rightleftharpoons H_2}$does not violate the thermodynamic constraints. The E_{corr} at all times lies at a potential that is more positive (more noble) than E^{eq}_{Ox} and less positive (less noble) than E^{eq}_{Red}—in the simple case of one metal oxidation and one oxidant reduction half-reaction. In the absence of dissolved oxygen, the only oxidant in early times in the

solution is H^+. However, the 1 atm pressure of dissolved H_2 (standard conditions) is not a reasonable assumption in non-standard conditions. The atmospheric pressure of H_2 is 6 $\times 10^{-7}$ atm [5], [14]. The pressure of dissolved H_2 is calculated in **Appendix C** using Henry's constant of 1282.04 atm M^{-1} for H_2 [15]. This increases the $E^{eq}_{H^+ \rightleftharpoons H_2}$ reduction reaction by 273 mV in the more positive (more noble) direction—see **Appendix C** for more details. In conclusion, the average value of E_{corr} in the 1st (pseudo-) steady-state is not more positive (more noble) than the actual $E^{eq}_{H^+ \rightleftharpoons H_2}$.

Once the hydrogel network forms, the dissolved metal cation (e.g., $Fe^{2+}_{(aq)|int}$) can oxidize to a higher oxidation state ($Fe^{3+}_{(aq)|int}$) (via reaction 8). This reaction requires a much stronger oxidant than water (or H^+) [6]. The solubility of dissolved oxygen in the solution under continuous argon purging is not zero. This value is reported to be 75 ppb in deaerated water [16]. Therefore, the formation of a metal cation of a higher oxidation state ($Fe^{3+}_{(aq)|int}$) can also occur in the solution under continuous argon purging. Once the interfacial region becomes saturated with $Fe^{3+}_{(aq)|int}$ species, these species precipitate as $Fe(OH)_{3\,(s)}$. A metal cation of a higher oxidation state ($Fe^{3+}_{(aq)|int}$) can act as an oxidant. In the presence of $Fe^{3+}_{(aq)|int}$, the rate of the H^+ reduction reaction decreases and $Fe^{3+}_{(aq)|int}$ acts as the main oxidant [17]. This explains the shift of E_{corr} from the 1st to the 2nd (pseudo-) steady-state.

The E_{corr} in the 2nd (pseudo-) steady-state in the solution under continuous argon purging approached $E^{eq}_{Fe_3O_4 \rightleftharpoons \gamma-FeOOH}$ for all three pHs and both temperatures—while the E_{corr} in the 2nd (pseudo-) steady-state at a higher pH was closer to $E^{eq}_{Fe_3O_4 \rightleftharpoons \gamma-FeOOH}$. On the other hand, in the stagnant air-saturated solution, the E_{corr} in the 2nd (pseudo-) steady-state situated at a potential more positive (more noble) than $E^{eq}_{Fe_3O_4 \rightleftharpoons \gamma-FeOOH}$ but less positive (less noble) than $E^{eq}_{\beta-Ni(OH)_2 \rightleftharpoons Ni_3O_4}$ at all three pHs and both temperatures. In addition, for both sets of redox conditions (i.e., solution under continuous argon purging and stagnant air-saturated solution), the 2nd (pseudo-) steady-state was farther from

$E^{eq}_{O_2 \rightleftharpoons OH^-}$ and closer to $E^{eq}_{Fe_3O_4 \rightleftharpoons \gamma-FeOOH}$ or $E^{eq}_{\beta-Ni(OH)_2 \rightleftharpoons Ni_3O_4}$ (depending on the dissolved oxygen concentration). This behaviour was independent of solution temperature or pH.

In the solution under continuous argon purging, although the concentration of dissolved oxygen is not zero, it is significantly lower than that in stagnant air-saturated solution. The oxidation of dissolved Fe^{II} to dissolved Fe^{III} in the solution requires a much stronger oxidant than water (or H^+) [6]. Likewise, the oxidation of dissolved Ni^{II} to dissolved Ni^{III} in the solution is slower in solution under continuous argon purging than in stagnant air-saturated solution. In addition, the oxidation of Ni requires a larger overpotential than for Fe. Therefore, in the absence of a strong oxidant (e.g., O_2), the formation of Fe^{III} is more likely than Ni^{III}, (reactions 9 and 10, respectively):

$$\{Fe^{2+}_{(aq)|int} \rightleftharpoons Fe(OH)_2\} \rightleftharpoons \{Fe^{3+}_{(aq)|int} \rightleftharpoons Fe(OH)_3\} + \ e^- \tag{9}$$

$$\{Ni^{2+}_{(aq)|int} \rightleftharpoons Ni(OH)_2\} \rightleftharpoons \{Ni^{3+}_{(aq)|int} \rightleftharpoons Ni(OH)_3\} + \ e^- \tag{10}$$

Once the interfacial region becomes saturated with Fe^{III}, $Fe(OH)_3$ precipitates as the hydrolysis equilibrium shifts to the right (reaction 6). As a result, the hydrogel network in the solution under continuous argon purging is likely a mixture of Fe^{II}/Fe^{III} and Ni^{II} hydroxides. However, oxidation of dissolved Ni^{II} to a higher oxidation state (reaction 10) can be significant in more oxidizing solutions such as those in the presence of gamma-radiation or in stagnant air-saturated solution. Once the interfacial region becomes saturated with Ni^{III}, $Ni(OH)_3$ precipitates, as the hydrolysis equilibrium shifts to the right (reaction 6). As a result, in more oxidizing conditions, it is more likely that the hydrogel network composition changes to include corrosion products of higher oxidation states (i.e., Ni^{III}) and becomes a mixture of Fe^{II}/Fe^{III} and Ni^{II}/Ni^{III}. Both $Fe^{3+}_{(aq)|int}$ and $Ni^{3+}_{(aq)|int}$ can act as oxidants and can reduce back to $Fe^{2+}_{(aq)|int}$ and $Ni^{2+}_{(aq)|int}$ (as long as the E_{corr} in 2nd (pseudo-) steady-state is less positive (less noble) than $E^{eq}_{Fe_3O_4 \rightleftharpoons \gamma-FeOOH}$ or $E^{eq}_{\beta-Ni(OH)_2 \rightleftharpoons Ni_3O_4}$, respectively). It should be noted that these equilibrium potentials are for stoichiometric species. The hydrogel network (or the oxide

film) that forms on Inconel X-750 is not necessarily a mixture of stoichiometric metal oxides/hydroxides. Non-stoichiometric species have their own equilibrium potentials. This explains the evolution and average value of E_{corr} in the 2nd (pseudo-) steady-state and proves that it is not the initial oxidant that predominantly controls the E_{corr} evolution. Rather, it is the dissolved corrosion products (e.g., $Fe^{3+}_{(aq)|int}$ and $Ni^{3+}_{(aq)|int}$) that determine the E_{corr} evolution.

Studying the E_{corr} evolution in this Chapter showed that corrosion of Inconel X-750 occurs in three stages (adapted from [4]; see Chapter 2 for three phases of pure nickel oxidation dynamics).

In stage 1, shown in **Figure 4.3**, the interfacial region remains below the saturation limit of the dissolved metal cations (i.e., $M^{n+}_{(aq)|int}$). In a less oxidizing solution, lower pHs where the solubility limits of dissolved metal cations are higher, or when there is convective solution flow (such as that in the solution under continuous argon purging), the saturation of the interfacial region requires more time. During stage 1, the hydrolysis of dissolved metal cations occurs, but the low yield of the hydrolysis reaction does not result in the precipitation of solid metal hydroxide, $M(OH)_{n\,(s)}$; any formation of solid metal hydroxide is local and negligible. This is because the interfacial region is not saturated with the dissolved metal cations. During stage 1, the dissolved metal cations (i.e., $M^{n+}_{(aq)|int}$) and hydrolysis products transport from the interfacial region to the bulk solution. This transport occurs as a result of the concentration gradient that is established between the interfacial region and the bulk solution [4]. When the solution volume is large and under continuous convective flow, the transport of dissolved metal cations is fast due to the continuous removal of these species from the interfacial region/bulk solution interface. In stage 1, the overall rate of metal oxidation is controlled by the rate of the metal oxidation reaction: $\upsilon_{M1} = \upsilon_{M1f} - \upsilon_{M1r}$.

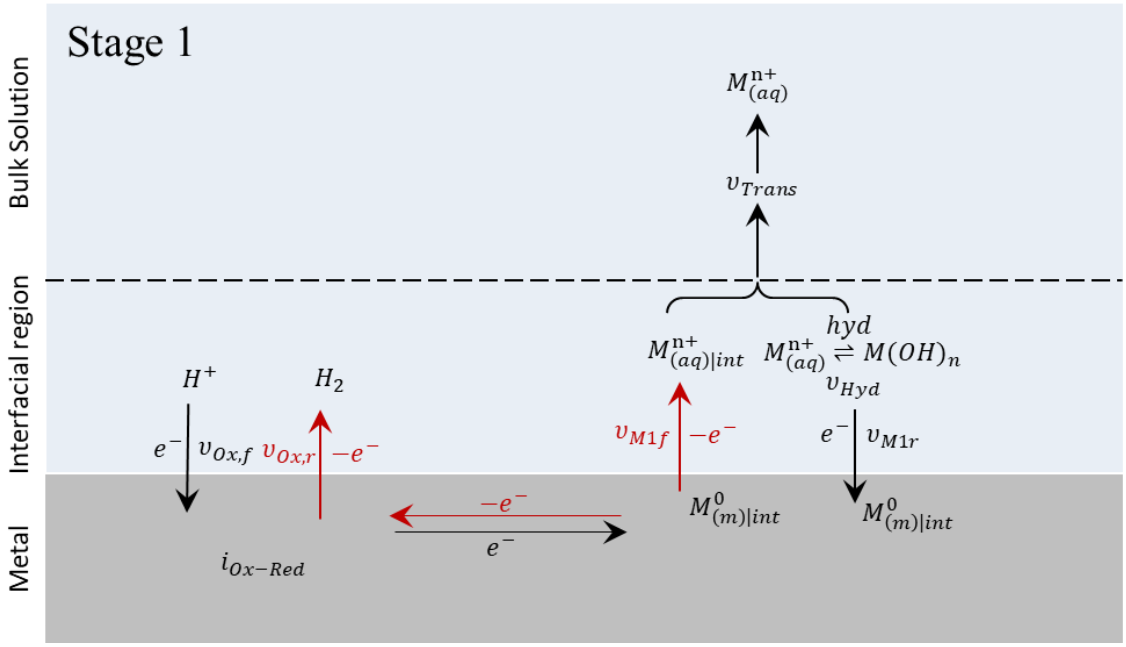

Figure 4.3 Schematic of elementary steps involved in the corrosion of a pure metal in the presence of one oxidant in stage 1 (adapted for metal M from [4], [5]).

In stage 2, shown in **Figure 4.4**, the reactions from stage 1 are still occurring. However, the interfacial region becomes saturated with dissolved metal cations (i.e., $M^{n+}_{(aq)|int}$), which shift the hydrolysis equilibrium towards the precipitation of corrosion products (e.g., $M^{n+}_{(aq)|int\,(sat)} \rightleftharpoons M(OH)_{n\,(s)}$). The build-up of solid corrosion products results in the formation of a hydrogel network. In the presence of a hydrogel network, the transport of hydrated metal cations from the metal/solution interface to the bulk solution is very slow. Therefore, further metal oxidation results in the precipitation of solid corrosion products and hence the growth of precipitated corrosion products (i.e., the hydrogel network) [11]. The thicker and more laterally expanded hydrogel network further affects the transport of dissolved metal cations (from the metal/solution interface to the bulk solution).

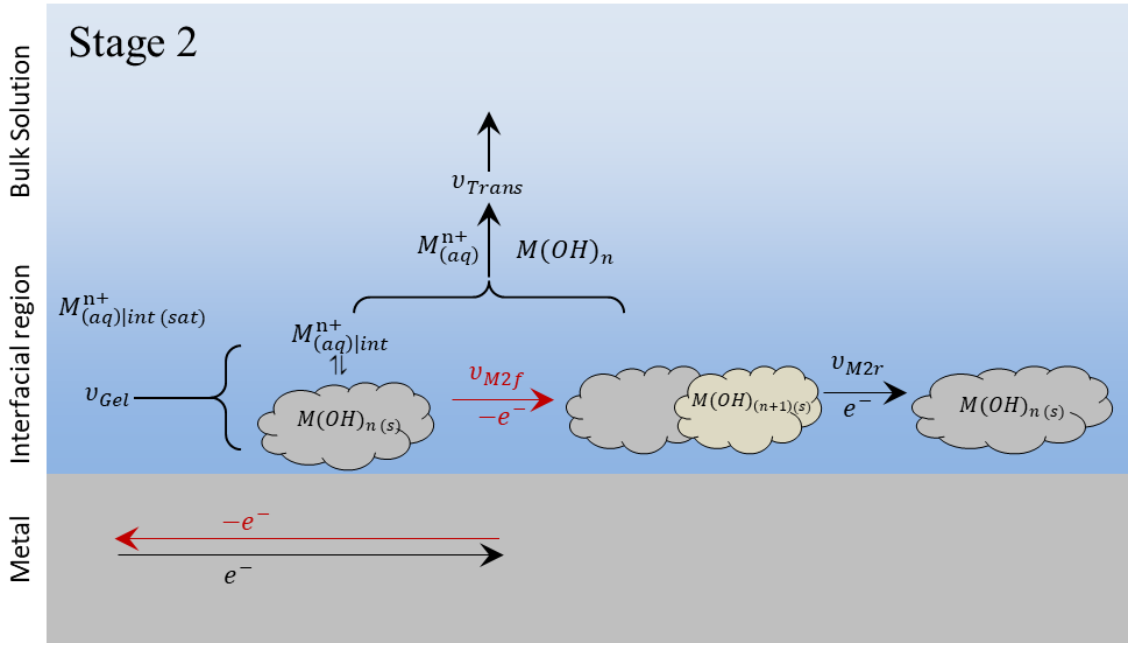

Figure 4.4 Schematic of elementary steps involved in the corrosion of a pure metal in stage 2 (adapted for metal M from [4], [5]).

In the presence of a stronger oxidant than water (or H^+), the precipitated corrosion product can oxidize further (i.e., $M(OH)_{n\ (s)} \rightarrow M(OH)_{(n+1)\ (s)}$). The likelihood of such an oxidation reaction depends on the concentration of the stronger oxidant and the metal element. If the concentration of the stronger oxidant is not significant and the oxidation potential of the metal is more positive (more noble), e.g., Ni, the oxidation of its corrosion product (e.g., $Ni(OH)_{2\ (s)}$) to a higher state is unlikely—compared to a metal with a less positive (less noble) oxidation potential (e.g., Fe). However, in more oxidizing solutions, such a reaction becomes likely and the hydrogel network can further develop. More specifically, the hydrogel network becomes a mixture of different oxidation states of the constituent metal cations (e.g., Fe^{II}/Fe^{III} and Ni^{II}/Ni^{III}). These metal cations of a higher oxidation state can act as strong oxidants. This result in the evolution of E_{corr} to more positive (more noble) potentials.

In stage 3, shown in **Figure 4.5**, the interfacial region is covered with a hydrogel network which is in a dynamic equilibrium with its constituent metal cations. The

hydrogel network, which is a mixture of solid metal hydroxides and electrolyte, can dehydrate and convert into solid crystal oxides. The formation of solid crystal oxides is faster at higher temperatures since lattice bond formation is a high-activation-energy process [6]. The formation of solid crystal oxides inhibits the hydration of oxidized metal cations ($M^{n+}_{(m)|int}$) and suppresses further metal oxidation (since, as mentioned above, metal cation transfer from metal to solution requires lattice-bond breaking followed by solvation (or hydration) of the cation (reaction 2) [7], [6]). Stage 3 is discussed further in Chapter 5.

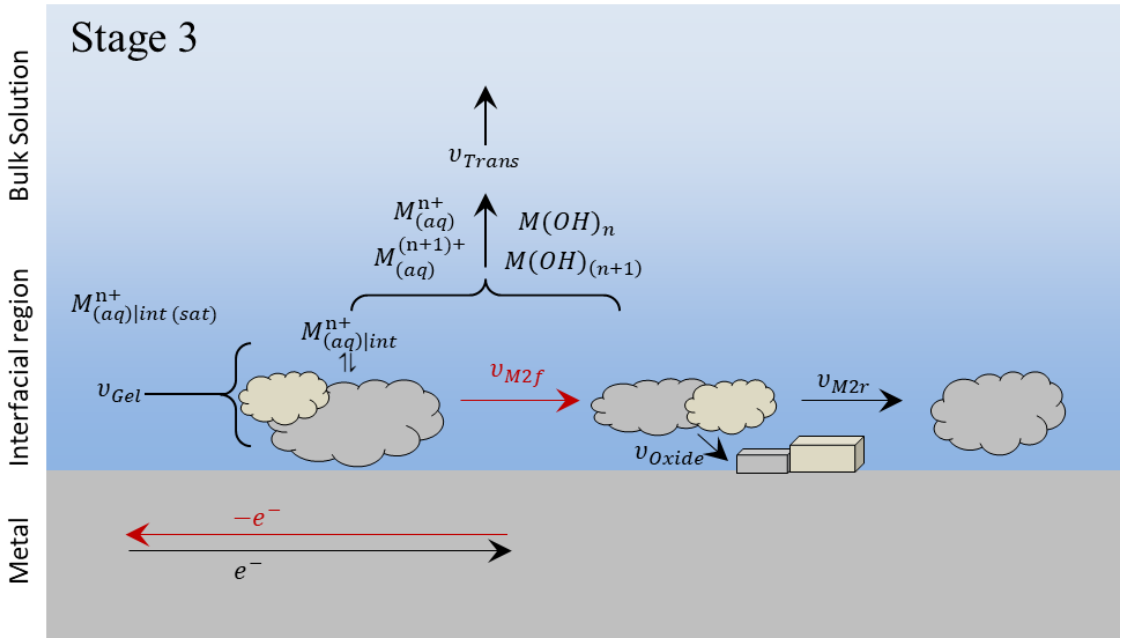

Figure 4.5 Schematic of elementary steps involved in the corrosion of a pure metal in stage 3 (adapted for metal M from [4], [5]).

4.4 Conclusions

This Chapter studied the effect of solution redox and transport conditions (i.e., solution under continuous argon purging, stagnant air-saturated solution, and solution under gamma-radiation) on E_{corr} evolution. It was concluded that E_{corr} started with a 1st (pseudo-) steady-state but did not remain in this steady-state. Rather, the E_{corr} moved

toward a 2nd (pseudo-) steady-state, which was farther from the E_{rxn}^{eq} values of metal/metal oxides/hydroxides solid species and closer to the E_{rxn}^{eq} of metal oxides/hydroxides solid species or between the E_{rxn}^{eq} of two redox reactions of metal oxides/hydroxides solid species. The shift from the 1st to the 2nd (pseudo-) steady-state was attributed to the formation of corrosion products in the form of a hydrogel network which facilitated the formation of metal cations of higher oxidation states. Once a hydrogel network had developed, the metal cations of higher oxidation states acted as the main oxidant and, and therefore controlled the redox conditions of the interfacial region and the overall corrosion process. It was concluded that at 25 °C, the corrosion of Inconel X-750 was mainly driven by metal oxidation products accumulated in later stages not by the water radiolysis products. The results from this Chapter indicated that the corrosion of Inconel X-750 evolves through mainly three stages:

In stage 1, the interfacial region remains below the metal cation saturation limit. Due to the concentration gradient that exists at the metal/solution and interfacial region/bulk solution interfaces, the dissolved metal cations move from the interfacial region to the bulk solution [4]. The formation of solid metal hydroxide(s), $M(OH)_{n\,(s)}$ and therefore a hydrogel network, are local and negligible. In stage 2, the interfacial region is saturated with dissolved metal cations. Under these conditions, the hydrolysis equilibrium shifts to the right and triggers the precipitation of solid metal hydroxide(s) and consequently the development of a hydrogel network. In solutions containing strong oxidant(s), the hydrogel network can further develop through the formation and then precipitation of metal cations of a higher oxidation state. At longer times, the hydrogel network can dehydrate into solid crystal oxides which in turn further supress metal oxidation.

4.5 References

[1] R. G. Kelly, J. R. Scully, D. Shoesmith, and R. G. Buchheit, *Electrochemical Techniques in Corrosion Science and Engineering*. Marcel Dekker, Inc., 2003.

[2] W. S. Tait, “Chapter 5 - Electrochemical Corrosion Basics,” in *Handbook of Environmental Degradation of Materials*, 3rd Edition., M. Kutz, Ed. William Andrew Publishing, 2018, pp. 97–115. doi: 10.1016/B978-0-323-52472-8.00005-8.

[3] D. W. Shoesmith, “Kinetics of Aqueous Corrosion,” in *Corrosion: Fundamentals, Testing, and Protection*, vol. 13A, S. D. Cramer and B. S. Covino, Eds. ASM International, 2003, pp. 42–51.

[4] R. Karimihaghighi, “Non-Linear Effects of Solution Parameters and Gamma Radiation on Nickel Oxidation Dynamics,” The University of Western Ontario, 2021. Electronic Thesis and Dissertation Repository, Available: https://ir.lib.uwo.ca/etd/7789

[5] M. Naghizadeh, “Copper Corrosion Dynamics under Deep Geologic Repository Conditions,” The University of Western Ontario. Accessed: Aug. 12, 2021. Electronic Thesis and Dissertation Repository, Available: https://ir.lib.uwo.ca/etd/7894/

[6] L. Wu, D. Guo, M. Li, J. M. Joseph, J. J. Noël, P. G. Keech, and J. C. Wren, “Inverse Crevice Corrosion of Carbon Steel: Effect of Solution Volume to Surface Area,” *Journal of The Electrochemical Society*, vol. 164, no. 9, p. C539, Jul. 2017, doi: 10.1149/2.0511709jes.

[7] A. Y. Musa and J. C. Wren, “Combined effect of gamma-radiation and pH on corrosion of Ni–Cr–Fe alloy inconel 600,” *Corrosion Science*, vol. 109, pp. 1–12, Aug. 2016, doi: 10.1016/j.corsci.2016.03.015.

[8] K. Daub, X. Zhang, J. J. Noël, and J. C. Wren, “Gamma-radiation-induced corrosion of carbon steel in neutral and mildly basic water at 150 °C,” *Corrosion Science*, vol. 53, no. 1, pp. 11–16, Jan. 2011, doi: 10.1016/j.corsci.2010.09.048.

[9] J. M. Joseph, B. Seon Choi, P. Yakabuskie, and J. Clara Wren, “A combined experimental and model analysis on the effect of pH and O_2(aq) on γ-radiolytically produced H_2 and H_2O_2,” *Radiation Physics and Chemistry*, vol. 77, no. 9, pp. 1009–1020, Sep. 2008, doi: 10.1016/j.radphyschem.2008.06.001.

[10] P. Marcus, Ed., *Corrosion Mechanisms in Theory and Practice*, 3rd Edition. Boca Raton: CRC Press, 2011. doi: 10.1201/b11020.

[11] M. Momeni, “Gamma-Radiation Induced Corrosion of Alloy 800,” The University of Western Ontario, 2017. Electronic Thesis and Dissertation Repository, Available: https://ir.lib.uwo.ca/etd/5011

[12] C. F. Baes and R. E. Mesmer, *The Hydrolysis of Cations*. John Wiley & Sons, Inc., 1976.

[13] Y. G. Shin, “Nonlinear Dynamics of Carbon Steel Corrosion under Gamma Radiation,” Western University, 2020. Electronic Thesis and Dissertation Repository, Available: https://ir.lib.uwo.ca/etd/7339

[14] E. Glueckauf and G. P. Kitt, “The hydrogen content of atmospheric air at ground level,” *Quarterly Journal of the Royal Meteorological Society*, vol. 83, no. 358, pp. 522–528, Oct. 1957, doi: 10.1002/qj.49708335808.

[15] K. S. Schmitz, *Physical Chemistry*. Elsevier, 2017. doi: 10.1016/C2013-0-18556-X.

[16] I. S. Hwang, R. G. Ballinger, J. W. Prybylowski, and K. Hosoya, “Electrochemistry of Multiphase Nickel-Base Alloys in Aqueous Systems,” *Journal of The Electrochemical Society*, vol. 136, no. 7, pp. 1874–1883, Jul. 1989, doi: 10.1149/1.2097067.

[17] Z. Ahmad, *Principles of Corrosion Engineering and Corrosion Control*, 1st Edition. Elsevier Ltd., 2006.

CHAPTER 5

Time-Dependent Metal Oxidation Rate: The Effects of Solution pH, Temperature, and Redox and Transport Conditions

5.1 Introduction

In Chapter 4, the evolution of E_{corr} under different solution conditions (i.e., solution redox and transport conditions, pH and temperature) was studied. It was concluded that E_{corr} evolved as a function of the solution conditions. Although the rates of metal oxidation and oxidant (or solution) half-reactions in E_{corr} measurements are the same, these rates cannot be extracted. Therefore, the effect of solution redox and transport conditions on the rate of a metal oxidation half-reaction cannot be directly determined. Studying the potential-current relationship as a function of time is a useful method to extract the rate (i.e., current density) of a metal oxidation half-reaction.

The E_{corr} is the electrode potential (E_{elec}) under naturally corroding conditions. Similar to E_{corr}, the applied potential in a polarized experiment (e.g., cyclic voltammetry) is the electrode potential, meaning that it represents the potential of both metal and solution redox species. However, in a polarized experiment, the potential is controlled externally, as opposed to an E_{corr} experiment where the electrode potential is controlled by the solution redox environment.

The overpotential for a redox half-reaction is defined as ($\left|\eta_{rxn}\right| = \left|E_{elec} - E_{rxn}^{eq}\right|$) [1]. Since both E_{corr} and applied potential (E_{app}) are electrode potentials, the overpotential for a metal oxidation half-reaction is $\left|\eta_{ox}\right| = \left|E_{elec} - E_{ox}^{eq}\right|$ and the

overpotential for an oxidant (or solution) reduction half-reaction is $|\eta_{red}| = |E_{elec} - E_{red}^{eq}|$, where E_{ox}^{eq} is the equilibrium potential of an oxidation half-reaction and E_{red}^{eq} is equilibrium potential of an oxidant (or solution) reduction half-reaction.

The first part of the current Chapter discusses the cyclic voltammetry results without a prior E_{corr} measurement ($CV_{t=0}$). The second part of this Chapter studies the potentiodynamic (PD) scans which are obtained after 24 hours of E_{corr} measurement ($PD_{t=24}$) and $CV_{t=0}$. The potential at which the E_{app} becomes zero (in either $PD_{t=24}$ or $CV_{t=0}$) will be compared with the average value of the 1st and 2nd (pseudo-) steady-states in the E_{corr} measurements, and the time-dependent rate of the metal oxidation half-reaction will be discussed.

5.2 Experimental Procedures

In Chapter 3, the experimental procedures were explained in detail. In this Chapter, the effects of solution pH (10.6 and 6.0) and temperature (25 °C and 80 °C), and the range of scanned potentials on the $CV_{t=0}$ are discussed. The $PD_{t=24}$ were obtained by scanning the applied potential from 300 mV below (less noble) the value of E_{corr} at 24 hours to 300 mV above (more noble) the value of E_{corr} at 24 hours. The scan rate for both $CV_{t=0}$ and $PD_{t=24}$ experiments was 5 mV s^{-1}. Both E_{corr} measurements and $CV_{t=0}$ experiments were preceded by a cathodic cleaning step.

5.3 Results and Discussions

The average value of the 1st and 2nd (pseudo-) steady-states in the E_{corr} measurements (which were discussed in detail in Chapter 4) were compared with the potential at which the current density in $PD_{t=24}$ or $CV_{t=0}$ becomes zero. The potential at which the measured current density became zero is referred to as an $E^{i=0}$. This comparison was done at three pHs (10.6, 8.4 and 6.0), two temperatures (25 °C and 80 °C) and two concentrations of dissolved oxygen (solution under continuous argon purging and stagnant air-saturated solution).

At pH 10.6 and pH 6.0, the $CV_{t=0}$ was carried out in three different potential ranges. In this Chapter, only the first cycles from $CV_{t=0}$ will be presented and discussed. Each $CV_{t=0}$ started from an initial potential in the less positive (less noble) potential region. Then, the applied potential was scanned to a maximum potential in the more positive (more noble) potential direction. This half-cycle is referred to as positive potential scan. At the end of the positive potential scan, the applied potential was reversed to the initial potential. This half-cycle is referred to as negative potential scan.

The $CV_{t=0}$ and $PD_{t=24}$ results are presented in E vs. $\log|i|$ format, where E is E_{app} and i is the measured current density. $E^{i=0}$ occurs when the overall rate of all anodic reactions becomes equal to the overall rate of all cathodic reactions. In other words, $E^{i=0}$ is an applied potential at which measured current density is zero. In this Chapter, $E^{i=0}$ on the positive potential scan of $CV_{t=0}$ is referred to as $E_{CV_{t=0}}^{i=0,f}$. $E^{i=0}$ on $PD_{t=24}$ is referred to as $E_{PD_{t=24}}^{i=0,f}$.

5.3.1 $CV_{t=0}$, the effects of temperature and pH

The $CV_{t=0}$ results for solutions under continuous argon purging and stagnant air-saturated solutions are shown in **Figure 5.1** and **Figure 5.2**, respectively. The designations 'Ar' and 'air' refer to solutions under continuous argon purging and stagnant air-saturated solutions, respectively. The positive potential scans are shown with solid lines and the negative potential scans are shown with dashed lines. The equilibrium potentials of some relevant metal oxidation half-reactions and metal hydroxide redox reactions are also provided. The equilibrium potentials at 25 °C are shown with solid lines and the equilibrium potentials at 80 °C are shown with dotted lines. The horizontal dashed lines correspond to the equilibrium potential values. The overpotential is defined as the difference between the applied potential and the reversible potential, the latter being given by Nernst equation [2], [3]. Since the applied potential is the electrode potential in polarized experiments, the overpotential of a redox half-reaction is: $\left|\eta_{rxn}\right| = \left|E_{app} - E_{rxn}^{eq}\right|$. For a metal oxidation half-reaction, the overpotential is $\left|\eta_{ox}\right| =$

$\left|E_{app} - E_{ox}^{eq}\right|$ while for a solution reduction half-reaction, the overpotential is $\left|\eta_{red}\right| = \left|E_{app} - E_{red}^{eq}\right|$. The details of the equilibrium potential calculations at 25 °C and 80 °C are provided in **Appendix B**.

The $CV_{t=0}$ results are presented in a given redox condition. This is because the dissolved metal cation concentration gradient that is established between the metal/solution interface and the interfacial region/bulk solution interface is affected by solution flow. In solutions under continuous argon purging, the solution is convective, which results in faster removal of dissolved metal cations from the interfacial region/bulk solution interface than in stagnant air-saturated solutions. This affects the time required to saturate the interfacial region with a given dissolved metal cation. The saturation of the interfacial region is a prerequisite for the precipitation of metal hydroxides and the formation of a hydrogel network. Therefore, the effect of solution temperature or pH is studied in a given redox condition.

Figure 5.1 shows that at both pHs:

- $E_{CV_{t=0}}^{i=0,f}$ was nearly independent of the solution temperature. In addition, $E_{CV_{t=0}}^{i=0,f}$ was more positive (more noble) than $E_{Fe^0 \rightleftharpoons FeCr_2O_4}^{eq}$, slightly above (more positive than) $E_{Fe(OH)_2 \rightleftharpoons Fe_3O_4}^{eq}$ but less positive (less noble) than $E_{Ni^0 \rightleftharpoons \beta - Ni(OH)_2}^{eq}$.
- The cathodic current density in the positive potential scan decreased with increasing applied potential, up to $E_{CV_{t=0}}^{i=0,f}$, above which (at more positive (more noble) potentials) the current density changed to anodic. In addition, the cathodic current density in the positive potential scan was larger in magnitude at 80 °C than at 25 °C.
- In the $CV_{t=0}$ (short range), the cathodic current density in the negative potential scan was slightly larger than the cathodic current density in the positive potential scan. This behaviour was observed at both temperatures.

- At 25 °C, the anodic current density reached a maximum value at potentials more positive (more noble) than $E^{eq}_{Fe(OH)_2 \rightleftharpoons Fe_3O_4}$ (but less positive (less noble) than $E^{eq}_{Fe(OH)_2 \rightleftharpoons Fe(OH)_3}$) and then started decreasing as the potential was scanned to more noble direction. At potentials close to and more positive (more noble) than $E^{eq}_{Fe(OH)_2 \rightleftharpoons Fe(OH)_3}$, the anodic current density showed a slight increase with potential increase in the more positive (more noble) direction. This behaviour was more obvious at pH 6.0 than at pH 10.6 in the $CV_{t=0}$ long range.

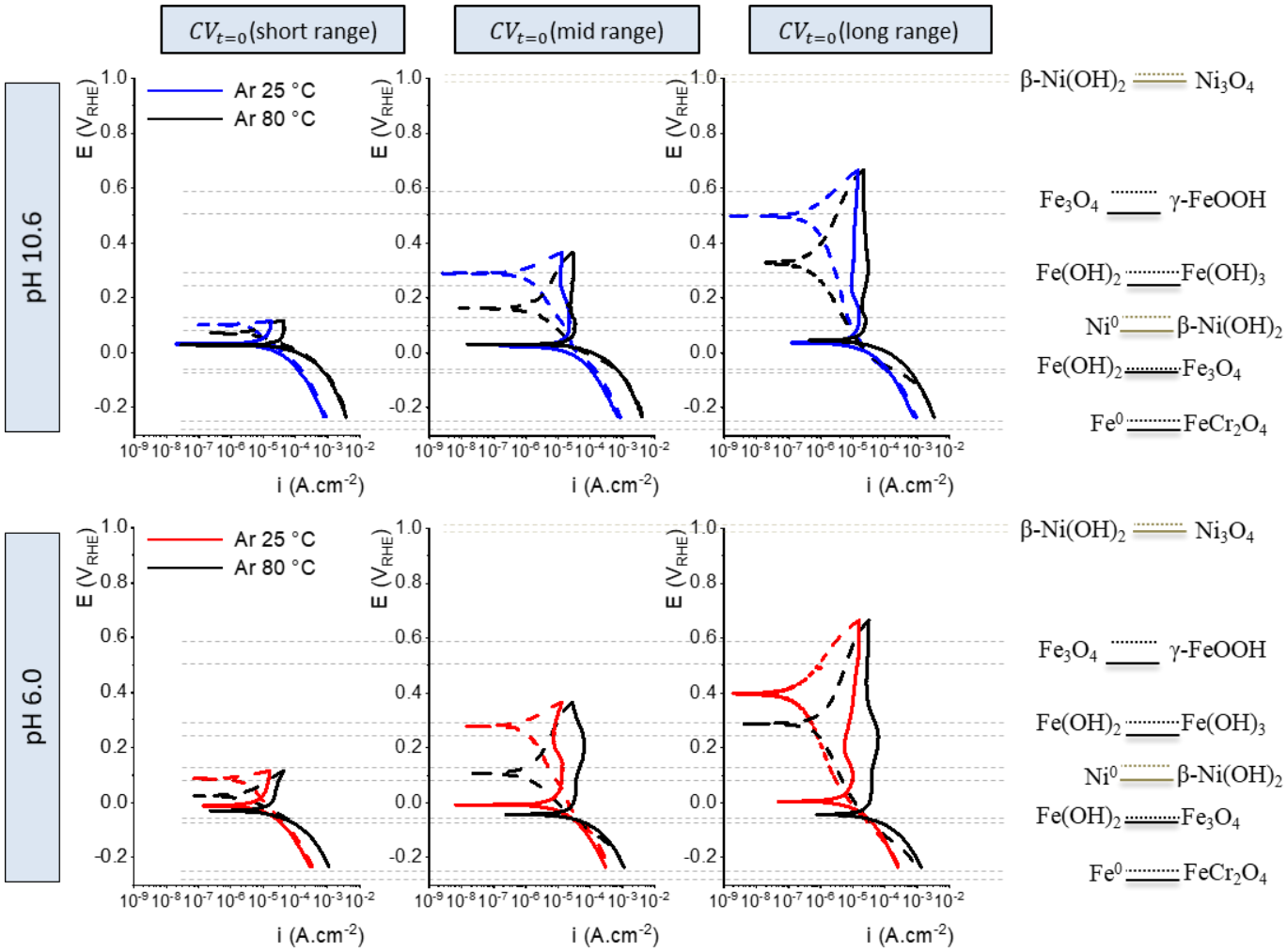

Figure 5.1 $CV_{t=0}$ (first cycle) in the solution under continuous argon purging at pH 10.6 (top) and pH 6.0 (bottom) at 25 °C (blue line for pH 10.6 and red line for pH 6.0) and 80 °C (black lines). Positive potential scan (solid line) and negative potential scan (dashed line).

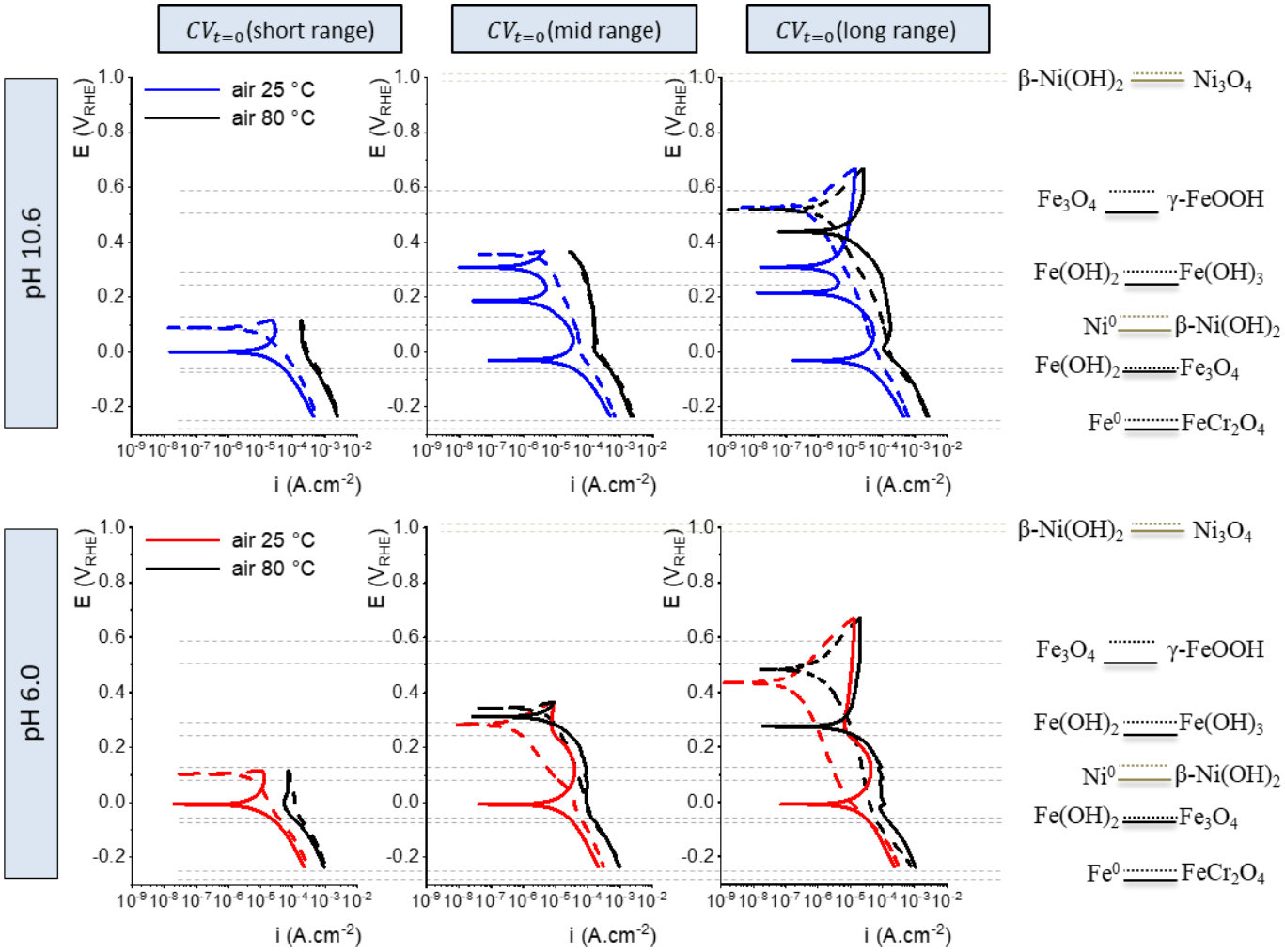

Figure 5.2 $CV_{t=0}$ (first cycle) in stagnant air-saturated solutions at pH 10.6 (top) and pH 6.0 (bottom) at 25 °C (blue line for pH 10.6 and red line for pH 6.0) and 80 °C (black lines). Positive potential scan (solid line) and negative potential scan (dashed line).

The $CV_{t=0}$ results in stagnant air-saturated solutions are shown in **Figure 5.2**. At pH 10.6 and 25 °C, the $E - \log|i|$ graph on the positive potential scan showed more than one $E^{i=0}$. Of three $E^{i=0}$ occurrences, the one located at the least positive (least noble) potential is referred to as $E_{CV_{t=0}}^{i=0,f}$. The middle $E^{i=0}$ occurrence and the $E^{i=0}$ occurrence located at the most positive (most noble) potential are referred to as $E_{CV_{t=0}}^{i=0,m}$ and $E_{CV_{t=0}}^{i=0,u}$, respectively. Between $E_{CV_{t=0}}^{i=0,m}$ and $E_{CV_{t=0}}^{i=0,u}$, the measured current density is cathodic—which is referred to as the cathodic loop. The maximum current density in the cathodic loop corresponded to $E_{Fe(OH)_2 \rightleftharpoons Fe(OH)_3}^{eq}$.

Figure 5.2 shows that at both pHs:

- The cathodic current density in the positive potential scan decreased with increased applied potential at both 25 °C and 80 °C. However, at 80 °C the cathodic current density changed its slope while at 25 °C, the cathodic current density was dominated by the anodic current density. The potential at which either of these changes occurred was well above (more positive than) $E_{Fe^0 \rightleftharpoons FeCr_2O_4}^{eq}$ and slightly above (more positive than) $E_{Fe(OH)_2 \rightleftharpoons Fe_3O_4}^{eq}$ but below (less positive than) $E_{Ni^0 \rightleftharpoons \beta - Ni(OH)_2}^{eq}$.
- The current density in the positive potential scan was larger in magnitude at 80 °C than at 25 °C.
- In the $CV_{t=0}$ (short range), the current density remained cathodic at 80 °C. In addition, the cathodic current density in the negative potential scan was slightly larger than the cathodic current density in the positive potential scan. This behaviour was also observed at 25 °C.
- At 25 °C, the anodic current density reached a maximum value at potentials more positive (more noble) than $E_{Fe(OH)_2 \rightleftharpoons Fe_3O_4}^{eq}$ (but less positive (less noble) than $E_{Fe(OH)_2 \rightleftharpoons Fe(OH)_3}^{eq}$) and then started decreasing as the potential was scanned to more positive (more noble) direction. At pH 10.6, the current density changed from anodic to cathodic at potentials less

positive (less noble) than $E^{eq}_{Fe(OH)_2 \rightleftharpoons Fe(OH)_3}$ and showed a cathodic loop. However, at potentials more positive (more noble) than $E^{eq}_{Fe(OH)_2 \rightleftharpoons Fe(OH)_3}$ the current density became anodic and started increasing with potential increase in the more positive (more noble) direction. At pH 6.0, the cathodic loop was absent but the anodic current density started increasing with potential increase in the more positive (more noble) direction (from potentials close to and more positive (more noble) than $E^{eq}_{Fe(OH)_2 \rightleftharpoons Fe(OH)_3}$).

The effect of solution pH on the positive potential scan of $CV_{t=0}$ results is shown in **Figure 5.3.** In polarized techniques (e.g., cyclic voltammetry), the electrode potential is controlled externally. During a positive potential scan, the potential changes with time (from less positive (less noble) to more positive (more noble) potentials) and the overpotential for metal oxidation half-reaction increases as the potential is scanned from less positive (less noble) to more positive (more noble) potentials. For a metal cation with a higher solubility limit at a lower solution pH, the interfacial region will be saturated faster at a given scan rate (in the positive potential scan) at a higher solution pH. Therefore, when other parameters are constant and only pH increases (and metal cation solubility limit decreases), the interfacial region saturates faster at the same potential (which corresponds to the same duration). Increasing the solution pH from 6.0 to 10.6 decreases the solubility limits of both $Fe(OH)_2$ and $Ni(OH)_2$ by nearly seven orders of magnitude [4]. However, the solubility limit of a metal cation in the presence of a mixed metal hydroxide (such as the one that forms on the surface of Inconel X-750) is not necessarily the same as that of a metal hydroxide in its pure form (e.g., $Fe(OH)_2$), see Chapter 6 for more details.

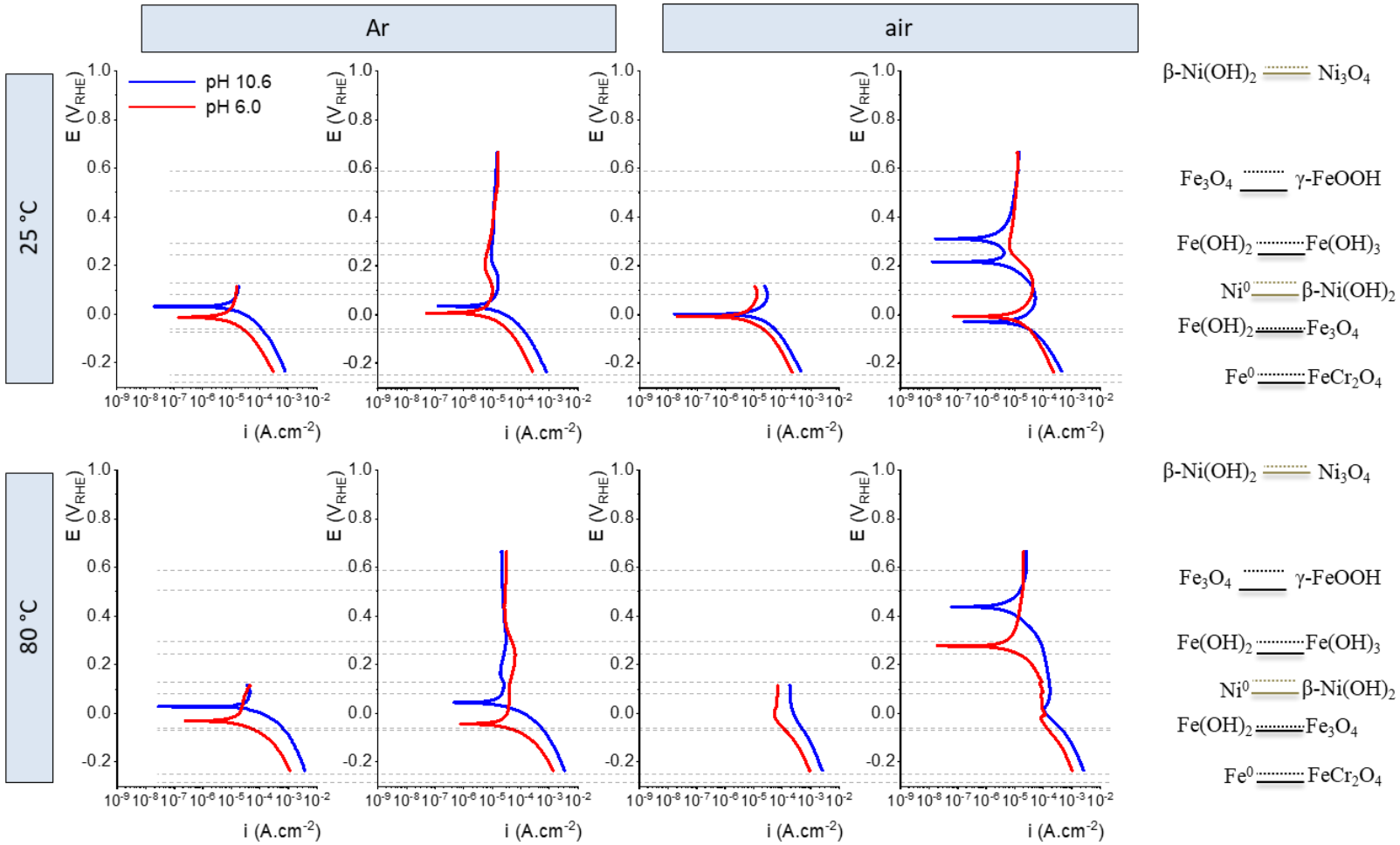

Figure 5.3 The effect of solution pH on the $E - \log|i|$ behaviour in positive potential scans at 25 °C (top) and 80 °C (bottom).

The comparison of positive potential scans in **Figure 5.3** shows that:

- In both redox environments, irrespective of solution temperature, $E_{CV_{t=0}}^{i=0,f}$ was always less positive (less noble) at pH 6.0 than at pH 10.6—except in stagnant air-saturated solution at 25 °C where $E_{CV_{t=0}}^{i=0,f}$ occurrences were close and the difference was not significant.
- The cathodic current density at pH 10.6 was always larger than that at pH 6.0, regardless of solution temperature or redox environment.

5.3.2 Correlation of $CV_{t=0}$ and $PD_{t=24}$ with steady-state E_{corr}

In Chapter 4, it was concluded that E_{corr} evolved in a quasi-stepwise manner. E_{corr} reached the 1st (pseudo-) steady-state value very rapidly (within less than a second). In addition, E_{corr} did not remain in the1st (pseudo-) steady-state. Rather, it evolved to the 2nd (pseudo-) steady-state. During the 1st and 2nd (pseudo-) steady-states, the E_{corr} changed slowly indicating that the redox reactions occurring on the corroding metal were in quasi-equilibrium (i.e., steady-state).

In this section, the $E_{CV_{t=0}}^{i=0,f}$ values are compared with the average value of E_{corr} in the 1st (pseudo-) steady-state, while the $E_{PD_{t=24}}^{i=0,f}$ values are compared with the average value of E_{corr} in the 2nd (pseudo-) steady-state. These comparisons are graphically shown in **Figure 5.4** (for pH 10.6), **Figure 5.5** (for pH 8.4) and **Figure 5.6** (for pH 6.0).

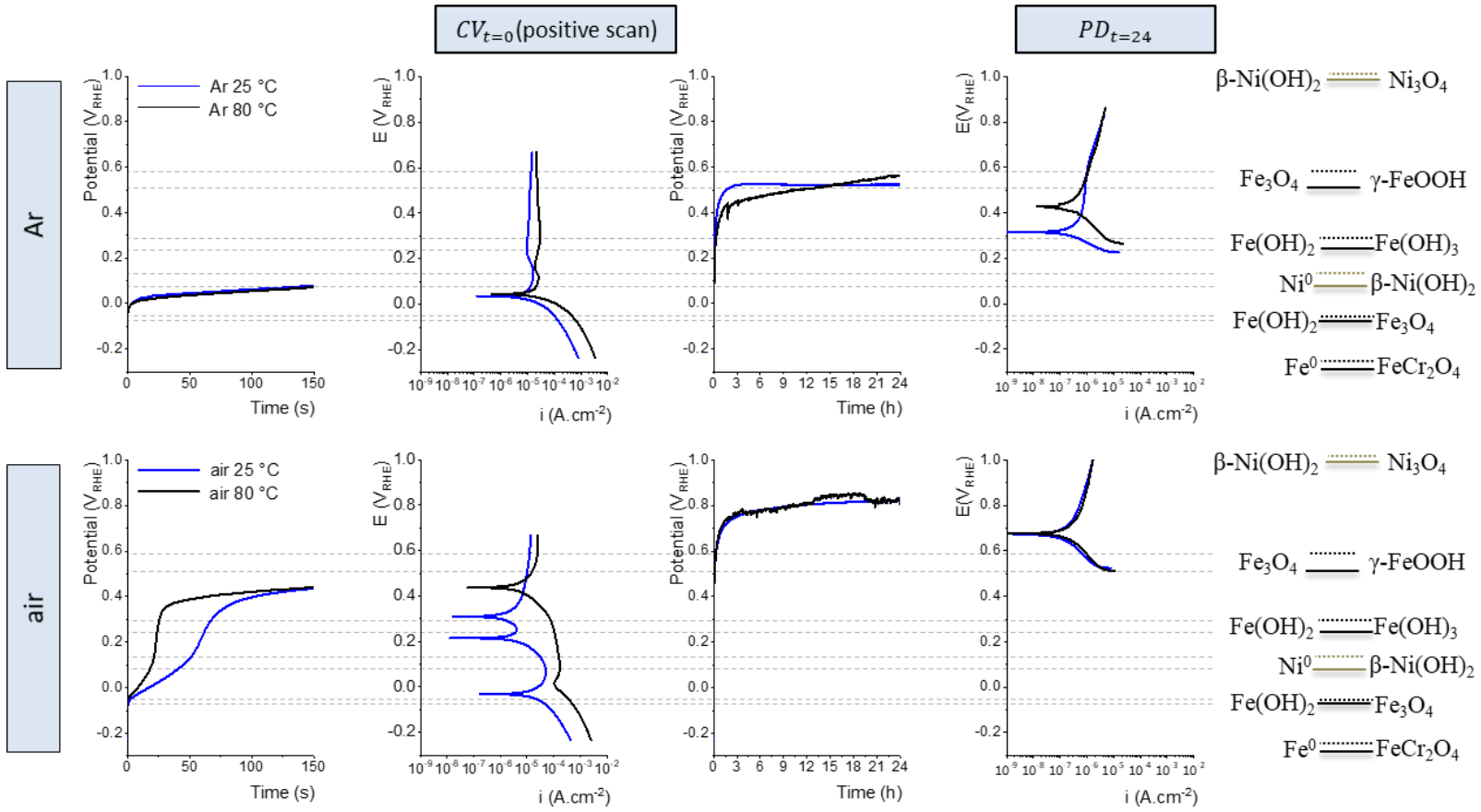

Figure 5.4 Comparison of $E_{CV_{t=0}}^{i=0,f}$ and $E_{PD_{t=24}}^{i=0,f}$ (at pH 10.6) with the average values of E_{corr} in the 1st and 2nd (pseudo-) steady-states, respectively, in solution under continuous argon purging (top) and in stagnant air-saturated solution (bottom).

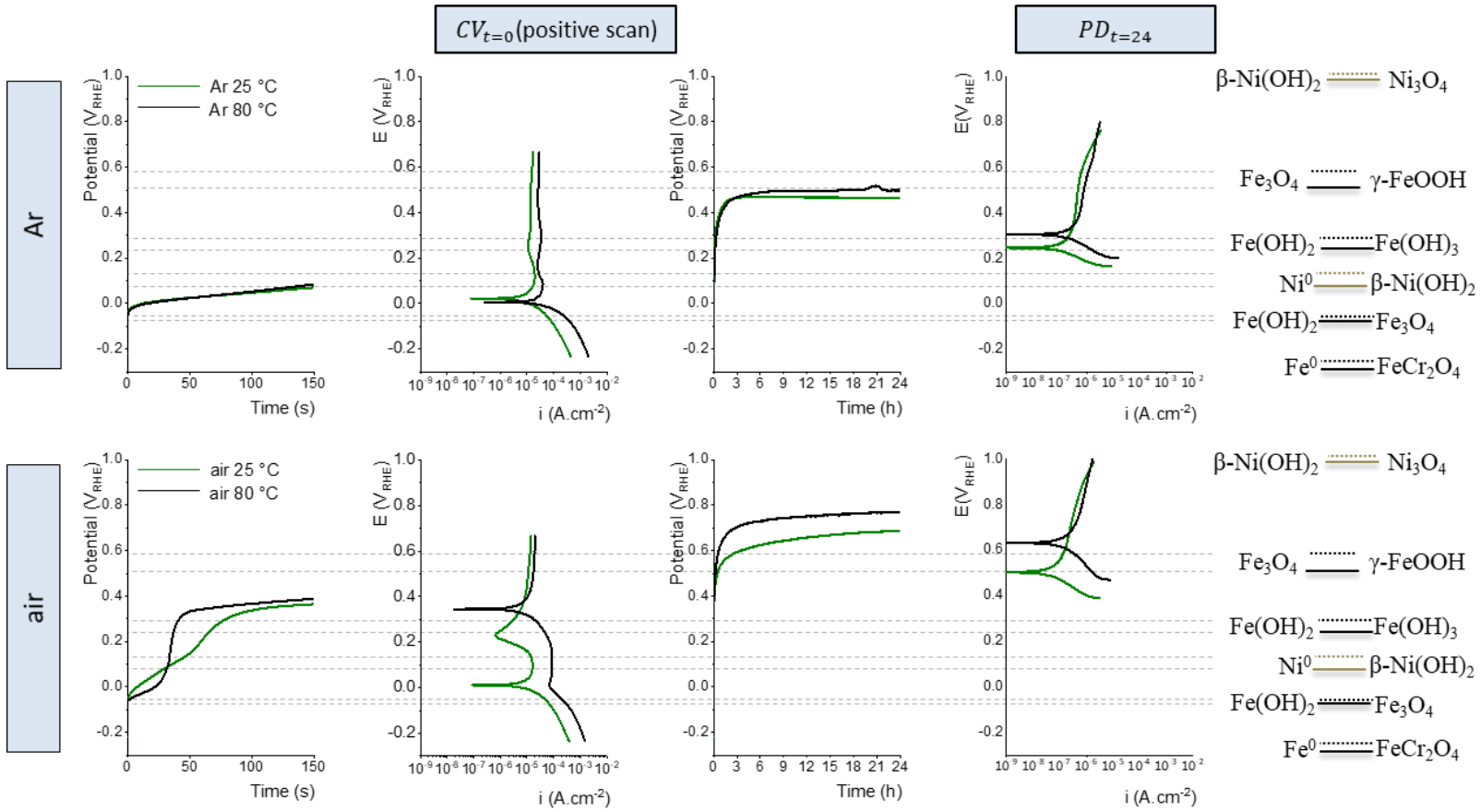

Figure 5.5 Comparison of $E_{CV_{t=0}}^{i=0,f}$ and $E_{PD_{t=24}}^{i=0,f}$ (at pH 8.4) with the average values of E_{corr} in the 1st and 2nd (pseudo-) steady-states, respectively, in solution under continuous argon purging (top) and in stagnant air-saturated solution (bottom).

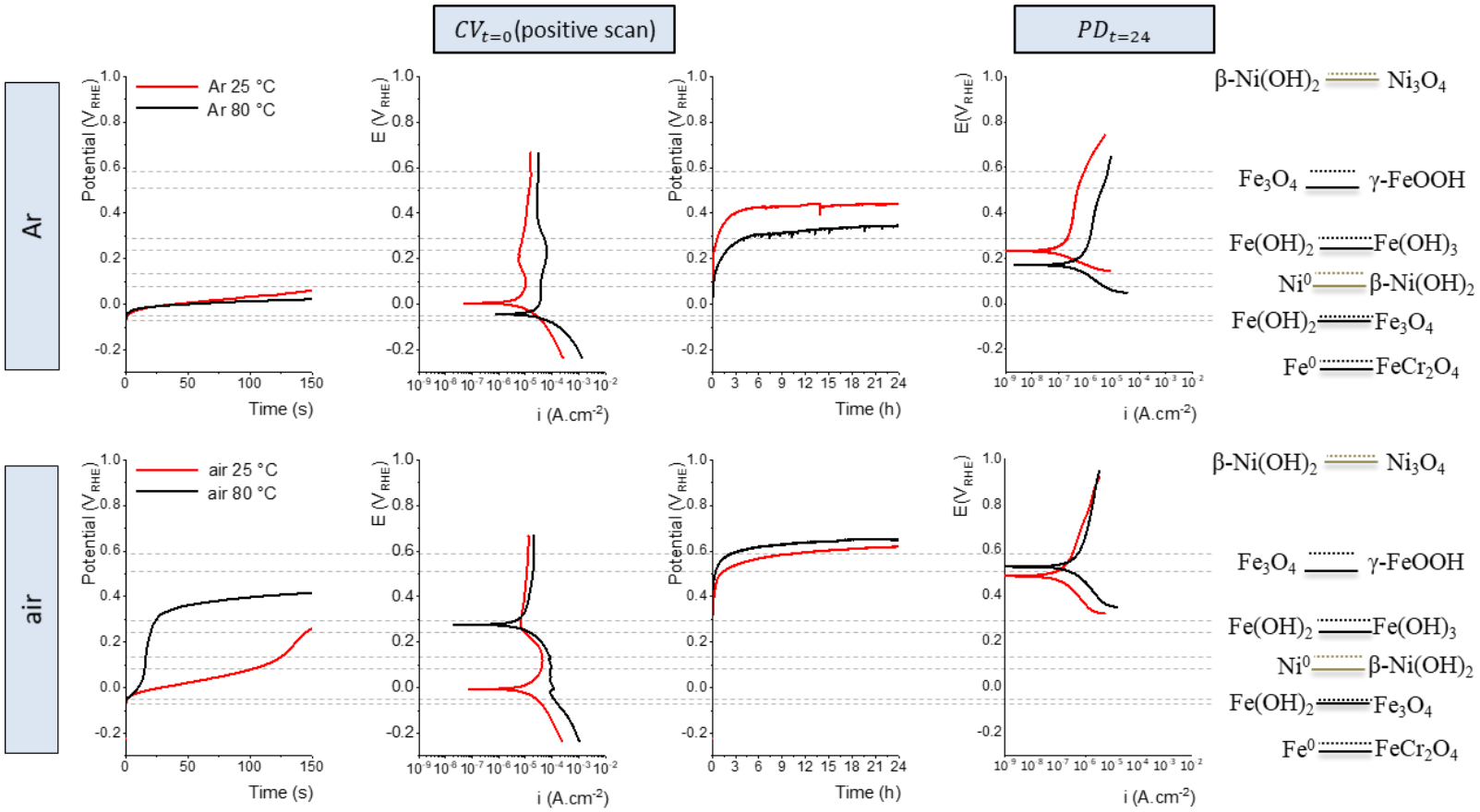

Figure 5.6 Comparison of $E_{CV_{t=0}}^{i=0,f}$ and $E_{PD_{t=24}}^{i=0,f}$ (at pH 6.0) with the average values of E_{corr} in the 1st and 2nd (pseudo-) steady-states, respectively, in solution under continuous argon purging (top) and in stagnant air-saturated solution (bottom).

The results from **Figure 5.4**, **Figure 5.5** and **Figure 5.6** shows that at all pHs:

- The average value of E_{corr} in the 1st (pseudo-) steady-state corresponded to $E_{CV_{t=0}}^{i=0,f}$ in both redox environments—except at 80 °C in stagnant air-saturated solution.
- A temperature increase shifted the $E_{CV_{t=0}}^{i=0,f}$ in stagnant air-saturated solution to more positive (more noble) potentials. In addition, the $E_{CV_{t=0}}^{i=0,f}$ at 80 °C in stagnant air-saturated solution corresponded to the E_{corr} value right after the sharp rise at the end of the 1st (pseudo-) steady-state.
- $E_{CV_{t=0}}^{i=0,f}$ located at a less positive (less noble) potential than $E_{PD_{t=24}}^{i=0,f}$. In addition, the extracted corrosion current (i_{corr}) corresponding to the $E_{CV_{t=0}}^{i=0,f}$ was always larger than the i_{corr} corresponding to $E_{PD_{t=24}}^{i=0,f}$; extracted i_{corr} values are not shown.

In Chapter 4, it was concluded that the corrosion of a metal starts with metal oxidation (reaction 1) followed by the transfer of oxidized metal cations from the metal site ($M_{(m)|int}^{n+}$) to the interfacial region ($M_{(aq)|int}^{n+}$) and then to the bulk solution (reaction 2). The transport of dissolved metal cations in the interfacial region to the bulk solution occurs due to the different concentrations of dissolved metal cations in the interfacial region and bulk solution [1]:

$$M_{(m)|int}^{0} \rightleftharpoons M_{(m)|int}^{n+} + ne^{-} \quad (1)$$

$$M_{(aq)|int}^{n+} \rightsquigarrow M_{(aq)|bulk}^{n+} \quad (2)$$

The dissolved metal cations in the interfacial region undergo hydrolysis (reaction 3, [5]):

$$M_{(aq)}^{n+} + xOH^{-} \rightleftharpoons M(OH)_{x\,(aq)}^{(n-x)+} \quad (3)$$

where x is 1, 2, ... n+1 [5]. When the rate of metal oxidation (reaction 1) is fast and the rate of metal cations transport to the bulk solution (reaction 2) is slow, the interfacial region becomes supersaturated with the dissolved metal cations and corrosion products can deposit on the surface as oxides/hydroxides (reaction 4) [3]. The hydroxides of transition metals are hygroscopic and form a hydrogel network upon precipitating as colloidal particles [6], [1], [7].

$$M_{(aq)}^{n+} \rightleftharpoons M(OH)_{n\,(s)} \tag{4}$$

The results discussed above showed that increasing the solution temperature shifted the $E_{CV_{t=0}}^{i=0,f}$ to more positive (more noble) potential only in stagnant air-saturated solution. In both solutions (i.e., solution under continuous argon purging and stagnant air-saturated solution) the rate of the hydrolysis reaction (reaction 3) and the applied potential are independent of the redox properties of the solution—as the latter is being controlled externally. The absence of a shift in $E_{CV_{t=0}}^{i=0,f}$ to a more positive value in solution under continuous argon purging can be explained by the solution transport conditions.

It should be noted that the solution in contact with the metal is an open chemical system [7]. In solutions under continuous argon purging, the dissolved metal cations are removed by the solution flow from the interfacial region/bulk solution interface faster than for stagnant air-saturated solutions. The rate of dissolved metal cation transport from the interfacial region to the bulk solution depends on the concentration gradient between them [1]. The interfacial solution/bulk solution interface remains dilute with regard to metal cations in solutions under continuous argon purging which creates a larger concentration gradient of dissolved metal cations across the interfacial region. In stagnant air-saturated solutions, the slower rate of metal cation transport from the interfacial solution/bulk solution interface results in a faster build-up of dissolved metal cations in the interfacial region—and a smaller concentration gradient across the interfacial region. The faster saturation of the interfacial region shifts the hydrolysis equilibrium (reaction 3) to the right. As mentioned above, the hydroxides of transition metals are hygroscopic and form a hydrogel network upon precipitating as colloidal particles [6], [1], [7]. The

hydrogel network (i.e., the deposited corrosion products) slows down the transport of dissolved metal cations from the corroding surface (metal/solution interface) to the interfacial region and to the bulk solution [7], [2].

One could ask why the shift in $E^{i=0,f}$ (in the $CV_{t=0}$ results) to more positive (more noble) potential in stagnant air-saturated solution happened only at 80 °C and not at 25 °C. This question can be answered by considering the effect of increased temperature on the rate of metal cation hydrolysis (reaction 3). When the solution temperature increases from room temperature to 80 °C, the rate of hydrolysis reaction (reaction 3) increases resulting in a faster formation of a metal hydroxide (reaction 4) [8]. At 25 °C, the slower rate of reaction 3 (compared to 80 °C) slows down the formation of a hydrogel network—the hydrogel network grows to a lesser extent.

In the presence of a hydrogel network, the oxidation of dissolved metal cations (e.g., $Fe^{2+}_{(aq)}$) is faster. This is because the oxidation of a dissolved metal cation to a higher oxidation state (e.g., $Fe^{3+}_{(aq)}$) on the surface of the hydrogel network (reaction 5) has a lower activation energy than metal cation oxidation in the solution [1], [9].

$$\left\{M^{n+}_{(aq)|int} \rightleftharpoons M(OH)_n\right\} \rightleftharpoons \left\{M^{(n+1)+}_{(aq)|int} \rightleftharpoons M(OH)_{n+1}\right\} + e^- \quad (5)$$

Once the interfacial region has become saturated with dissolved metal cations of a higher oxidation state (e.g., $Fe^{3+}_{(aq)}$), hydroxide particles ($Fe(OH)_{3\,(s)}$) precipitate and a hydrogel network develops. That is, the hydrogel network evolves into one with a mixture of metal cations of different oxidation states. Dissolved metal cations of a higher oxidation state (e.g., $Fe^{3+}_{(aq)}$) can also reduce on the surface and generate cathodic current. This is reflected through the shift of $E^{i=0,f}_{CV_{t=0}}$ results to a more positive (more noble) potential.

Interestingly, the shift of $E^{i=0,f}_{CV_{t=0}}$ to more positive (more noble) potential in stagnant air-saturated solution that occurred at 80 °C, also occurred at pH 6.0. Given the seven orders of magnitude larger solubilities of both $Fe(OH)_2$ and $Ni(OH)_2$ at pH 6.0

than at pH 10.6 [4], this behaviour is counter-intuitive and requires some explanation. Interestingly, the potential at which the slope of the cathodic line in the positive potential scan potential changed (in stagnant air-saturated solution at 80 °C) was nearly the same (slightly more positive at pH 10.6 than at pH 6.0) at all three pHs: 0.0 V_{RHE}. This behaviour is observable for pH 10.6 and pH 6.0 in **Figure 5.3**. However, the magnitude of the shift of $E_{CV_{t=0}}^{i=0,f}$ to more positive (more noble) potentials was largest at pH 10.6 and smallest at pH 6.0 (and that of pH 8.4 was in between). As mentioned above, once the hydrogel network forms on the surface, the reduction of dissolved metal cations of a higher oxidation state (e.g., $Fe_{(aq)}^{3+}$) can contribute to the cathodic current—and can increase the magnitude of the cathodic current density. Under these conditions (i.e., once $Fe_{(aq)}^{3+}$ forms in the interfacial region) the contribution of H^+ reduction reaction to the overall cathodic current density becomes negligible [10].

The solubility limits of pure $Fe(OH)_2$ and $Ni(OH)_2$ sharply increase as solution pH decreases (for the range of pHs studied in this project) [4]. However, as the solution pH decreases, the solubility limits of Fe^{II} and Ni^{II} for a mixed metal hydroxide (such as the one that forms on the surface of Inconel X-750) do not necessarily increase by the same factor as the solubility limits of Fe^{II} and Ni^{II} in their pure forms. As will be discussed further in Chapter 6, the main effect of decreasing the solution pH from 10.6 to 6.0 is to increase Ni^{II} dissolution. The same pH decrease has a smaller effect on increasing the dissolutions of Fe^{II} (and Cr^{III}). Therefore, the mixed hydrogel networks that form at different pHs are slightly different. This explains the observation of a positive (more noble) shift of $E_{CV_{t=0}}^{i=0,f}$ at all three pHs in stagnant air-saturated solutions at 80 °C but with different magnitudes in the shift for each pH.

The cathodic current generated by the reduction of dissolved metal cations of a higher oxidation state (e.g., $Fe_{(aq)}^{3+}$) allows for a better understanding of the $E - \log|i|$ graph in stagnant air-saturated solutions at pH 10.6 and 25 °C. The anodic current density is determined by the overpotential for the metal oxidation half-reaction. This overpotential is controlled externally ($|\eta_{ox}| = |E_{app} - E_{ox}^{eq}|$). On the other hand, the

magnitude of the cathodic current density depends on whether a hydrogel network has formed in the interfacial region or not. More specifically, before the formation of a hydrogel network, the magnitude of the cathodic current density depends on the concentration of the initial oxidant (e.g., H^+) and the applied potential ($\left|\eta_{red}\right| = \left|E_{app} - E_{red}^{eq}\right|$). Once the hydrogel network forms, the reduction of dissolved metal cations of a higher oxidation state (e.g., $Fe_{(aq)}^{3+}$) can contribute to the overall cathodic current density, and under these conditions, the contribution of oxidant(s) (e.g., H^+) to the reduction reaction become secondary and negligible [10]. The competition between the anodic and the cathodic current densities explains the observation of multiple $E^{i=0}$ occurrences and a cathodic loop in the $E - \log|i|$ graph in stagnant air-saturated solution at 25 °C and at pH 10.6. At potentials more positive (more noble) than $E_{Fe(OH)_2 \rightleftharpoons Fe(OH)_3}^{eq}$, the reduction of dissolved metal cations of a higher oxidation state (e.g., $Fe_{(aq)}^{3+}$) becomes negligible—since $Fe_{(aq)}^{3+}$ will no longer be stable at higher (more noble) potentials. Therefore, at applied potentials more positive (more noble) than $E_{Fe(OH)_2 \rightleftharpoons Fe(OH)_3}^{eq}$, the anodic current density associated with the metal oxidation half-reaction dominates the overall cathodic current density and the measured current density remains anodic. This is consistent with the observations in solution under continuous argon purging at 25 °C where the anodic current density reached a maximum value followed by a decrease in anodic current density at potentials more positive (more noble) than $E_{Fe(OH)_2 \rightleftharpoons Fe_3O_4}^{eq}$ (but less positive (less noble) than $E_{Fe(OH)_2 \rightleftharpoons Fe(OH)_3}^{eq}$ and the slight increase in anodic current density at potentials more positive (more noble) than $E_{Fe(OH)_2 \rightleftharpoons Fe(OH)_3}^{eq}$.

In the $CV_{t=0}$ (short range), it was observed that in both redox environments, the cathodic current density in the negative potential scan was slightly larger than that in the positive potential scan. In addition, the difference in magnitude of the cathodic current density between the positive and negative potential scans was larger in stagnant air-saturated solutions than in solutions under continuous argon purging. In Chapter 4, it was mentioned that the solubility of dissolved oxygen in solutions under continuous argon purging was not zero—reported as 75 ppb in deaerated water [11]. Therefore, the

formation of metal cations of a higher oxidation state ($Fe^{3+}_{(aq)|int}$) can also occur in solutions under continuous argon purging. Once a metal cation of a higher oxidation state ($Fe^{3+}_{(aq)|int}$) is generated, its contribution to the overall cathodic current density surpasses that of the initial oxidant (i.e., H^+). This explains the observation of a larger cathodic current density in the negative potential scan than in the positive potential scan in both redox environments at both temperatures.

In the positive potential scan and prior to the formation of a hydrogel network (and consequently a metal cation of a higher oxidation state ($Fe^{3+}_{(aq)|int}$)), the main reduction reaction is H^+ reduction reaction. Hydrogen evolution is a very complicated reaction with several steps each having multiple stages [12]. However, the observation of a larger (in magnitude) cathodic current density in the positive potential scan at 80 °C than at 25 °C for all pHs, **Figure 5.3**, can indicate the effect of temperature on increasing the overall rate of H^+ reduction reaction.

The results in **Figure 5.3** show that the magnitude of the cathodic current density in the positive potential scan was larger at pH 10.6 than at pH 6.0. This behaviour was observed in both redox environments (solutions under continuous argon purging and stagnant air-saturated solutions) and at both temperatures (25 °C and 80 °C). As mentioned in Chapter 4, the oxidation of Ni to dissolved $Ni^{2+}_{(aq)}$ can happen at potentials below (less positive than) the E^{eq}_{rxn} of Ni species (i.e., $E^{eq}_{Ni^0 \rightleftharpoons \beta - Ni(OH)_2}$). In addition, the main effect of decreasing the solution pH is to increase Ni^{II} dissolution; the dissolution of Fe^{II} and Cr^{III} also increases, but to a lesser extent. The measured current density is the sum of all anodic and all cathodic currents. The much larger contribution of metal oxidation to the overall anodic current explains the lower cathodic current density at pH 6.0 than at pH 10.6 in the positive potential scan.

The comparison of i_{corr} values from $CV_{t=0}$ and $PD_{t=24}$ showed that the i_{corr} corresponding to $E^{i=0,f}_{CV_{t=0}}$ was always larger in magnitude than that in $PD_{t=24}$. This observation indicates that the hydrogel network can convert to crystal oxide particles at

longer times, which further decreases the rate of metal oxidation [1]. Metal oxidation is largely inhibited in the presence of solid crystal particles. Therefore, i_{corr} decreases significantly. This is an indication that corrosion has evolved to stage 3.

The observations from this Chapter were in agreement with the findings from Chapter 4. The results showed that the corrosion of Inconel X-750 occurred in three mains stages. During the positive potential scan (in the first cycle of cyclic voltammetry), the corrosion process can extend beyond stage 1. The evolution of corrosion system to stage 2 is more likely in stagnant solutions, in the presence of more dissolved oxygen, at a higher temperature (i.e., 80 °C versus 25 °C) and when the rang of scanned potential is extended to more positive (more noble) values. In addition, this evolution is independent of the solution pH (for the range of pH studied in this Chapter). The $PD_{t=24}$ results indicated that the rate of metal oxidation decreases considerably over time due to the development of a hydrogel network and the formation of solid crystal oxides. The three stages of corrosion evolution are as follows:

Stage 1: The interfacial region is free of dissolved metal cations. The dissolved metal cations move from the interfacial region to the bulk solution as a result of the concentration gradient that is established across the interfacial region [1]. In conditions where the solution experiences a convective flow (such as in a solution under continuous argon purging), the transport of the dissolved metal cations is faster due to a larger concentration gradient across the interfacial region. As a result, the interfacial region remains dilute of metal cations for a longer duration than for stagnant solution conditions.

Stage 2: Once the interfacial region is saturated with dissolved metal cations, the yield of the hydrolysis reaction becomes significant. This results in the precipitation of solid metal hydroxide on the surface. The precipitated solid metal hydroxide particles on the surface result in the development of a hydrogel network. In solution conditions where the rate of the hydrolysis reaction is faster and the solution is not agitated (e.g., at 80 °C and in stagnant air-saturated solutions), the hydrogel network forms faster. In the presence of a hydrogel network, the oxidation of metal atoms from the metal surface and

the transport of oxidized metal cations generated at the metal/solution interface through the hydrogel network, then interfacial region and finally to the bulk solution, is more difficult. This results in a slower rate of metal oxidation in stage 2 than in stage 1.

Once the hydrogel network forms on the surface, it can develop over time through the electrochemical oxidation of dissolved metal cations in the interfacial region. In more oxidizing conditions, the dissolved metal cations can oxidize to metal cations of a higher oxidation state. Once such a higher oxidation metal cation reaches its solubility limit in the interfacial region (the solution that is in contact with the precipitated hydrogel network), it undergoes hydrolysis and precipitates as solid metal hydroxide particles.

Stage 3: The hydrogel network can dehydrate and form solid crystal oxides. The formation and growth of oxide particles increases at higher temperatures (80 °C compared to room temperature). This is because bond formation is a high activation energy process [9]. In the presence of solid crystal oxides, metal oxidation reactions are further limited and the overall metal oxidation current decreases.

5.4 Conclusions

The results obtained in this Chapter were in agreement with the findings from E_{corr} in Chapter 4 and confirmed that corrosion of Inconel X-750 occurs in three main stages. In the positive potential scan (in the first cycle of cyclic voltammetry), the corrosion evolution from stage 1 to stage 2 is more likely in stagnant solutions, in the presence of more dissolved oxygen, at a higher temperature and when the rang of scanned potential is extended to more positive (more noble) values. For example, at higher temperatures (e.g., 80 °C) where the rate of the hydrolysis reaction is faster, and in solutions with stronger oxidant(s), the hydrogel network can develop to incorporate metal hydroxides of higher oxidation states (e.g., $Fe^{3+}_{(aq)}$).

At longer times, the hydrogel network can develop and change into a mixture of solid metal hydroxides of different oxidation states. The hydrogel network can dehydrate

and convert to solid crystal oxides. These solid crystal oxides can significantly decrease the rate of metal oxidation (i.e., corrosion current (i_{corr})).

5.5 References

[1] R. Karimihaghighi, "Non-Linear Effects of Solution Parameters and Gamma Radiation on Nickel Oxidation Dynamics," The University of Western Ontario, 2021. Electronic Thesis and Dissertation Repository, Available: https://ir.lib.uwo.ca/etd/7789

[2] R. G. Kelly, J. R. Scully, D. Shoesmith, and R. G. Buchheit, *Electrochemical Techniques in Corrosion Science and Engineering*. Marcel Dekker, Inc., 2003.

[3] D. W. Shoesmith, "Kinetics of Aqueous Corrosion," in *Corrosion: Fundamentals, Testing, and Protection*, vol. 13A, S. D. Cramer and B. S. Covino, Eds. ASM International, 2003, pp. 42–51.

[4] C. F. Baes and R. E. Mesmer, *The Hydrolysis of Cations*. John Wiley & Sons, Inc., 1976.

[5] A. Y. Musa and J. C. Wren, "Combined effect of gamma-radiation and pH on corrosion of Ni–Cr–Fe alloy inconel 600," *Corrosion Science*, vol. 109, pp. 1–12, Aug. 2016, doi: 10.1016/j.corsci.2016.03.015.

[6] Y. G. Shin, "Nonlinear Dynamics of Carbon Steel Corrosion under Gamma Radiation," Western University, 2020. Electronic Thesis and Dissertation Repository, Available: https://ir.lib.uwo.ca/etd/7339

[7] M. Naghizadeh, "Copper Corrosion Dynamics under Deep Geologic Repository Conditions," The University of Western Ontario. Accessed: Aug. 12, 2021. Electronic Thesis and Dissertation Repository, Available: https://ir.lib.uwo.ca/etd/7894/

[8] M. Momeni, "Gamma-Radiation Induced Corrosion of Alloy 800," The University of Western Ontario, 2017. Electronic Thesis and Dissertation Repository, Available: https://ir.lib.uwo.ca/etd/5011

[9] L. Wu, D. Guo, M. Li, J. M. Joseph, J. J. Noël, P. G. Keech, and J. C. Wren, "Inverse Crevice Corrosion of Carbon Steel: Effect of Solution Volume to Surface Area," *Journal of The Electrochemical Society*, vol. 164, no. 9, p. C539, Jul. 2017, doi: 10.1149/2.0511709jes.

[10] Z. Ahmad, *Principles of Corrosion Engineering and Corrosion Control*, 1st Edition. Elsevier Ltd., 2006.

[11] I. S. Hwang, R. G. Ballinger, J. W. Prybylowski, and K. Hosoya, "Electrochemistry of Multiphase Nickel-Base Alloys in Aqueous Systems," *Journal of The Electrochemical Society*, vol. 136, no. 7, pp. 1874–1883, Jul. 1989, doi: 10.1149/1.2097067.

[12] J. C. Scully, *The fundamentals of corrosion*, 3rd Edition. Pergamon press, 1990.

CHAPTER 6

Time-Dependent Corrosion Behaviour of Inconel X-750 at 25 °C – 150 °C: The Effects of pH, Temperature, Oxygen Concentration and Gamma-Radiation

6.1 Introduction

In nuclear power plants, nickel-based superalloys are used for thin-walled heat exchanger tubing, spacers such as garter springs in the annular gap between the pressure and calandria tubes in CANDU reactors, and bolts and guide pins in PWRs and in BWRs [1]–[3]. Nickel-based superalloys can be exposed to various solution environments which can affect the metal oxidation pathway and therefore the overall corrosion rate. In nuclear power plant applications, an additional complication arises because of the presence of a continuous flux of ionizing radiation. When exposed to gamma-radiation, water decomposes, resulting in the production of a number of different redox active species, ranging from oxidizing ($\bullet OH$, H_2O_2, O_2) to reducing ($\bullet e_{aq}^-$, $\bullet H$, $\bullet O_2^-$) [4]–[7], as shown in reaction (1, [5]).

$$H_2O \rightsquigarrow OH^1, \bullet e_{aq}^-, \bullet H, H_2, H_2O_2, H^+ \quad (1)$$

The direct effect of gamma-radiation on the corrosion behaviours of pure nickel and nickel-based superalloys [8], [2], [9], Stellite-6 [10]–[12], and carbon and stainless steels has been studied [13]–[16]. Studies of the corrosion behaviour of Inconel X-750

[1] The reference indicated OH but I believe this to be a typo and that the correct form of this symbol should have been $\bullet OH$.

also exist in the literature [3], [17], [18]. Some of these studies were performed in simulated reactor conditions [17], [18]. However, there has been no study on the direct effect of gamma-radiation on the corrosion dynamics of Inconel X-750, to the best of my knowledge.

In Chapter 4, the elementary steps and the systemic feedback that occurs in the corrosion system were explained. The results discussed in previous Chapters (Chapters 4 and 5) were obtained in solutions of large volume (nearly 500 mL). In the current Chapter, the results from coupon exposure tests performed in a small solution volume (6.0 mL) will be discussed. Although there is no means to quantitatively measure the amounts of dissolved ions in the vicinity of the electrode's surface or the oxide/hydroxide layers (in the interfacial region), comparing the amounts of dissolved ions in the bulk solution under different conditions provides information on the systemic feedback between elementary steps and how the overall corrosion rate is controlled. This information could be used to more precisely determine the corrosion kinetics at the electrode surface under different solution conditions.

The amount of solution used in the coupon exposure tests in this Chapter was 6.0 mL, which is significantly smaller than the amount of solution used for the E_{corr} and CV experiments (Chapters 4 and 5). In addition, convective solution flow under stagnant conditions is negligible, and hence the rate of metal cation transport from the surface layer to the bulk solution will be further affected [8]. This is an important point for solutions under continuous argon purging condition with a continuous flow of argon gas in the E_{corr} and CV experiments, as opposed to stagnant solution in the coupon exposure tests. However, even in the absence of convective solution flow, the Brownian motion of molecules tends to homogenize the solution [19]. As a result, the dissolved metal cations (produced by metal oxidation half-reaction) will still transport from the interfacial region to the bulk solution.

The ratio of solution volume to surface area does not affect the rate of electron transfer [20]. Therefore, at the beginning (t = 0), when the solution is free of dissolved

metal cations, the rate of metal oxidation is independent of solution volume to surface area ratio. However, as corrosion progresses and the dissolved metal cations of interest ($M^{n+}_{(aq)|int}$) diffuse from the interfacial region to the bulk solution, a concentration gradient is established between the metal/solution and interfacial region/bulk solution interfaces. The transport of dissolved metal cations from the interfacial region to the bulk solution depends on the concentration gradient across the interfacial region [8]. In a smaller solution volume, the concentration of dissolved metal cations in the bulk solution increases faster for a given metal oxidation rate [8]. Because the rate of metal cation transport from the surface layer to the bulk solution depends on concentration gradient, this faster increase in the concentration of dissolved metal cations in the bulk solution decreases the rate of metal cation transport from the interfacial region to the bulk solution [8]. Therefore, the concentration of dissolved metal cations of an element in the interfacial region reaches its saturation limit faster. This results in the deposition of dissolved metal cations and switches the corrosion pathway to oxide/hydroxide formation [20].

6.2 Experimental Procedures

Information on the details of experimental procedures can be found in Chapter 3. In this Chapter, coupon exposure tests were performed to investigate the effect of a) gamma-radiation and pH at 25 °C and 150 °C, b) the effect of temperature (25 °C versus 80 °C) in the absence of gamma-radiation and low oxygen concentration and c) the effect of dissolved oxygen concentration at 80 °C in the absence of gamma-radiation, on the kinetics of oxide formation and metal dissolution of Inconel X-750. These investigations were carried out in borate buffer solutions for different exposure times.

For coupon exposure tests performed in argon-saturated conditions and in the absence of gamma-radiation (referred to as Ar-No-Rad) and in argon-saturated conditions and in the presence of gamma-radiation (referred to as Ar-Rad), the stock solution of interest was purged with argon gas prior to being transferred to the glove box. For coupon exposure tests performed in air-saturated conditions and in the absence of gamma-

radiation (referred to as air-No-Rad), a stock solution of interest under normal atmospheric conditions was used to submerge the coupons in the vials.

The coupon exposure tests were performed using Inconel X-750 coupons immersed in 6 mL solutions in sealed quartz vials. After the test duration, the solution was analyzed using ICP-OES to determine the concentrations of dissolved metal ions (i.e., Cr, Fe and Ni). When the difference between the dissolutions associated with two Ni wavelengths was larger than 7.2 times, only the dissolution associated with 231.604 nm wavelength was used. In the presented results, the concentration of each element is normalized to surface area (μM cm^{-2}). The morphologies of the coupons corroded at 150 °C (in both the absence and presence of gamma-radiation) were characterized by SEM. The SEM micrographs are shown at two different magnifications for each corroded coupon.

6.3 Results and Discussions

6.3.1 The effects of gamma-radiation and temperature on metal dissolution

In **Figure 6.1**, the ICP-OES results obtained from time-dependent coupon exposure experiments in the absence and presence of gamma-radiation at 25 °C are presented. This study was performed at two pHs: 10.6 and 6.0. The average values of dissolved ions for Cr, Fe and Ni were calculated from five samples (6, 12, 24, 48 and 96 hours) in the absence of gamma-radiation and from four samples (6, 12, 24 and 48 hours) in the presence of gamma-radiation.

Table 6.1 summarizes the effect of gamma-radiation on the average value of ion dissolution for all three main elements (i.e., Cr, Fe and Ni) at two pHs (i.e., pH 10.6 and pH 6.0). It was concluded that gamma-radiation decreased the average concentration of all three main elements (i.e., Cr, Fe and Ni) at pH 6.0. However, at pH 10.6, the effect of gamma-radiation on average ion dissolution depended on the element. More specifically, for Cr and Ni, gamma-radiation increased the average ion dissolution while for Fe, gamma-radiation decreased the average ion dissolution. Irrespective of the decrease or

increase in the average value of dissolution of an element, the amount of change was not significant, particularly when the gamma-radiation resulted in a lower average value of a dissolved ion concentration.

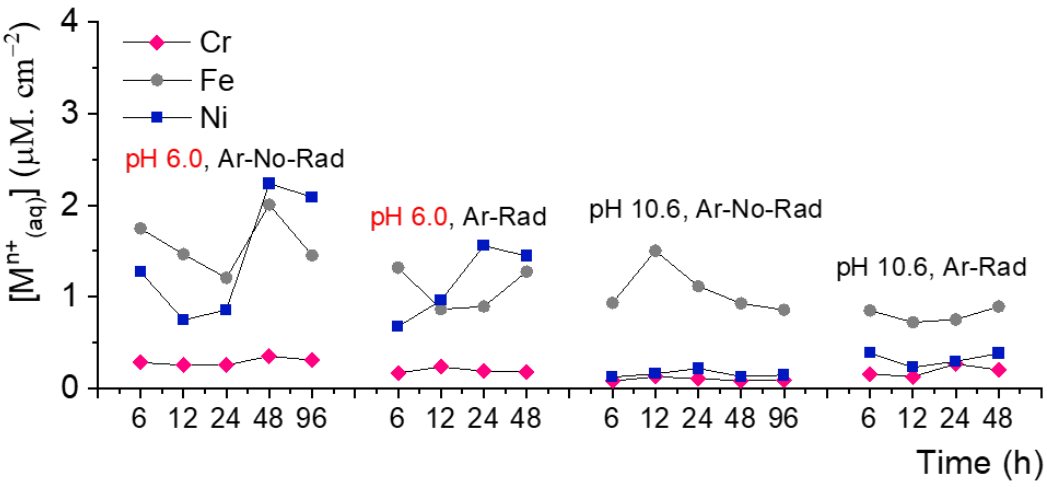

Figure 6.1 ICP-OES results from coupon exposure experiments in the absence and presence of gamma-radiation at 25 °C.

From the comparison of the ICP-OES results obtained at 25 °C, **Figure 6.1** and **Table 6.1**, it was understood that:

- Cr showed the least dissolution at all durations in the absence and presence of gamma-radiation at both pHs (i.e., pH 10.6 and pH 6.0).
- In all solution conditions, the amount of dissolved ion for each element reached a steady-state value at early times—except for Ni dissolution at pH 6.0 which showed an increasing behaviour over time.
- The steady-state condition for Cr, Fe and Ni continues at longer durations while each dissolved ion fluctuates around an average value over time.
- At pH 10.6, in both redox environments and at all durations: a) Fe was the dominant dissolved element and b) Ni dissolution was very low and comparable to Cr dissolution.

- Decreasing the solution pH from 10.6 to 6.0 had a significant effect on dissolution of Ni in both redox environments and at all durations. This difference was higher in the absence of gamma-radiation than in the presence of gamma-radiation.
- Although the average concentration of dissolved Fe was higher at pH 6.0 than at pH 10.6 (in both the presence and absence of gamma-radiation), this difference was not significant.

Table 6.1 The effect of gamma-radiation ($[M^{n+}]_{Ar-Rad}/[M^{n+}]_{Ar-No-Rad}$) at 25 °C on the average amounts (in mM cm^{-2}) of dissolved ions (Cr, Fe and Ni) at pH 10.6 and pH 6.0.

	Cr	Fe	Ni
pH 10.6, Ar-No-Rad	9.7×10^{-5}	1.1×10^{-3}	1.6×10^{-4}
pH 10.6, Ar-Rad	1.9×10^{-4}	8.0×10^{-4}	3.2×10^{-4}
[Ar-Rad]/[Ar-No-Rad]	1.9	0.8	2.1
	Cr	Fe	Ni
pH 6.0, Ar-No-Rad	2.9×10^{-4}	1.6×10^{-3}	1.4×10^{-3}
pH 6.0, Ar-Rad	1.9×10^{-4}	1.1×10^{-3}	1.2×10^{-3}
[Ar-Rad]/[Ar-No-Rad]	0.7	0.7	0.8

Figure 6.2 shows the effects of gamma-radiation and pH (i.e., pH 10.6, pH 6.0 and pH 8.4) on metal dissolution at 150 °C. For all pHs and solution redox environments (i.e., in the presence and absence of gamma-radiation), the average value of ion dissolution was calculated from three samples (1, 3 and 5 days). These average values are summarized in **Table 6.2**.

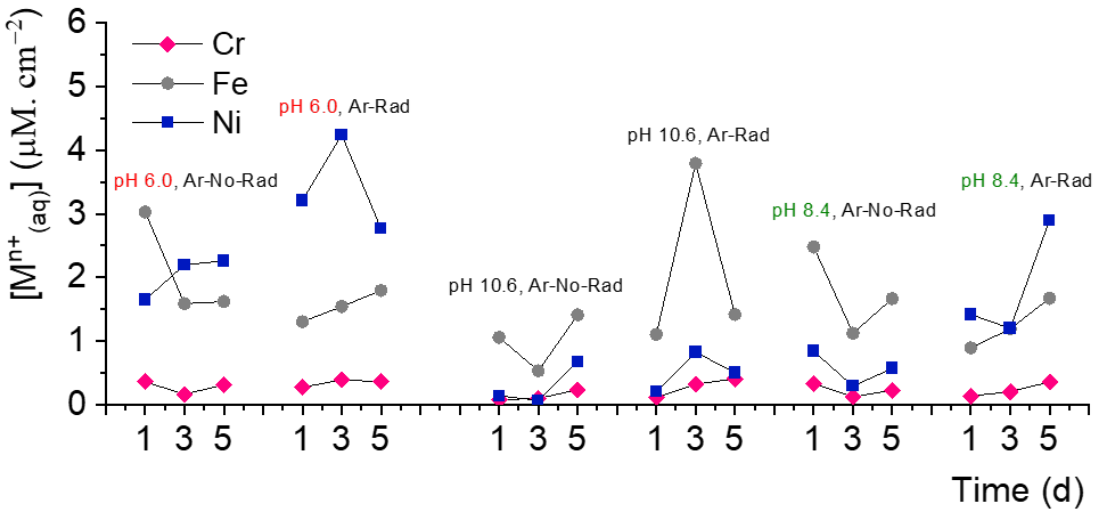

Figure 6.2 ICP-OES results from coupon exposure experiments: the effects of pH and gamma-radiation at 150 °C in the absence (Ar-No-Rad) and presence (Ar-Rad) of gamma-radiation.

From the comparison of the ICP-OES results obtained at 150 °C, as summarized in **Figure 6.2** and **Table 6.2**, it can be seen that:

- Irrespective of solution pH or gamma-radiation exposure, steady-state conditions are established for each of the three main dissolved elements (i.e., Cr, Fe and Ni) within 1 day. Under all conditions, the steady-state concentration fluctuates around an average value for each dissolved element. Irrespective of solution pH or gamma-radiation exposure, the average steady-state concentration of Cr was always the lowest—except at 3 days at pH 10.6 in the absence of gamma-radiation.

- At pH 10.6, the average amount of each dissolved ion in the presence of gamma-radiation was larger than the corresponding average value in the absence of gamma-radiation. The factor by which ion dissolution increased was nearly the same for all three main elements. In addition, irrespective of gamma-radiation exposure, Fe was the main dissolved element at all durations.
- At pH 6.0, the dissolution of Ni was significant irrespective of the presence of gamma-radiation. The average value of Ni dissolution was nearly the same as that of Fe in the absence of gamma-radiation. More specifically, there was a competition between Fe and Ni dissolution as the main dissolved element in the absence of gamma-radiation. On the other hand, in the presence of gamma-radiation, Ni became the main dissolved element at all durations. The factors by which Cr and Fe dissolution changed as a result of gamma-radiation exposure were close to 1 while this factor for Ni dissolution was slightly larger.
- At pH 8.4, Fe was the main dissolved element at all durations in the absence of gamma-radiation while Ni was the main dissolved element at all durations in the presence of gamma-radiation—except at 3 days for which the dissolutions of Fe and Ni were identical. The factors by which ion concentration changed as a result of gamma-radiation exposure were not significant for Cr and Fe. More specifically, the changes in Cr and Fe dissolution as a result of gamma-radiation exposure were close to 1 while this factor Ni dissolution was larger and close to 3.

Table 6.2 The effect of gamma-radiation ($[M^{n+}]_{Ar-Rad}/[M^{n+}]_{Ar-No-Rad}$) at 150 °C on the average amounts (in mM cm^{-2}) of dissolved ions (Cr, Fe and Ni) at pH 10.6, pH 6.0 and pH 8.4.

	Cr	Fe	Ni
pH 10.6, Ar-No-Rad	1.4×10^{-4}	1.0×10^{-3}	2.9×10^{-4}
pH 10.6, Ar-Rad	2.8×10^{-4}	2.1×10^{-3}	5.1×10^{-4}
[Ar-Rad]/[Ar-No-Rad]	2.1	2.1	1.7
	Cr	Fe	Ni
pH 6.0, Ar-No-Rad	2.8×10^{-4}	2.1×10^{-3}	2.0×10^{-3}
pH 6.0, Ar-Rad	3.4×10^{-4}	1.5×10^{-3}	3.4×10^{-3}
[Ar-Rad]/[Ar-No-Rad]	1.2	0.7	1.7
	Cr	Fe	Ni
pH 8.4, Ar-No-Rad	2.3×10^{-4}	1.8×10^{-3}	5.7×10^{-4}
pH 8.4, Ar-Rad	2.3×10^{-4}	1.3×10^{-3}	1.8×10^{-3}
[Ar-Rad]/[Ar-No-Rad]	1.0	0.7	3.2

6.3.2 The effects of temperature and oxygen concentration on metal dissolution

In this section, the effect of temperature (25 °C versus 80 °C) in argon-saturated conditions and in the absence of gamma-radiation, and the effect of dissolved oxygen concentration at 80 °C (air-saturated conditions versus argon-saturated conditions) in the absence of gamma-radiation on the dissolution of three main elements (i.e., Cr, Fe and Ni) are discussed. These results are presented in **Figure 6.3**. The average concentrations of Cr, Fe and Ni were calculated from five samples (6, 12, 24, 48 and 96 hours) in argon-saturated conditions at 25 °C and air-saturated conditions at 80 °C while the average value of each dissolved ion (i.e., Cr, Fe and Ni) in argon-saturated conditions at 80 °C was calculated from eight samples (0.5, 1, 3, 6, 12, 24, 48, and 96 hours). These average values are summarized in **Table 6.3**.

From the comparison of the ICP-OES results in **Figure 6.3** and **Table 6.3** it was understood that:

- The Cr concentration was the lowest of the three elements under all solution conditions, regardless of solution pH, temperature, and dissolved oxygen concentration.
- Under all solution conditions, the amount of dissolved ion for each element reached a steady-state value at early times and then continued to fluctuate around an average value—except for Ni at pH 6.0 which showed an ever-increasing trend at longer durations. This effect was most pronounced at 80 °C and in argon-saturated conditions.
- At pH 10.6, Fe was the dominant dissolved element. In addition, Ni dissolution was very low and comparable to Cr dissolution. These effects were independent of temperature and dissolved oxygen concentration.
- At pH 6.0, Ni was the dominant dissolved element under all conditions except for early times at 25 °C in argon-saturated conditions.

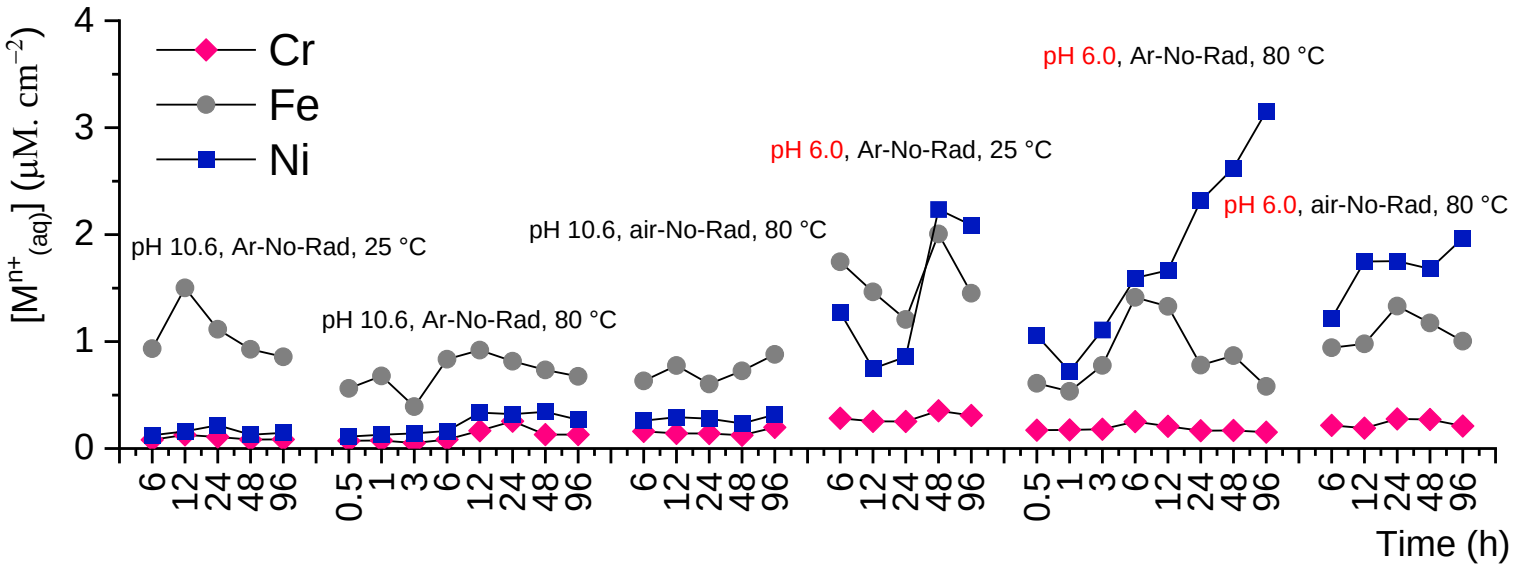

Figure 6.3 ICP-OES results from coupon exposure experiments, the effect of temperature in argon-saturated conditions and the effect of oxygen concentration at 80 °C.

Table 6.3 The effect of temperature and oxygen concentration on the average amounts (in mM cm^{-2}) of dissolved ions (Cr, Fe and Ni) at pH 10.6 and pH 6.0.

	Cr	Fe	Ni
pH 10.6, Ar-No-Rad 25 °C	9.7×10^{-5}	1.1×10^{-3}	1.6×10^{-4}
pH 10.6, Ar-No-Rad 80 °C	1.2×10^{-4}	7.0×10^{-4}	2.3×10^{-4}
pH 10.6, air-No-Rad 80 °C	1.5×10^{-4}	7.2×10^{-4}	2.8×10^{-4}
[Ar-No-Rad 80 °C]/[Ar-No-Rad 25 °C]	1.2	0.7	1.5
[air-No-Rad 80 °C]/[Ar-No-Rad 80 °C]	1.3	1.0	1.2
	Cr	Fe	Ni
pH 6.0, Ar-No-Rad 25 °C	2.9×10^{-4}	1.6×10^{-3}	1.4×10^{-3}
pH 6.0, Ar-No-Rad 80 °C	1.8×10^{-4}	8.6×10^{-4}	1.8×10^{-3}
pH 6.0, air-No-Rad 80 °C	2.3×10^{-4}	1.1×10^{-3}	1.7×10^{-3}
[Ar-No-Rad 80 °C]/[Ar-No-Rad 25 °C]	0.6	0.5	1.2
[air-No-Rad 80 °C]/[Ar-No-Rad 80 °C]	1.3	1.3	0.9

6.3.3 The effect of gamma-radiation on the morphology of corroded coupons at 150 °C

The SEM micrographs of corroded coupons at 150 °C after 1 and 5 days in the presence and absence of gamma-radiation are presented in **Figure 6.4** (at pH 10.6), **Figure 6.5** (at pH 6.0) and **Figure 6.6** (pH 8.4). These SEM images do not necessarily correspond to the ICP-OES results in **Figure 6.2**. The SEM micrographs of as-polished Inconel X-750 is shown in **Figure 6.7**. These SEM images were obtained in secondary electron (SE) mode. Irrespective of solution pH or gamma-radiation exposure, the surface film consisted of an underlying film in the form of either a compact or a filament-like oxide, covered with a sparse distribution of particle oxides. In some of the micrographs shown in **Figure 6.4** to **Figure 6.6**, the yellow lines indicate features that are likely polishing lines covered by the underlying film. These features which hereafter are referred to as polishing lines, are also observable and indicated by yellow lines in **Figure 6.7**. From **Figure 6.4** to **Figure 6.6** it can be seen that:

- At pH 10.6, the underlying oxide resembled a compact film (particularly in 1d specimens) more than a filament-like oxide—except in 5d specimens where some filament-like oxide was observed. This underlying film converted to a filament-like oxide to some extent over time (from 1 to 5 days) in the presence and absence of gamma-radiation. A polishing line was visible in the image of the 1d specimen corroded in the absence of gamma-radiation, while no polishing lines were observed for its counterpart in the presence of gamma-radiation. After 5 days, the density of oxide particles was higher than for 1d specimen, irrespective of gamma-radiation exposure or its absence. In 5d specimens, the density of oxide particles was higher in the absence of gamma-radiation than in the presence of gamma-radiation. In addition, polishing lines were observed in 5d specimen in both the absence and presence of gamma-radiation.
- For pH 6.0, an underlying oxide covered with oxide particles was observable for all conditions. After 1 day, there was no major difference

between the specimens corroded in the absence and presence of gamma-radiation in terms of the underlying oxide and oxide particles—except for the polishing lines which were visible in the absence of gamma-radiation, and a slightly more developed underlying oxide in the presence of gamma-radiation (more specifically, no polishing lines were seen in the 1d specimen in the presence of gamma-radiation). Even in 1d specimen in the absence of gamma-radiation, the underlying oxide resembled a filament-like film more than a compact film. After 5 days, the underlying oxide developed to a greater extent and became visible in both the absence and presence of gamma-radiation. In other words, the filament-like oxide developed over time in both the absence and presence of gamma-radiation. After 5 days, the filament-like structure was finer and had a more open structure in the presence of gamma-radiation than in the absence of gamma-radiation. In the presence of gamma-radiation, the density of oxide particles was higher for 1d specimen than for 5d specimen while in the absence of gamma-radiation there was no major difference in the density of oxide particles between the 1d and 5d specimens. For the 5d specimens, no polishing lines was observed in either the presence or absence of gamma-radiation.

- For pH 8.4, the underlying oxide in all conditions resembled a filament-like film more than a compact film. After 1 day, there was no difference between the specimens corroded in the absence and presence of gamma-radiation in terms of the underlying oxide and oxide particles—except for a slightly higher oxide particle density in the absence of gamma-radiation. In addition, there were no polishing lines visible on the sample corroded in the presence of gamma-radiation while a polishing line was visible on the sample corroded in the absence of gamma-radiation. After 5 days, the underlying filament-like film developed in the presence of gamma-radiation while in the absence of gamma-radiation the underlying filament-like film became finer. After 5 days, this filament-like underlying film had a finer structure in the absence of gamma-radiation while in the presence

of gamma-radiation, it had a coarser structure. For the 5d specimen corroded in the absence of gamma-radiation, a trace of a polishing line was visible unlike for its counterpart in the presence of gamma-radiation for which no polishing line was visible.

The morphologies of corroded Inconel 600, Stellite-6 and pure nickel at 150 °C have been studied in the literature and a filament-like oxide was observed on these alloys in the absence and presence of gamma-radiation [9], [12], [8]. The lengths of the filaments and the depth of the coverage depend on pH and gamma-radiation [9]. These filament-like oxides form as a result of hydroxide dehydration [8].

The surface of nickel-based superalloys with at least 15 wt.% Cr (e.g., Inconel 600 and Alloy 800) is covered with a thin layer of Cr_2O_3 oxide due to the thermodynamic stability of Cr_2O_3 [2], [9]. Inconel X-750 is a nickel-based superalloy similar to Inconel 600—with the distinction that it is precipitation hardenable due to the addition of aluminum and titanium [21], [22]. Inconel X-750 that has more than 15 wt.% Cr (which is sufficient for the establishment of a thin layer of air-formed Cr_2O_3 oxide) is likely covered by a thin layer of Cr_2O_3 oxide on its surface prior to the beginning of aqueous corrosion. In addition, the oxide that grows on Alloy 800 has been reported to have a spinel structure with a composition $Ni_xFe_{1+x}Cr_{2-x}O_4$ (0<x<1) where x = 0 near the metal/oxide interface and x = 1 near the oxide/solution interface [2]. Although Inconel X-750 has different concentrations of the three main elements (i.e., Cr, Fe and Ni) from Alloy 800, it is likely that the oxide film that grows on Inconel X-750 will be a non-stoichiometric mixed oxide of these three main elements.

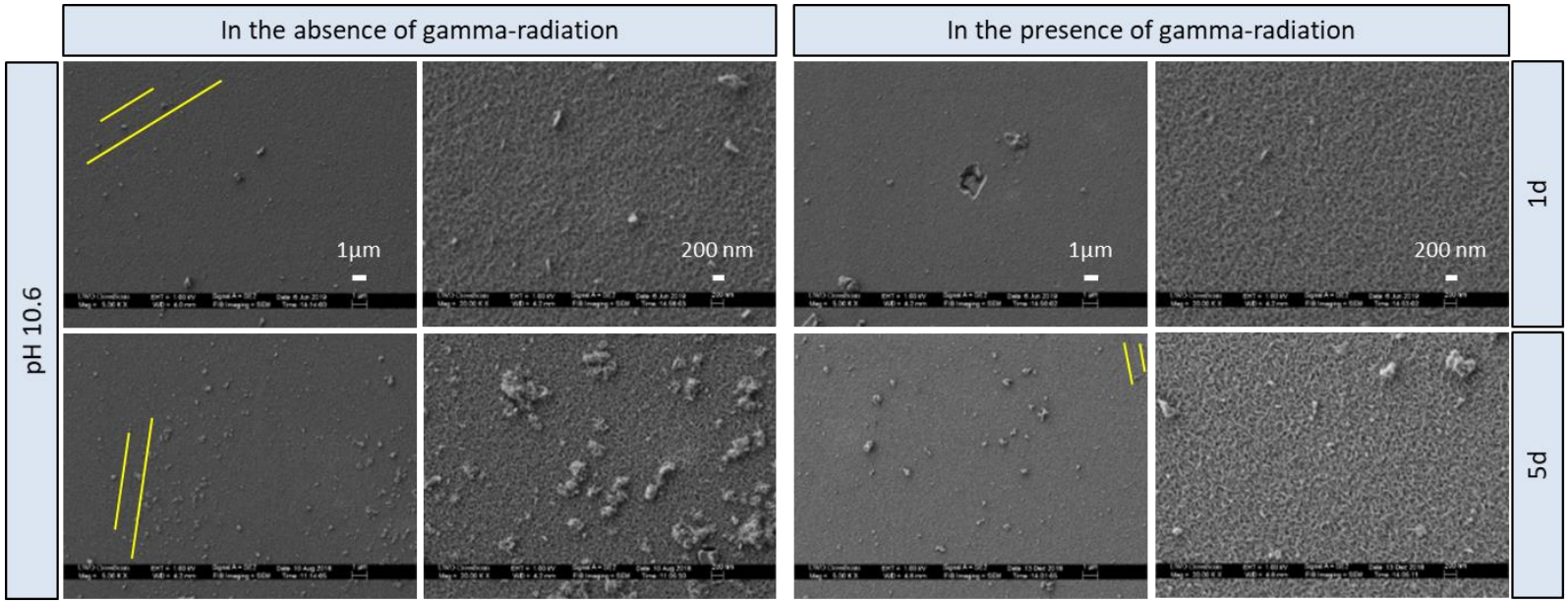

Figure 6.4 SEM micrographs of corroded coupons at 150 °C after 1 and 5 days in the presence and absence of gamma-radiation at pH 10.6.

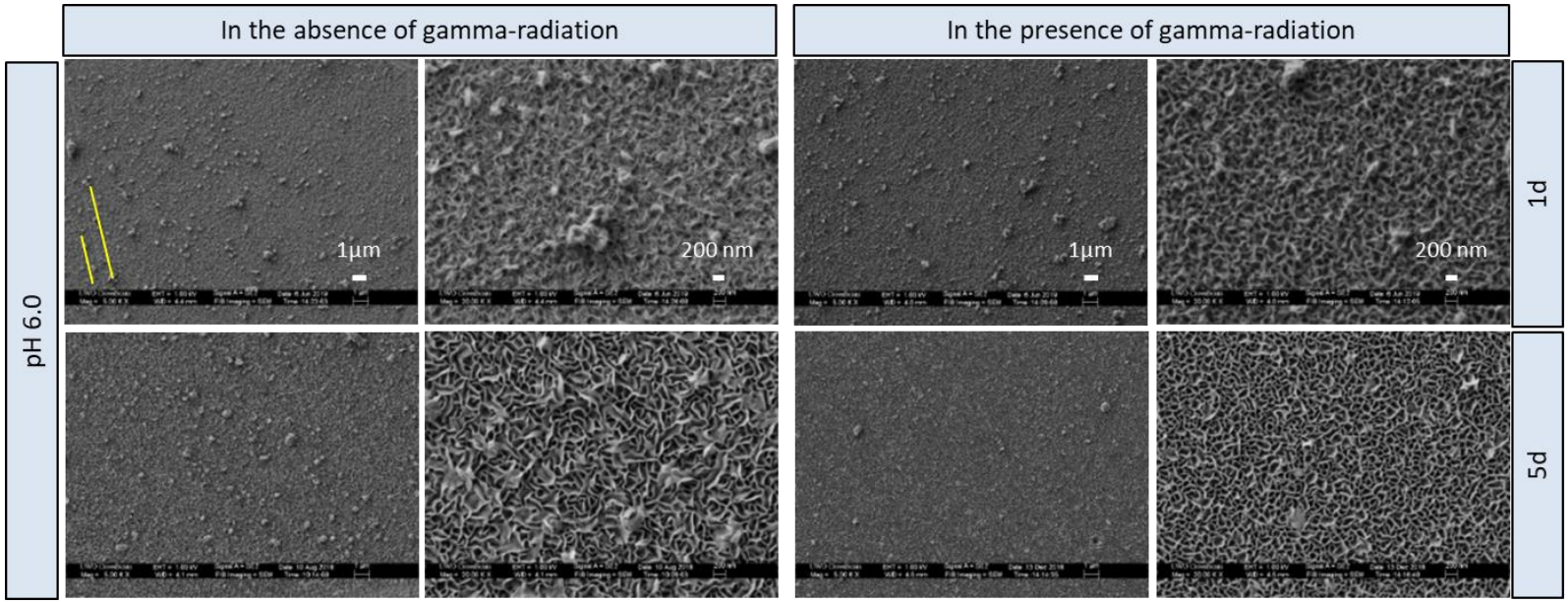

Figure 6.5 SEM micrographs of corroded coupons at 150 °C after 1 and 5 days in the presence and absence of gamma-radiation at pH 6.0.

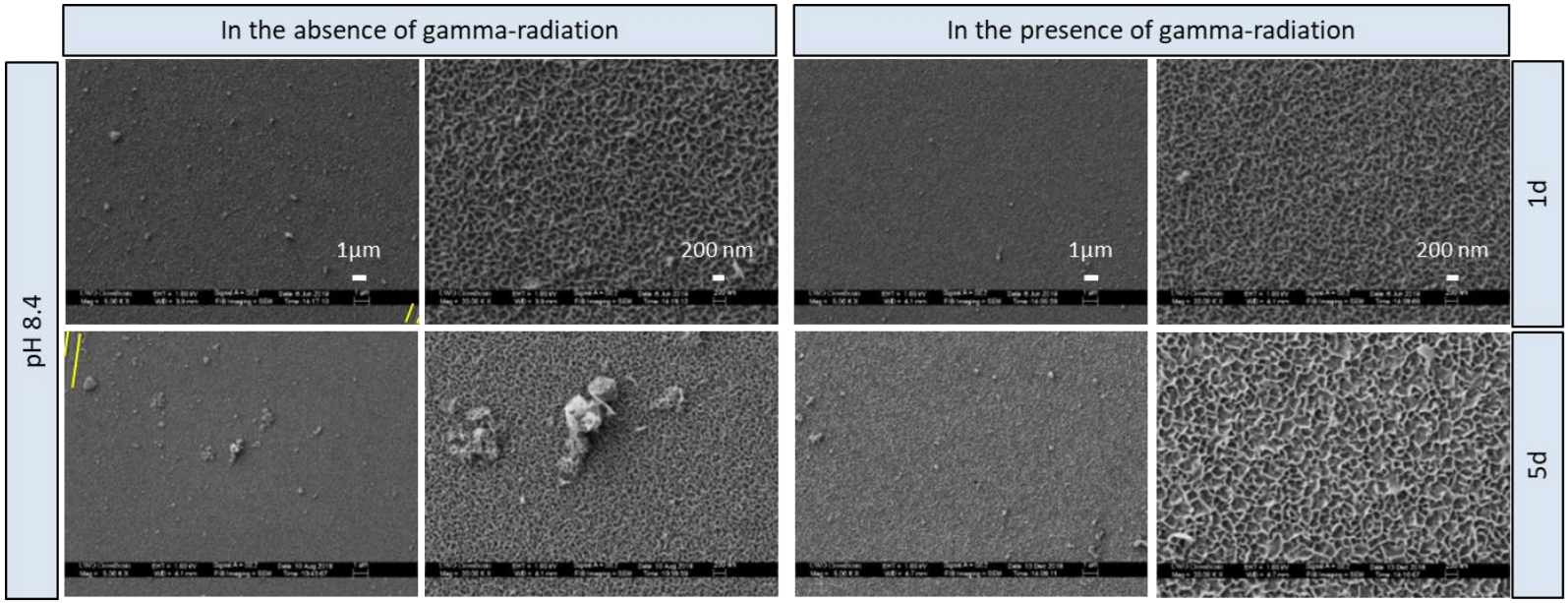

Figure 6.6 SEM micrographs of corroded coupons at 150 °C after 1 and 5 days in the presence and absence of gamma-radiation at pH 8.4.

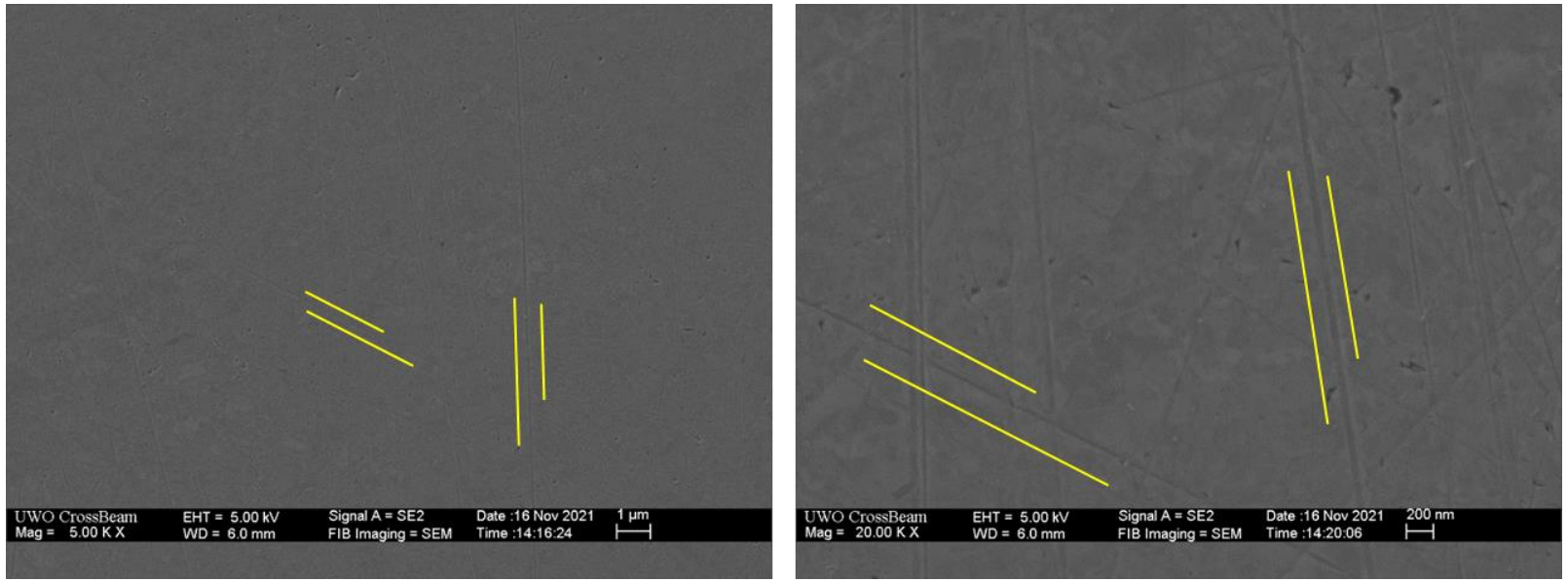

Figure 6.7 SEM micrographs of as-polished Inconel X-750 at two magnifications.

The solubility limit of Cr_2O_3 is lower than the solubility limits of $Fe(OH)_2$ and $Ni(OH)_2$ for the range of pHs studied in this work [23], [24]. In addition, it has been observed that the concentration of dissolved Cr in equilibrium with $Cr_xFe_{1-x}(OH)_3$ was several orders of magnitude lower than when in equilibrium with $Cr(OH)_3$ [25].

As mentioned in Chapter 4, under a naturally corroding conditions, the overpotential for a redox half-reaction is defined by $\left|\eta_{rxn}\right| = \left|E_{corr} - E_{rxn}^{eq}\right|$ and the overpotential for a metal oxidation half-reaction is $\left|\eta_{ox}\right| = \left|E_{corr} - E_{ox}^{eq}\right|$). $E^{eq}_{Cr^0 \rightleftharpoons Cr_2O_3}$ is significantly less positive (less noble) than the equilibrium potentials of $Fe^0 \rightleftharpoons Fe^{II}$ (e.g., $E^{eq}_{Fe^0 \rightleftharpoons FeCr_2O_4}$) and $Ni^0 \rightleftharpoons Ni^{II}$ (e.g., $E^{eq}_{Ni^0 \rightleftharpoons \beta - Ni(OH)_2}$) half-reactions—see **Appendix B**. Therefore, for given solution redox conditions and at early times when dissolved metal cations are not present in the interfacial region, the overpotential for Cr oxidation is larger than those of the Fe and Ni oxidation half-reactions. As a result, the interfacial region quickly saturates with dissolved Cr^{III} ions. The solubility limit of Cr_2O_3 at pH 6.0 is very low and nearly one order of magnitude lower than at pH 10.6 [24]. The fast saturation of the interfacial region with dissolved $Cr^{3+}_{(aq)|int}$ ions is followed by a hydrolysis reaction which results in the establishment of a Cr_2O_3 film—even at pH 6.0 where the concentration of OH^- is lower than at pH 10.6. Therefore, an insoluble Cr_2O_3 film quickly forms on the surface at both pH 10.6 and pH 6.0. This is consistent with the observation that in all the solution environments discussed above, the average value of dissolved Cr for a given solution condition was always lower than that of dissolved Fe and Ni.

Once the Cr_2O_3 film forms on the surface, further oxidation of $Cr^0_{(m)|int}$ to $Cr^{3+}_{(aq)|int}$ is slowed down. Formation of this Cr_2O_3 film can also limit the oxidation of Fe and Ni (for given redox conditions). This is because the rate of interfacial charge transfer can be limited by the rate of solvation (or surface hydration) of metal cations [9].

Prior to the saturation of the interfacial region with dissolved Fe and Ni, the main path for the corrosion is metal oxidation. The equilibrium potential of $Fe^0 \rightleftharpoons Fe^{II}$ (e.g.,

$E^{eq}_{Fe^0 \rightleftharpoons FeCr_2O_4}$ or $E^{eq}_{Fe^0 \rightleftharpoons Fe(OH)_2}$) is less positive (less noble) than the equilibrium potential of $Ni^0 \rightleftharpoons Ni^{II}$ (e.g., $E^{eq}_{Ni^0 \rightleftharpoons \beta - Ni(OH)_2}$), see **Appendix B**. Therefore, for given redox conditions, the overpotential for Fe oxidation is larger than that of Ni. In addition, the solubility limits of Ni^{II} and Fe^{II} are different for a given solution pH. More specifically, the solubility limit of Fe^{II} is nearly one order of magnitude larger than Ni^{II} at both pH 10.6 and pH 6.0 [23]. The rate of dissolved metal cation transport from the interfacial region to the bulk solution depends on the concentration gradient of dissolved metal cations across the interfacial region [8]. Therefore, prior to the saturation of the interfacial region with dissolved metal cations (i.e., $Fe^{II}_{(aq)}$and $Ni^{II}_{(aq)}$), a relatively lower dissolution of Ni^{II} species than that of Fe^{II} species is expected.

The solubility limits defined for Fe^{II} and Ni^{II} in the form of a mixed hydrogel network can be different from the solubility limits of Fe^{II} and Ni^{II} defined for pure $Fe(OH)_2$ and $Ni(OH)_2$ oxides/hydroxides. **Table 6.4** summarizes the effect of solution pH on Fe and Ni dissolution for Inconel X-750. Interestingly, in all solution conditions, the average concentration of Ni dissolution largely depended on the solution pH and not on temperature or redox environment, while the average concentrations of dissolved Fe or Cr did not change significantly with pH. The solubility limits of both $Fe(OH)_2$ and $Ni(OH)_2$ decrease by nearly seven orders of magnitude upon decreasing the solution pH from 10.6 to 6.0 [23]. However, **Table 6.4** showed that decreasing the solution pH from 10.6 to 6.0 had a more significant effect on Ni dissolution than on Fe or Cr dissolution. This indicates that the order of change in solubility limits of Fe^{II} and Ni^{II} with pH in the presence of a mixed hydrogel network (such as the one that forms on the surface of Inconel X-750) can be different from that for pure metal hydroxides. As a result, prior to the saturation of the interfacial region with dissolved metal cations (i.e., $Fe^{II}_{(aq)}$ and $Ni^{II}_{(aq)}$), the relative dissolutions of Ni^{II} and Fe^{II} species for Inconel X-750 which is likely covered by a Cr_2O_3 film does not linearly change with solution pH.

In conditions where the rate of metal oxidation is fast and the rate of metal cation transport from the interfacial region to the bulk solution is slow [26], the interfacial

region becomes saturated with dissolved metal cations. This shifts the hydrolysis equilibrium towards the precipitation of metal oxides/hydroxides. The hydroxides of transition metals are hygroscopic and form a hydrogel network after precipitating as colloidal particles [27], [8], [28].

At pH 10.6 and 150 °C, the polishing lines were visible for all specimens irrespective of the duration of corrosion or the presence of gamma-radiation—except for the 1d specimen in the presence of gamma-radiation. The visibility of these polishing lines can indicate the thinness of the underlying oxide [8]. The results in **Figure 6.2** and **Table 6.2** showed that gamma-radiation or exposure time did not have a significant effect on the average values of each dissolved element (i.e., Cr, Fe and Ni). The solution environment under gamma-radiation becomes more oxidizing due to the production of H_2O_2, which acts as the main oxidant and consequently increases the metal oxidation rate initially [8], [9]. This translates to a larger overpotential for metal oxidation in the presence of gamma-radiation than in the absence of gamma-radiation. In addition, H^+ is another water radiolysis product which is continuously produced under a continuous flux of gamma-radiation [8] and can decrease the solution pH and consequently increase the solubility limits of dissolved metal cations (e.g., Fe^{II} and Ni^{II}).

Table 6.4 The effect of pH ($[M^{n+}]_{pH\ 6.0}/[M^{n+}]_{pH\ 10.6}$) on the average concentrations of Cr, Fe and Ni under different redox conditions.

Condition	Ar-No-Rad 25 ℃	Ar-Rad 25 ℃	Ar-No-Rad 150 ℃	Ar-Rad 150 ℃	Ar-No-Rad 80 ℃	air-No-Rad 80 ℃
Cr	3.0	1.0	2.0	1.2	1.5	1.5
Fe	1.5	1.4	2.1	0.7	1.2	1.5
Ni	9.3	3.6	6.9	6.6	7.8	6.0

The fact that at pH 10.6 the dissolved ion concentrations reached steady-state values and did not change considerably with time or gamma-radiation exposure is consistent with the nearly unchanged morphology of the corroded specimens over time or in the presence of gamma-radiation exposure—more specifically, the underlying film developed only to a small extent to a filament-like film between 1 and 5 days. At pH 10.6, the solubility limits of all three main elements (i.e., Cr, Fe and Ni) are low. In addition, the concentration of OH^- is high. This forces the corrosion pathway towards oxide formation rather than metal dissolution and results in fast saturation of the interfacial region and early formation of a hydrogel network. The deposition of corrosion products on the surface, which results in the formation and growth of the hydrogel network, impedes the transport of dissolved metal cations from the corroding substrate [28], [29]. Although the rate of metal oxidation decreases with oxide growth, the deposited metal oxide/hydroxide (i.e., the hydrogel network) grows as long as metal oxidation continues [2]. This explains the negligible effect of gamma-radiation on the dissolved metal cation concentration or the morphology of the corroded surfaces at pH 10.6.

As can be seen in **Table 6.4**, the main effect of decreasing the solution pH was on the dissolution of Ni. That is, decreasing the solution pH from 10.6 to 6.0 had a less significant effect on increasing the dissolutions of Cr and Fe than on increasing the dissolution of Ni. The ICP-OES results at 150 °C showed that at both pH 10.6 and pH 6.0, the concentration of dissolved elements (i.e., Cr, Fe and Ni) reached a steady-state values after 1 day. On the other hand, from the SEM micrographs in **Figure 6.4** and **Figure 6.5**, it can be seen that decreasing the solution pH from 10.6 to 6.0, changed the morphology of the underlying oxide from a compact film to a filament-like oxide. In addition, at pH 6.0, the polishing lines were mostly absent on all specimens (except for the 1d specimen in the absence of gamma-radiation), whereas at pH 10.6, the polishing lines were visible for all specimens (except for the 1d specimen in the presence of gamma-radiation). As mentioned above, the visibility of these polishing lines can indicate the thinness of underlying oxide [8]. That is to say, a thicker underlying film can form at a lower solution pH (i.e., at pH 6.0 relative to at pH 10.6).

The solubility of dissolved metal cation depends on temperature [9]. However, the effect of temperature on changing the solubility of dissolved metal cations is relatively small than that of solution pH [9].

Although the rate of surface hydration reaction decreases with decreasing the solution pH from 10.6 to 6.0, the rate of this reaction increases with the solution temperature [2]. The temperature at which these experiments were carried out was high (i.e., 150 °C). Therefore, even at pH 6.0 where the concentration of OH^- is lower than at pH 10.6, the surface hydration is fast which results in the transfer of oxidized metal cations from the metallic site to the interfacial region.

The net dissolution of Ni^{II} is initially higher at pH 6.0 than at pH 10.6 [2]. The high dissolution of Ni^{II} at pH 6.0 at early times (when the interfacial region is not yet saturated with dissolved Ni species) results in a larger concentration gradient between the metal/solution interface and interfacial region/bulk solution interface. The rate of transport of dissolved metal cations is proportional to the concentration gradient across the interfacial region and increases when the concentration gradient is larger [8].

However, it should be noted that the coupon exposure tests were performed in a small solution volume. At longer times, when the bulk solution contains more dissolved metal cations (e.g., Ni^{II}), the rate of metal cation transport from the interfacial region to the bulk solution decreases. This is because the rate of metal cation transport from the interfacial region to the bulk solution depends on the concentration gradient [8].

The combined effect of small solution volume and a fast surface hydration reaction result in fast saturation of the interfacial region with dissolved metal cations and consequently precipitation of dissolved metal cations (e.g., Ni^{II}) in the interfacial region. The shortest duration of coupon exposure test in this study was 1 day. As can be seen from **Figure 6.2**, the average concentrations of dissolved Ni species reached a steady-state in 1 day. This indicates that in at longer times (after 1 day), the concentration of dissolved metal cations (e.g., Ni^{II}) in the bulk solution is high. This results in

deceleration of further transport of dissolved metal cations (e.g., Ni^{II}) from the interfacial region to the bulk solution. When the interfacial region reaches the solubility limit of dissolved metal cations, the yield of hydrolysis reaction for dissolved metal cations (e.g., Ni^{II}) in the interfacial region increases resulting in the precipitation of metal oxides/hydroxides particles. This is consistent with the observation of more dissolved Ni^{II} ions and a most-likely thicker deposited film at pH 6.0 than at pH 10.6 at 150 °C in a small solution volume.

At all pHs (i.e., pH 10.6, pH 6.0 and pH 8.4), once the hydrogel network forms, the dissolved metal cations (e.g., $Fe^{2+}_{(aq)|int}$ or $Ni^{2+}_{(aq)|int}$) can oxidize to a higher oxidation state (e.g., $Fe^{3+}_{(aq)|int}$ or $Ni^{3+}_{(aq)|int}$). This reaction requires a much stronger oxidant than water (or H^+) [20] and is therefore more likely in the presence of gamma-radiation due to the continuous production of H_2O_2, which acts as the main oxidant [8], [9].

The hydrogel network can dehydrate and convert into solid crystal oxides at high temperatures. The growth of a metal oxide into a distinct crystal phase is highly temperature-sensitive due to the high activation energy required for lattice bond formation [9], [20]. In the presence of a grown solid oxide lattice, the overall metal oxidation is generally suppressed [8].

The results obtained at lower temperatures and in the absence of gamma-radiation, shown in **Table 6.3**, indicated that at both solution pHs (i.e., pH 10.6 and pH 6.0) increasing the solution temperature (from 25 °C to 80 °C) or increasing the concentration of dissolved oxygen (from argon-saturated to air-saturated) did not have a significant effect on increasing the average concentrations of each dissolved element (i.e., Cr, Fe and Ni). In addition, the results in **Table 6.1** indicated that the effect of gamma-radiation on increasing the average concentrations of three main elements (i.e., Cr, Fe and Ni) was also not significant.

At pH 10.6, the solubility limits of all three main elements are low and the concentration of OH^- is high, which results in a fast hydration of oxidized metal atoms and the hydrolysis of dissolved metal cations, early precipitation of metal oxides/hydroxides and the formation of a hydrogel network. Further metal oxidation is slowed down in the presence of a hydrogel network due to slow transport of dissolved metal cations from the corroding surface to the interfacial region and eventually to the bulk solution [28], [29]. This is consistent with the observations in **Figure 6.1** and **Figure 6.3** which showed that the concentrations of each element (i.e., Cr, Fe and Ni) fluctuated around an average value and did not change significantly with redox environment or temperature.

At pH 6.0, the solubility limits of Cr and Fe species are not much different from those at pH 10.6. This is consistent with the observation of steady-state conditions for the dissolution of these elements in all redox environments and temperatures in **Figure 6.1** and **Figure 6.3**. However, it can be seen from **Table 6.4** that the main effect of decreasing the solution pH from 10.6 to 6.0 was on increasing the concentration of dissolved Ni species. This is also consistent with the observation of an increasing trend for Ni dissolution over time at pH 6.0, irrespective of redox environment or temperature (at temperatures below 80 °C). At pH 6.0, the rates of surface hydration reaction and solid crystal oxide formation at temperatures up to 80 °C are not as fast as those at 150 °C. This results in the transport of dissolved metal cations (e.g., Ni^{II}) form the interfacial region to the bulk solution over a longer period of time at 80 °C (in the absence of gamma-radiation, **Figure 6.3**) than at 150 °C (in the absence of gamma-radiation, **Figure 6.2**).

The results in this Chapter support the findings from previous Chapters, particularly for later stages where the hydrogel network has developed on the surface and can convert into solid crystal oxides.

It was found that at early times, a Cr_2O_3 film quickly forms at all pHs (for the range of pHs studied in this work) and can limit the oxidation of Fe and Ni at a given pH.

At early times, in stage 1, the concentrations of dissolved metal cations (Fe^{II} and Ni^{II}) remain below their saturation limits. The rate of metal oxidation is equal to the rate of oxidant reduction. In more oxidizing redox conditions, the rate of metal oxidation is higher than under less oxidizing redox conditions. However, the rate of metal oxidation under any redox conditions has to be equal to the rate of oxidant reduction. In more oxidizing redox conditions such as in the presence of gamma-radiation, the rate of metal oxidation (or the overall rate of corrosion) is initially increased due to the generation of H_2O_2, which acts as the main oxidant [8], [9].

The dissolved metal cations transport from the interfacial region to the bulk solution due to the concentration gradient between these two regions. At lower pHs (e.g., pH 6.0) where the solubility limits of metal cations (mainly Ni^{II}) are high, a larger concentration gradient is initially established between the interfacial region and the bulk solution which increases the rate of transport of metal cations to the bulk solution [8]. However, for small solution volumes, further transport of dissolved metal cations from the interfacial region to the bulk solution is decelerated as the concentration of dissolved metal cations (e.g., Ni^{II}) in the bulk solution increases [8]. This results in early saturation of the interfacial region for small solution volumes.

In stage 2, the concentration of dissolved metal cations in the interfacial region increases and reaches the saturation limit. The dissolved metal cations undergo hydrolysis and the hydrolysis equilibrium shifts towards the precipitation of metal hydroxide and the establishment of a hydrogel network. For Inconel X-750, this hydrogel network is likely a mixture of metal cations with different oxidation states. Although the reactions involved in stage 1 continue in stage 2, the formation of a hydrogel network slows down the overall rate of metal oxidation.

Once the hydrogel network forms, the dissolved metal cations and the metal hydroxide (e.g., $Fe^{2+}/Fe(OH)_2$ or $Ni^{2+}/Ni(OH)_2$) in the interfacial region can oxidize to a higher oxidation state. The oxidation of interfacial metal cations and the metal hydroxide depends on the redox conditions (i.e., the concentration and the type of

oxidant). In less oxidizing conditions, further oxidation of interfacial metal cations and the metal hydroxide to higher oxidation states is less likely, while in more oxidizing conditions such as those under gamma-radiation, the hydrogel network can oxidize to higher oxidation states and convert into a mixture of the three main elements with different oxidation states.

In stage 3, the formation of solid crystal oxides from the hydrogel network can occur, particularly at higher temperatures. The formation of solid crystal oxides further limits metal oxidation.

6.4 Conclusions

In this Chapter, the effect of redox environment, pH and temperature on the corrosion behaviour of Inconel X-750 was studied using coupon exposure tests. The dissolution of the three main elements of this alloy (i.e., Cr, Fe and Ni) was investigated using the ICP-OES technique, and the surface morphologies of specimens corroded at 150 °C was studied using the SEM technique. At early times, a Cr_2O_3 film quickly forms at all the pHs (for the range of pH studied in this work) due to the low solubility limit of Cr^{III} and the larger oxidation overpotential available for Cr oxidation than for Fe and Ni. This was consistent with the fact that the average concentration of dissolved Cr was lower than for both Fe and Ni under all studied conditions.

It was concluded that under all conditions, decreasing the solution pH significantly increased the average concentration of dissolved Ni while the average concentrations of dissolved Fe and Cr did not changed significantly. This further supported the findings from previous Chapters. It was also concluded that changing the solution pH could have less effect on the solubility limits of Fe^{II} and Cr^{III} in the presence of a mixed hydrogel (such as the one that forms on the surface of Inconel X-750) than it could have on the solubility limits of pure metal oxides/hydroxides, (e.g., $Fe(OH)_{2\,(s)}$ and Cr_2O_3).

6.5 References

[1] H. K. Zhang, Z. Yao, G. Morin, and M. Griffiths, “TEM characterization of in-reactor neutron irradiated CANDU spacer material Inconel X-750,” *Journal of Nuclear Materials*, vol. 451, no. 1, pp. 88–96, Aug. 2014, doi: 10.1016/j.jnucmat.2014.03.043.

[2] M. Momeni, “Gamma-Radiation Induced Corrosion of Alloy 800,” The University of Western Ontario, 2017. Electronic Thesis and Dissertation Repository, Available: https://ir.lib.uwo.ca/etd/5011

[3] T. Kekkonen and H. Hänninen, “The effect of heat treatment on the microstructure and corrosion resistance of inconel X-750 alloy,” *Corrosion Science*, vol. 25, no. 8, pp. 789–803, Jan. 1985, doi: 10.1016/0010-938X(85)90011-3.

[4] J. C. Wren, “Steady-State Radiolysis: Effects of Dissolved Additives,” in *Nuclear Energy and the Environment*, vol. 1046, American Chemical Society, 2010, pp. 271–295.

[5] J. M. Joseph, B. Seon Choi, P. Yakabuskie, and J. Clara Wren, “A combined experimental and model analysis on the effect of pH and O_2(aq) on γ-radiolytically produced H_2 and H_2O_2,” *Radiation Physics and Chemistry*, vol. 77, no. 9, pp. 1009–1020, Sep. 2008, doi: 10.1016/j.radphyschem.2008.06.001.

[6] J. W. T. Spinks, *An Introduction to Radiation Chemistry*, 2nd Edition. John Wiley & Sons, Inc., 1976.

[7] G. S. Was, “Environmentally Assisted Cracking of Irradiated Metals and Alloys,” in *Fundamentals of Radiation Materials Science*, Berlin, Heidelberg: Springer Berlin Heidelberg, 2007, pp. 765–814. doi: 10.1007/978-3-540-49472-0_15.

[8] R. Karimihaghighi, “Non-Linear Effects of Solution Parameters and Gamma Radiation on Nickel Oxidation Dynamics,” The University of Western Ontario, 2021. Electronic Thesis and Dissertation Repository, Available: https://ir.lib.uwo.ca/etd/7789

[9] A. Y. Musa and J. C. Wren, “Combined effect of gamma-radiation and pH on corrosion of Ni–Cr–Fe alloy inconel 600,” *Corrosion Science*, vol. 109, pp. 1–12, Aug. 2016, doi: 10.1016/j.corsci.2016.03.015.

[10] M. Behazin, J. J. Noël, and J. C. Wren, “Combined Effects of pH and γ-Irradiation on the Corrosion of Co-Cr Alloy Stellite-6,” *Electrochimica Acta*, vol. 134, pp. 399–410, Jul. 2014, doi: 10.1016/j.electacta.2014.04.079.

[11] M. Behazin, M. C. Biesinger, J. J. Noël, and J. C. Wren, “Comparative study of film formation on high-purity Co and Stellite-6: Probing the roles of a chromium oxide layer and gamma-radiation,” *Corrosion Science*, vol. 63, pp. 40–50, Oct. 2012, doi: 10.1016/j.corsci.2012.05.007.

[12] M. Behazin, “Radiation Induced Corrosion of Stellite-6,” The University of Western Ontario, 2014. Electronic Thesis and Dissertation Repository, Available: https://ir.lib.uwo.ca/etd/2434

[13] D. Guo, “Corrosion Dynamics of Carbon Steel in Used Fuel Container Environments,” The University of Western Ontario, 2018. Electronic Thesis and Dissertation Repository, Available: https://ir.lib.uwo.ca/etd/5897

[14] K. Ishigure, N. Fujita, T. Tamura, and K. Oshima, “Effect of Gamma Radiation on the Release of Corrosion Products from Carbon Steel and Stainless Steel in High Temperature Water,” *Nuclear Technology*, vol. 50, no. 2, pp. 169–177, Sep. 1980, doi: 10.13182/NT80-A32543.

[15] Q. W. Knapp and J. C. Wren, “Film formation on type-316L stainless steel as a function of potential: Probing the role of gamma-radiation,” *Electrochimica Acta*, vol. 80, pp. 90–99, Oct. 2012, doi: 10.1016/j.electacta.2012.06.090.

[16] K. Daub, X. Zhang, J. J. Noël, and J. C. Wren, “Gamma-radiation-induced corrosion of carbon steel in neutral and mildly basic water at 150 °C,” *Corrosion Science*, vol. 53, no. 1, pp. 11–16, Jan. 2011, doi: 10.1016/j.corsci.2010.09.048.

[17] S. Tuzi, K. Göransson, S. M. H. Rahman, S. G. Eriksson, F. Liu, M. Thuvander, and K. Stiller, “Oxide evolution on Alloy X-750 in simulated BWR environment,” *Journal of Nuclear Materials*, vol. 482, pp. 19–27, Dec. 2016, doi: 10.1016/j.jnucmat.2016.09.026.

[18] S. Tuzi, H. Lai, K. Göransson, M. Thuvander, and K. Stiller, “Corrosion of pre-oxidized nickel alloy X-750 in simulated BWR environment,” *Journal of Nuclear Materials*, vol. 486, pp. 350–360, Apr. 2017, doi: 10.1016/j.jnucmat.2017.01.051.

[19] L. R. Faulkner, “Understanding electrochemistry: Some distinctive concepts,” *Journal of Chemical Education*, vol. 60, no. 4, pp. 262–264, Apr. 1983, doi: 10.1021/ed060p262.

[20] L. Wu, D. Guo, M. Li, J. M. Joseph, J. J. Noël, P. G. Keech, and J. C. Wren, “Inverse Crevice Corrosion of Carbon Steel: Effect of Solution Volume to Surface Area,” *Journal of The Electrochemical Society*, vol. 164, no. 9, p. C539, Jul. 2017, doi: 10.1149/2.0511709jes.

[21] W. L. Mankins and S. Lamb, “Nickel and Nickel Alloys,” in ASM HANDBOOK Properties and Selection: Nonferrous Alloys and Special-Purpose Materials, vol. 2, ASM Handbook Committee, Ed. ASM International, 1990, pp. 428–445. doi: 10.31399/asm.hb.v02.a0001072.

[22] W. F. Smith, *Structure and Properties of Engineering Alloys*, 2nd Edition. McGraw-Hill, 1993.

[23] C. F. Baes and R. E. Mesmer, *The Hydrolysis of Cations*. John Wiley & Sons, Inc., 1976.

[24] M. Pourbaix, *Atlas of electrochemical equilibria in aqueous solutions*, 2nd Edition. National Association of Corrosion Engineers, 1974.

[25] B. M. Sass and D. Rai, “Solubility of amorphous chromium(III)-iron(III) hydroxide solid solutions,” *Inorganic Chemistry*, vol. 26, no. 14, pp. 2228–2232, Jul. 1987, doi: 10.1021/ic00261a013.

[26] D. W. Shoesmith, “Kinetics of Aqueous Corrosion,” in *Corrosion: Fundamentals, Testing, and Protection*, vol. 13A, S. D. Cramer and B. S. Covino, Eds. ASM International, 2003, pp. 42–51.

[27] Y. G. Shin, “Nonlinear Dynamics of Carbon Steel Corrosion under Gamma Radiation,” Western University, 2020. Electronic Thesis and Dissertation Repository, Available: https://ir.lib.uwo.ca/etd/7339

[28] M. Naghizadeh, “Copper Corrosion Dynamics under Deep Geologic Repository Conditions,” The University of Western Ontario. Accessed: Aug. 12, 2021. Electronic Thesis and Dissertation Repository, Available: https://ir.lib.uwo.ca/etd/7894/

[29] R. G. Kelly, J. R. Scully, D. Shoesmith, and R. G. Buchheit, *Electrochemical Techniques in Corrosion Science and Engineering*. Marcel Dekker, Inc., 2003.

CHAPTER 7

Thesis Summary and Future Work

7.1 Summary

This work investigated the corrosion dynamics of Inconel X-750 using a combination of electrochemical techniques and coupon exposure tests. The electrochemical techniques used were corrosion potential ((E_{corr}) measurements), cyclic voltammetry without a prior E_{corr} measurement ($CV_{t=0}$), and potentiodynamic (PD) polarization obtained after 24 hours of E_{corr} measurement ($PD_{t=24}$). The coupon exposure tests were performed using Inconel X-750 coupons immersed in solutions in sealed quartz vials. These measurements were complemented by post-test analyses involving dissolved metal analysis by ICP-OES and surface analysis using SEM. The experimental parameters were the solution pH, temperature, dissolved oxygen concentration, and the absence or presence of gamma-radiation. The key findings from this study are summarised below.

In Chapter 4, the evolution of E_{corr} under different solution conditions was studied. The E_{corr} was compared with the equilibrium potentials (E_{rxn}^{eq}) of redox half-reactions involving metals and metal oxides/hydroxides solid species, to understand the thermodynamically possible redox reactions happening on the surface of Inconel X-750. The results showed that E_{corr} started with a 1st (pseudo-) steady-state but did not remain in this steady-state. Rather, the E_{corr} moved toward a 2nd (pseudo-) steady-state, which was farther from the E_{rxn}^{eq} values of metal/metal oxides/hydroxides solid species (e.g., $E_{Fe^0 \rightleftharpoons Fe(OH)_2}^{eq}$) and closer to the E_{rxn}^{eq} of metal oxides/hydroxides solid species or between the E_{rxn}^{eq} of two redox reactions of metal oxides/hydroxides solid species. The shift from the 1st to the 2nd (pseudo-) steady-state was attributed to the formation of corrosion

products in the form of a hydrogel network which facilitated the formation of metal cations of higher oxidation states. Once a hydrogel network had developed, the metal cations of higher oxidation states acted as the main oxidant, and therefore controlled the redox conditions of the interfacial region and the overall corrosion process. The results from Chapter 4 indicated that the corrosion process occurs in three main stages:

- In stage 1, the interfacial region remains below the saturation limit of the dissolved metal cations and the overall rate of metal oxidation is controlled by the rate of the metal oxidation reaction.
- In stage 2: the interfacial region becomes saturated with dissolved metal cations, followed by the precipitation of corrosion products which results in the formation of a hydrogel network. In the presence of a hydrogel network, the transport of hydrated metal cations from the metal/solution interface to the bulk solution is very slow. When stronger oxidants than water are present in the solution, the dissolved metal cations can further oxidize and then precipitate resulting in the development of the hydrogel network to a mixture of different oxidation states of dissolved metal species.
- In stage 3, the interfacial region is covered with a hydrogel network. The hydrogel network can dehydrate and convert into solid crystal oxides which can inhibit the hydration of oxidized metal cations and suppress metal oxidation further.

The rate of metal oxidation cannot be extracted from the E_{corr} measurements. However, the rate of metal oxidation can be indicated by the potential-current relationship as a function of time. In Chapter 5, a comparison of $CV_{t=0}$ with the E_{corr} results confirmed the findings from Chapter 4. The results in Chapter 5 indicated that the $CV_{t=0}$ (with a scan rate of 5 mV s^{-1}) can extend beyond stage 1. More specifically, the likelihood of evolution of corrosion system from stage 1 to stage 2 increases in stagnant solutions, in solutions with more dissolved oxygen, at a higher temperature (i.e., 80 °C versus 25 °C) and when the rang of scanned potential is extended to more positive (more

noble) values. The $PD_{t=24}$ results showed that at longer times, the hydrogel network can dehydrate and convert into solid crystal particles (stage 3) which can further limit the rate of metal oxidation.

In Chapter 6, the solution analysis showed that the main effect of decreasing solution pH was to increase Ni dissolution. That is, decreasing the solution pH from 10.6 to 6.0 had a less significant effect on increasing Fe and Cr dissolutions. Inconel X-750 contains three main alloying elements (i.e., Cr, Fe and Ni). Therefore, the hydrogel network that forms as a result of the corrosion process is not necessarily a mixture of pure metal oxides/hydroxides particles or a stoichiometric metal oxides/hydroxides hydrogel network. This explained the effect of a mixed hydrogel network on the dissolution and oxide formation observations under different solution conditions. This finding from Chapter 6 was consistent with the E_{corr} and $CV_{t=0}$ observations in Chapter 4 and Chapter 5, respectively.

The results obtained from the study of the corrosion behaviour of Inconel X-750 in this work have improved the understanding of the processes involved in the corrosion of nickel-based superalloys in general and that of Inconel X-750 in particular. However, more research is required to further understand and validate the findings from this work and deconvolute the corrosion processes involved in more severe conditions.

7.2 Future Work

This work has contributed to a better understanding of the corrosion dynamics of Inconel X-750. The findings from this work predicted that the corrosion of Inconel X-750 (which has a different ratio of three main elements from Alloy 800 and Inconel 600 [1], [2]) can extend beyond the formation of Ni^{II} species (in the presence of strong oxidants) and the formation of nickel corrosion products with oxidation states higher than Ni^{II} can be part of the corrosion pathway.

To further understand the effect of oxide formation on the corrosion dynamics of Inconel X-750 in particular and nickel-based superalloys in general, more electrochemistry and coupon exposure test should be performed under different concentrations of dissolved oxygen and in different solution volumes (to better understand the effect of solution volume to surface area ratio). Post-test analysis techniques (e.g., Auger electron spectroscopy (AES), X-ray photoelectron spectroscopy (XPS), etc.) could be used to better understand the evolution of the composition of the oxide film with time under different oxidizing conditions. Coupon exposure tests could be performed at temperatures above 150 °C in the presence and absence of gamma-radiation.

7.3 References

[1] M. Momeni, "Gamma-Radiation Induced Corrosion of Alloy 800," The University of Western Ontario, 2017. Electronic Thesis and Dissertation Repository, Available: https://ir.lib.uwo.ca/etd/5011

[2] A. Y. Musa and J. C. Wren, "Combined effect of gamma-radiation and pH on corrosion of Ni–Cr–Fe alloy inconel 600," *Corrosion Science*, vol. 109, pp. 1–12, Aug. 2016, doi: 10.1016/j.corsci.2016.03.015.

APPENDIX A

Thermodynamic Data for Chromium, Iron and Nickel Redox Species

The expressions below (adapted from [1], [2]) and the thermodynamic data in **Table A.1** (from [2]–[8]) were used for the calculation of ΔG_f at 80 °C (353.15 K). These calculated data are summarized in **Table A.2**:

$$\Delta G_f(T) = \Delta G_f^0(298.15\ K) - (T - 298.15\ K) \times S^0(298.15\ K) - T\int_{298.15}^{T} \frac{C_p^0(T)}{T}\,dT + \int_{298.15}^{T} C_p^0(T)\,dT$$

$$C_p^0(T) = a + bT + cT^{-2}$$

where T is temperature in K and the unit for heat capacity, $C_p^0(T)$, is J/mol K. The values of the constants a, b, and c and S^0(298.15 K) are from references [2]–[8].

Table A.1 Thermodynamic data for redox species in the aqueous corrosion of Cr, Fe, and Ni at 25 °C ([2]–[8]).

Species	$\Delta {G_f}^0$(25 °C) (J/mol)	S°(25 °C) (J/mol K)	$C_p^0(T) = a + bT + cT^{-2}$ (J/mol K)		
			a	b	c
Cr^0	0	23.6	21.76	0.00898	-96000
$Cr(OH)_3$	-873170	105	127.6	0.041639	-4217000
Cr_2O_3	-1053090	81.2	119.37	0.0092	-1565000
Fe^0	0	27.28	28.18	-0.00732	-290000
$FeCr_2O_4$	-1343900	146	163	0.0223	-3190000
$Fe(OH)_2$	-491980	88	116.064	0.008648	-2874000
$Fe(OH)_3$	-705290	106.7	127.6	0.041639	-4217000
Fe_3O_4	-1015450	146.4	91.5	0.201	-
$\gamma - FeOOH$	-480100	65.08	59.76	0.06052	-772900
$\gamma - Fe_2O_3$	-725100	93.04	106.8	0.06509	-1886000
Ni^0	0	29.9	11.17	0.03778	318000
$\beta - Ni(OH)_2$	-458930	52.9	90	-	-
Ni_3O_4	-712000	140	117	-	-
$H_{2\,(g)}$	0	130.57	27.79	0.00326	50000
$O_{2\,(g)}$	0	205.06	29.96	0.00419	167000
H^+	0	-22.2	-71	-	-
H_2O	-237190	70.08	75.44	-	-

Table A.2 Thermodynamic data for redox species in the aqueous corrosion of Cr, Fe, and Ni at 80 °C.

Species	ΔG_f (80 °C) (J/mol)	C_p (80 °C) (J/mol K)
Cr^0	-1410	24.16
$Cr(OH)_3$	-879420	108.49
Cr_2O_3	-1058070	110.07
Fe^0	-1610	23.27
$FeCr_2O_4$	-1352590	145.30
$Fe(OH)_2$	-497250	96.07
$Fe(OH)_3$	-711630	108.49
Fe_3O_4	-1024240	162.48
$\gamma - FeOOH$	-484020	74.94
$\gamma - Fe_2O_3$	-730740	114.66
Ni^0	-1770	27.06
$\beta - Ni(OH)_2$	-462270	90.00
Ni_3O_4	-720260	117.00
$H_{2\,(g)}$	-7320	29.34
$O_{2\,(g)}$	-11440	32.78
H^+	1560	-71.00
H_2O	-241410	75.44

A. References

[1] J. Huang, X. Wu, and E. Han, “Influence of pH on electrochemical properties of passive films formed on Alloy 690 in high temperature aqueous environments,” *Corrosion Science*, vol. 51, no. 12, pp. 2976–2982, 2009.

[2] R. Karimihaghighi, “Non-Linear Effects of Solution Parameters and Gamma Radiation on Nickel Oxidation Dynamics,” The University of Western Ontario, 2021. Electronic Thesis and Dissertation Repository, Available: https://ir.lib.uwo.ca/etd/7789

[3] D. Cubicciotti, “Effect of copper on zircaloy corrosion in BWR,” *Journal of Nuclear Materials*, vol. 182, pp. 287–290, May 1991, doi: 10.1016/0022-3115(91)90444-C.

[4] D. Cubicciotti, “Potential-pH diagrams for alloy-water systems under LWR conditions,” *Journal of Nuclear Materials*, vol. 201, pp. 176–183, May 1993, doi: 10.1016/0022-3115(93)90173-V.

[5] B. Beverskog and I. Puigdomenech, “Revised Pourbaix diagrams for nickel at 25–300 °C,” *Corrosion Science*, vol. 39, no. 5, pp. 969–980, May 1997, doi: 10.1016/S0010-938X(97)00002-4.

[6] B. Beverskog and I. Puigdomenech, “Revised pourbaix diagrams for chromium at 25–300 °C,” *Corrosion Science*, vol. 39, no. 1, pp. 43–57, Jan. 1997, doi: 10.1016/S0010-938X(97)89244-X.

[7] B. Beverskog and I. Puigdomenech, “Revised pourbaix diagrams for iron at 25–300 °C,” *Corrosion Science*, vol. 38, no. 12, pp. 2121–2135, Dec. 1996, doi: 10.1016/S0010-938X(96)00067-4.

[8] J. Majzlan, B. E. Lang, R. Stevens, A. Navrotsky, B. F. Woodfield, and J. Boerio-Goates, “Thermodynamics of Fe oxides: Part I. Entropy at standard temperature and pressure and heat capacity of goethite (α-FeOOH), lepidocrocite (γ-FeOOH), and maghemite (γ-Fe_2O_3),” *American Mineralogist*, vol. 88, no. 5–6, pp. 846–854, May 2003, doi: 10.2138/am-2003-5-613.

APPENDIX B

Equilibrium Potentials of Redox Species of Chromium, Iron and Nickel at 25 °C and 80 °C (298.15 K and 353.15 K)

Electrochemical reactions are essentially chemical reactions. Therefore, their thermodynamics depend on the concentrations of the species involved and the temperature. The Nernst equation describes this dependence [1].

For reaction aRd + mH^+ +ne^- = bOx +cH_2O, the reversible potential (E_r) is calculated from the equation (1, [1]) [1].

$$E_r = E_\circ - \frac{RT}{nF} \ln \frac{\{Ox\}^b \{H_2O\}^c}{\{Rd\}^a \{H^+\}^m} \quad (1)$$

where $E_\circ$ the is standard reversible potential (i.e., E_r for unit activity of all reactants/products) and $\{i\}^j$ is the activity of species i, raised to the stoichiometric coefficient, j [1]. The equilibrium potentials in **Table B.1** are calculated using $\Delta G_f{}^0$(25 °C) and ΔG_f (80 °C) data in **Table A.1** and **Table A.2** [2]–[8].

The +241 mV (versus SHE) and +197 mV values (used to normalized the measured potentials versus SHE) are the potentials reported for Calomel (saturated KCl (~ 4 mol dm^{-3})) and $Ag/AgCl$ (KCl_{sat}) electrodes at 25 °C, respectively [9].

Table B.1 Equilibrium potentials of Cr, Fe and Ni redox species at 25 °C and 80 °C (298.15 K and 353.15 K).

R#	Reaction	E°, 25 °C (V)	E, 80 °C (V)
1	$Cr(OH)_3 + 3H^+ + 3e^- \rightleftharpoons Cr^0 + 3H_2O$	-0.556	-0.515
2	$Cr_2O_3 + 6H^+ + 6e^- \rightleftharpoons 2Cr^0 + 3H_2O$	-0.590	-0.561
3	$FeCr_2O_4 + 2H^+ + 2e^- \rightleftharpoons Fe^0 + Cr_2O_3 + H_2O$	-0.278	-0.251
4	$Fe(OH)_2 + 2H^+ + 2e^- \rightleftharpoons Fe^0 + 2H_2O$	-0.091	-0.050
5	$Fe(OH)_3 + H^+ + e^- \rightleftharpoons Fe(OH)_2 + H_2O$	0.247	0.296
6	$Fe_3O_4 + 2H_2O + 2H^+ + 2e^- \rightleftharpoons 3Fe(OH)_2$	-0.072	-0.063
7	$3\gamma - FeOOH + H^+ + e^- \rightleftharpoons Fe_3O_4 + 2H_2O$	0.513	0.586
8	$\gamma - FeOOH + H^+ + e^- \rightleftharpoons Fe(OH)_2$	0.123	0.153
9	$\beta - Ni(OH)_2 + 2H^+ + 2e^- \rightleftharpoons Ni^0 + 2H_2O$	0.080	0.132
10	$Ni_3O_4 + 2H_2O + 2H^+ + 2e^- \rightleftharpoons 3\beta - Ni(OH)_2$	0.987	1.011
	(For reactions 11 and 12, see **Appendix C**)	E, 25 °C (V)	
11	$2H^+ + 2e^- \rightleftharpoons H_2$	0.273	–
12	$O_2 + 4H^+ + 4e^- \rightleftharpoons 2H_2O$	1.175	–

The E° for $Ni(OH)_3 + e^- \rightarrow Ni(OH)_2 + OH^-$ reaction[1] is reported as 0.48 V [10]. The reactions in **Table B.1** are (adapted) from [2], [11]–[14].

[1] The reference used '→' for this reaction, but I believe the correct symbol is '⇌' because E° is defined as an equilibrium potential.

B. References

[1] R. G. Kelly, J. R. Scully, D. Shoesmith, and R. G. Buchheit, *Electrochemical Techniques in Corrosion Science and Engineering*. Marcel Dekker, Inc., 2003.

[2] R. Karimihaghighi, "Non-Linear Effects of Solution Parameters and Gamma Radiation on Nickel Oxidation Dynamics," The University of Western Ontario, 2021. Electronic Thesis and Dissertation Repository, Available: https://ir.lib.uwo.ca/etd/7789

[3] D. Cubicciotti, "Effect of copper on zircaloy corrosion in BWR," *Journal of Nuclear Materials*, vol. 182, pp. 287–290, May 1991, doi: 10.1016/0022-3115(91)90444-C.

[4] D. Cubicciotti, "Potential-pH diagrams for alloy-water systems under LWR conditions," *Journal of Nuclear Materials*, vol. 201, pp. 176–183, May 1993, doi: 10.1016/0022-3115(93)90173-V.

[5] B. Beverskog and I. Puigdomenech, "Revised Pourbaix diagrams for nickel at 25–300 °C," *Corrosion Science*, vol. 39, no. 5, pp. 969–980, May 1997, doi: 10.1016/S0010-938X(97)00002-4.

[6] B. Beverskog and I. Puigdomenech, "Revised pourbaix diagrams for chromium at 25–300 °C," *Corrosion Science*, vol. 39, no. 1, pp. 43–57, Jan. 1997, doi: 10.1016/S0010-938X(97)89244-X.

[7] B. Beverskog and I. Puigdomenech, "Revised pourbaix diagrams for iron at 25–300 °C," *Corrosion Science*, vol. 38, no. 12, pp. 2121–2135, Dec. 1996, doi: 10.1016/S0010-938X(96)00067-4.

[8] J. Majzlan, B. E. Lang, R. Stevens, A. Navrotsky, B. F. Woodfield, and J. Boerio-Goates, "Thermodynamics of Fe oxides: Part I. Entropy at standard temperature and pressure and heat capacity of goethite (α-FeOOH), lepidocrocite (γ-FeOOH), and maghemite (γ-Fe_2O_3)," *American Mineralogist*, vol. 88, no. 5–6, pp. 846–854, May 2003, doi: 10.2138/am-2003-5-613.

[9] G. Inzelt, A. Lewenstam, and F. Scholz, Eds., Handbook of Reference Electrodes, Springer-Verlag Berlin Heidelberg, 2013.

[10] A. J. Bard, R. Parsons, and J. Jordan, Eds., Standard Potentials in Aqueous Solution. New York: Marcel Dekker, Inc., 1985.

[11] M. Momeni, "Gamma-Radiation Induced Corrosion of Alloy 800," The University of Western Ontario, 2017. Electronic Thesis and Dissertation Repository, Available: https://ir.lib.uwo.ca/etd/5011

[12] X. Liu, X. Wu, and E.-H, "Influence of Zn injection on characteristics of oxide film on 304 stainless steel in borated and lithiated high temperature water," *Corrosion Science*, vol. 53, no 10, pp. 3337–3345, Oct. 2011, doi: 10.1016/j.corsci.2011.06.011.

[13] L. Wu, D. Guo, M. Li, J. M. Joseph, J. J. Noël, P. G. Keech, and J. C. Wren, "Inverse Crevice Corrosion of Carbon Steel: Effect of Solution Volume to Surface Area," *Journal of The Electrochemical Society*, vol. 164, no. 9, p. C539, Jul. 2017, doi: 10.1149/2.0511709jes.

[14] M. Pourbaix, Atlas of electrochemical equilibria in aqueous solutions, 2nd Edition. National Association of Corrosion Engineers, 1974.

APPENDIX C

Calculations of Equilibrium Potentials for Proton and Oxygen Reduction Reactions in Different Solution Conditions

The solubility of oxygen in water is 8.26 mg/L at 298 K for water saturated air at 760 Torr [1]. This is equal to 2.58×10^{-4} M. Therefore, at 25 °C (298.15 K) and air-saturated conditions:

$$\boldsymbol{O_2 + 4e^- + 4H^+ \rightleftharpoons 2H_2O} \qquad \textbf{(C1)}$$

$$E_r = E^\circ - \left(\frac{RT}{nF}\right) \ln\ (1/[H^+]^4\ [O_2])$$

$$E_r = 1.228 - \left(\frac{RT}{4F}\right) \ln\ (1/[H^+]^4\ [O_2])$$

$$E_r = 1.228 - \left(\frac{RT}{F}\right) \ln\ (1/[H^+]) - \left(\frac{RT}{4F}\right) \ln\ (1/\ [O_2])$$

$$E_r = 1.228 - 0.0591 \log\ (1/[H^+]) - \left(\frac{0.0256}{4}\right) \ln\ (1/\ [O_2])$$

$$E_r = 1.228 - 0.0591\ pH - \ 0.0147 \log\ (1/\ [O_2])$$

$$E_r = 1.228 - 0.0591\ pH - \ 0.0147 \log\ (1/2.58 \times 10^{-4})$$

$$E_r = 1.228 - 0.0591\ pH - 0.0147 \times (3.58)$$

$$E_r = 1.175 - 0.0591\ pH$$

The reported concentration of dissolved oxygen in deaerated water is 75 ppb [2] which is equal to 2.34×10^{-6} M. Therefore, at 25 °C (298.15 K) and under deaerated conditions:

$$\boldsymbol{O_2 + 4e^- + 4H^+ \rightleftharpoons 2H_2O} \qquad \textbf{(C1)}$$

$$E_r = E^\circ - \left(\frac{RT}{nF}\right) \ln\left(1/[H^+]^4\,[O_2]\right)$$

$$E_r = 1.228 - \left(\frac{RT}{F}\right) \ln\left(1/[H^+]\right) - \left(\frac{RT}{4F}\right) \ln\ \left(1/[O_2]\right)$$

$$E_r = 1.228 - 0.0591 \log\ \left(1/[H^+]\right) - \left(\frac{0.0256}{4}\right) \ln\left(1/[O_2]\right)$$

$$E_r = 1.228 - 0.0591\ pH - \ 0.0147 \log\ \left(1/[O_2]\right)$$

$$E_r = 1.228 - 0.0591\ pH - \ 0.0147 \log\ \left(1/2.34 \times 10^{-6}\right)$$

$$E_r = 1.228 - 0.0591\ pH - 0.0147 \times (5.63)$$

$$E_r = 1.228 - 0.0591\ pH - \ 0.082$$

$$E_r = 1.145 - 0.0591\ pH$$

To calculate the reversible potential for $2H^+ + 2e^- \rightleftharpoons H_2$ reaction, the concentration of hydrogen in atmospheric conditions and Henry's constant for H_2 are required. The average hydrogen content of air at ground level is reported to be 0.62 ppm [3] and the ppm is volume rather than mass for the following calculations:

C_{H_2} = 0.62 ppm (by volume)

P $_{(total)}$ = 1 atm

P_{H_2} = 1 atm × (0.62 × 10^{-6}) L/1 L = 6.2 × 10^{-7}

P(atm)= 6.2×10^{-7} atm which is the partial pressure of hydrogen gas under atmospheric conditions. Using Henry's constant for hydrogen, 1282.04 atm M^{-1} [1], the concentration of dissolved H_2 can be calculated from Henry's law:

$$6.2 \times 10^{-7}\ (\text{atm})/1282.04\ (\text{atm/M}) = 4.83 \times 10^{-10}\ \text{M}$$

Therefore:

$$\boldsymbol{2H^+ + 2e^- \rightleftharpoons H_2} \qquad \textbf{(C2)}$$

$$E_r = E^\circ - \left(\frac{RT}{nF}\right) \ln \frac{[H_2]}{[H^+]^2}$$

$$E_r = E^\circ - \left(\frac{RT}{2F}\right) \ln \frac{[H_2]}{[H^+]^2}$$

$$E_r = 0 - \left(\frac{RT}{F}\right) \ln\left(1/[H^+]\right) - \left(\frac{RT}{2F}\right) \ln\ ([H_2])$$

$$E_r = -0.0591\ pH\ - \left(\frac{0.0256}{2}\right) \ln 4.83 \times 10^{-10}$$

$$E_r = -0.0591\ pH\ - 0.0294 \log\ 4.83 \times 10^{-10}$$

$$E_r = -0.0591\ pH\ - 0.0294 \times (-9.31)$$

$$E_r = 0.273 - 0.0591\ pH$$

In reactions C1 and C2, concentration is used as an assumed approximation of activity. Reactions C1 and C2 and their E° values are from [4]. The value of R (8.31447 J K^{-1} mol^{-1}) and the value of F (96.48 kC mol^{-1}) are from [5].

C. References

[1] K. S. Schmitz, *Physical Chemistry*. Elsevier, 2017. doi: 10.1016/C2013-0-18556-X.

[2] I. S. Hwang, R. G. Ballinger, J. W. Prybylowski, and K. Hosoya, "Electrochemistry of Multiphase Nickel-Base Alloys in Aqueous Systems," *Journal of The Electrochemical Society*, vol. 136, no. 7, pp. 1874–1883, Jul. 1989, doi: 10.1149/1.2097067.

[3] E. Glueckauf and G. P. Kitt, "The hydrogen content of atmospheric air at ground level," *Quarterly Journal of the Royal Meteorological Society*, vol. 83, no. 358, pp. 522–528, Oct. 1957, doi: 10.1002/qj.49708335808.

[4] M. Pourbaix, *Atlas of electrochemical equilibria in aqueous solutions*, 2nd Edition. National Association of Corrosion Engineers, 1974.

[5] P. Atkins and J. de Paula, Physical Chemistry, W. H. Freeman and Company, 8th Edition, 2006.